The Dissertation Committee for Wei Jiang
certifies that this is the approved version of the following dissertation:

Wavelength-selective Micro- and Nano-Photonic Devices for Wavelength Division Multiplexing Networks

Committee:

Ray T. Chen, Supervisor

Joe C. Campbell

Ananth Dodabalapur

Michael Becker

Yao Li

Wavelength-selective Micro- and Nano-Photonic Devices for Wavelength Division Multiplexing Networks

by

Wei Jiang, B.S., M.A.

Dissertation

Presented to the Faculty of the Graduate School of
The University of Texas at Austin
in Partial Fulfillment
of the Requirements
for the Degree of

Doctor of Philosophy

The University of Texas at Austin

May 2005

To my parents

Acknowledgments

I would like to thank my advisor Dr. Ray Chen for his guidance throughout my doctoral study. When I came to Dr. Chen's group with a theoretical physics background, I could barely discern what seemed like interesting in theory. Now when I am about to leave, I begin to have a sense of what is truly meaningful in research. I owe a great deal to Dr. Chen for the engineering perspectives he imparted to me. In so many ways I am indebted to Dr. Joe Campbell, whose optoelectronics class was among the best parts of my educational experience at the University of Texas. I am deeply grateful that he rearranged a surgery to help me make a possible time slot for my qualifying exam, which he sat through in the midst of his rehabilitation. I will bear in my mind his teaching and guidance in many occasions; and if one day I have the honor to start a teaching career, Dr. Campbell will be my model. I also would like to thank other members of my dissertation committee Dr. Ananth Dodabalapur, Dr. Yao Li, and Dr. Michael Becker, for their encouragement and guidance. I am grateful to my Master's thesis advisor Dr. Herbert Berk, who always opens the door to me and finds time for me when I need help. Thank Dr. Alan Bovik for teaching me Matlab in his class, which streamlined my numerical calculation skills.

I appreciate the assistance from members of Optical Interconnect group, particularly those I worked closely with, Dr. Yingzhi Sun, Dr. Feng Zhao, Dr. Chuhua Tian, Chengxin Yang, Brie Howley, Yongqiang Jiang, and my officemate

Jeff Zou, as well as Jeannie Toll, Nancy Hard, William Fordyce, and other MER staff.

To all friends I was fortunate and honored to meet in the midst of service to the University and community, I thank your help, encouragement, dedication to service, and character that inspired me not only in service but in research or whatever career I shall choose. Thanks to Dr. Jay Guan for inducting me into the local community. Many thanks to Jerry Wilcox, Pamela Bona and all International Office staff I worked with. I especially appreciate friendship and support from Stacey Kounelias, Brian Haley, Katie King, Jordan Buckley, Rachel McGinity, and Huibing Zhang.

Thanks to Erying, a friend who knows me, and to Dingyuan, Nan and Qiang, who are always there when I need help. It was four great years, thank you my roommate Jun; and please extend my regards to Jie. To Lingyun, Susan, Dawei, Shizhong, as well as many other personal friends, sometimes thankfulness and gratitude are not measured by words, by felt by heart.

Thank my mother for being my role model, my father for his gift, my sister for her support. Thank uncle Tom and aunt Julie, I never wavered amid some disconcerting events in this foreign land because I knew that you were standing behind me. Thank aunt Jufang for many supportive phone calls and for the family stories that enlightened me.

WEI JIANG

The University of Texas at Austin
May 2005

Wavelength-selective Micro- and Nano-Photonic Devices for Wavelength Division Multiplexing Networks

Publication No. ____________________

Wei Jiang, Ph.D.
The University of Texas at Austin, 2005

Supervisor: Ray T. Chen

On the road toward the information age, the enormous bandwidth demanded by the explosive growth of Internet traffic has been supplied by fiber-optic communications technology; in particular, the widespread use of Wavelength-Division Multiplexing (WDM) techniques. My research focused on Optical Add-Drop Multiplexers (OADMs) and wavelength demultiplexers, two key devices for WDM technology. Various approaches, including nanophotonic approaches based on photonic crystals, were employed in the research.

First, a variety of ball lens-based OADMs were designed and implemented. The overall performance of the ball lens-based OADMs was competitive compared to that of commercial GRIN lens-based OADMs, while the former devices were more

cost-effective and simpler in packaging.

Optical Add-Drop Multiplexers are one of the promising applications of photonic crystals. Prior theories have been limited to devices with frequency-independent coupling and simple mirror symmetry. Through my research, a general model was developed to understand the optical add-drop process in realistic photonic crystal-based OADMs, where the interactions between the waveguides and cavities are frequency dependent and cavity modes depart from the accidental degeneracy of frequency. Furthermore, a class of devices with more freedom in choice of symmetry were proposed. An original idea was proposed to utilize the inevitable optical loss in a way that improves device performance.

The last part of my research was aimed at developing a wavelength demultiplexer based on the superprism effect in photonic crystals. In the course of this research, a general and rigorous refraction theory was developed for a photonic crystal of any lattice type, any surface orientation, and any surface termination. The theory solved some long-standing problems in grating diffraction as well. Refraction at naturally emerging quasi-periodic surfaces was treated in a unified way with the refraction on periodic surfaces. A new concept, surface-dependent mode degeneracy, was introduced and was shown to be crucial to understanding photonic crystal refraction. Arbitrary incident beam profiles were investigated. The first-ever practical demultiplexer design that has less than 3dB loss over a 25-nm spectrum is given based on this theory. The theory is anticipated to be instrumental in understanding some interesting research topics such as photonic crystal slab-based superlenses.

Contents

Chapter 3 Optical Add-Drop Processes in Symmetrical Waveguide-Resonator Systems 31

List of Tables

List of Figures

Chapter 1

Introduction: Optical Add-Drop Multiplexers for Fiber-Optic Communications & Emerging Role of Nanophotonics

1.1 Fiber Optic Communications

The explosive growth of the Internet in the final decade of the last century has transformed almost all aspects of society and life. Accompanying the Internet marvel was an unprecedented demand for communication bandwidth, which was fortunately echoed by an emerging fiber-optic communications technology: wavelength division multiplexing (WDM) [1, 2].

The communication networks have developed into a hierarchical system, as illustrated in Fig. 1.1. At the bottommost level, local area networks (LANs) of various sizes connect communication devices and computers in an entity such as an enterprise or a university. In many cities, these entities are connected through

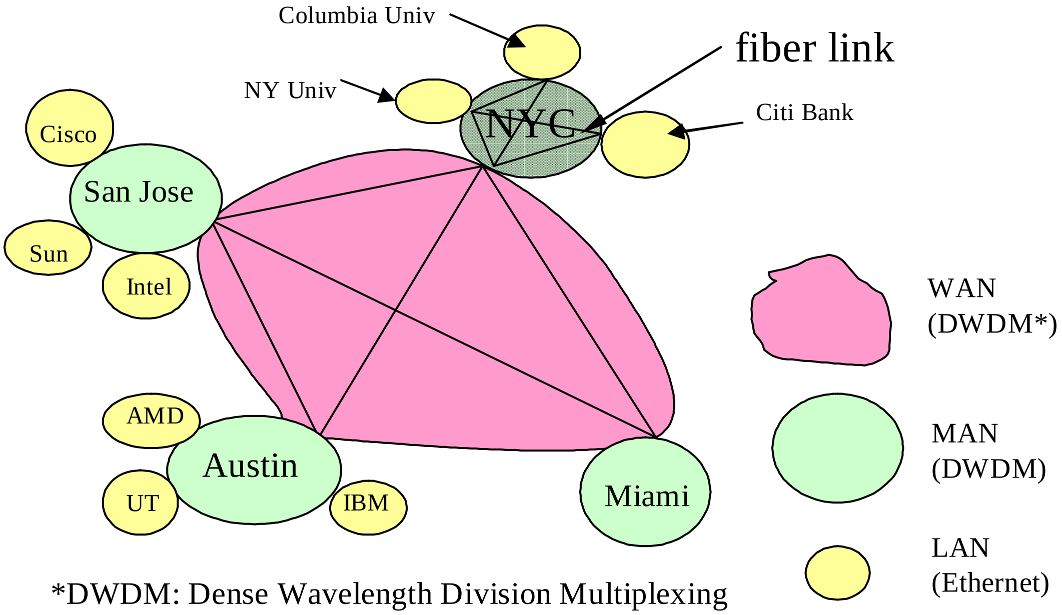

*DWDM: Dense Wavelength Division Multiplexing

Figure 1.1: Hierarchy of communications networks

metropolitan area networks (MANs), which are further connected to MANs elsewhere through wide area networks (WANs) or long-haul networks. The metropolitan area networks are regarded as the most promising market for WDM technologies owing to the busy traffic of MANs and the size of the market.

With the advent of erbium-doped optical amplifiers (EDFAs) and other related technologies, fiber-optic communications systems are evolving into the all-optical network era. In today's fiber-optic communications system, an electronic signal is modulated onto an optical wave and sent into a fiber, which relays the optical signal through a number of EDFAs far apart to reach a receiver that demodulates the optical signal into electronic form. In this way, electronic-optic(E-O) conversions occur only at the transmitter and receiver, which circumvents the bandwidth bottleneck owing to slow intermediate E-O conversion elements.

The wavelength-division-multiplexing technology has played a revolutionary role in expanding the bandwidth toward terabit communications. The transparent spectral windows of optical fibers are divided into small sections called channels, each of which transmits signals without interference by others. This approach exploits the bandwidth of optical fibers to its ultimacy. Since each channel can transmit signals at a rate of up to 40 GHz, which is limited only by the bandwidths of most optoelectronic devices, the aggregate bandwidth of the fiber-optic communications expands enormously.

One of the key functions of a WDM network is the capability of loading and unloading a specific wavelength of light from a fiber. For a typical WDM link shown in Fig. 1.2, light of one wavelength is added and/or dropped from a fiber through an optical add-drop multiplexer(OADM). Such an OADM is needed when a user needs to retrieve the information being transmitted in the fiber on that wavelength, and/or intends to send some information elsewhere through the WDM link.

Another useful device, illustrated in Fig. 1.2, is a demultiplexer(DeMUX), which separates each wavelength of light into individual fibers. Sometimes, the separated wavelengths of light will be bundled together again through a multiplexer(MUX), with some wavelengths of light replaced with fresh signals. Optical switches can be used to dynamically replace a number of the wavelengths, while variable optical amplifiers (VOAs) are used to balance the optical power of individual channels prior to further transmission.

My doctoral research has focused on the study of optical add-drop multiplexers and WDM demultiplexers. Optical add-drop multiplexers(OADMs) have been investigated using various approaches. Among them, the thin-film interference filter based micro-optic approach has been most successful in practice, although a number of novel approaches, such as fiber Bragg gratings [3–6] and waveguide couplers [7,8], have been the topics of research and development. For few-channel demultiplexers, a popular approach is to combine a number of single-channel OADMs in series. For high channel-count demultiplexers, arrayed-waveguide-grating or diffraction grating

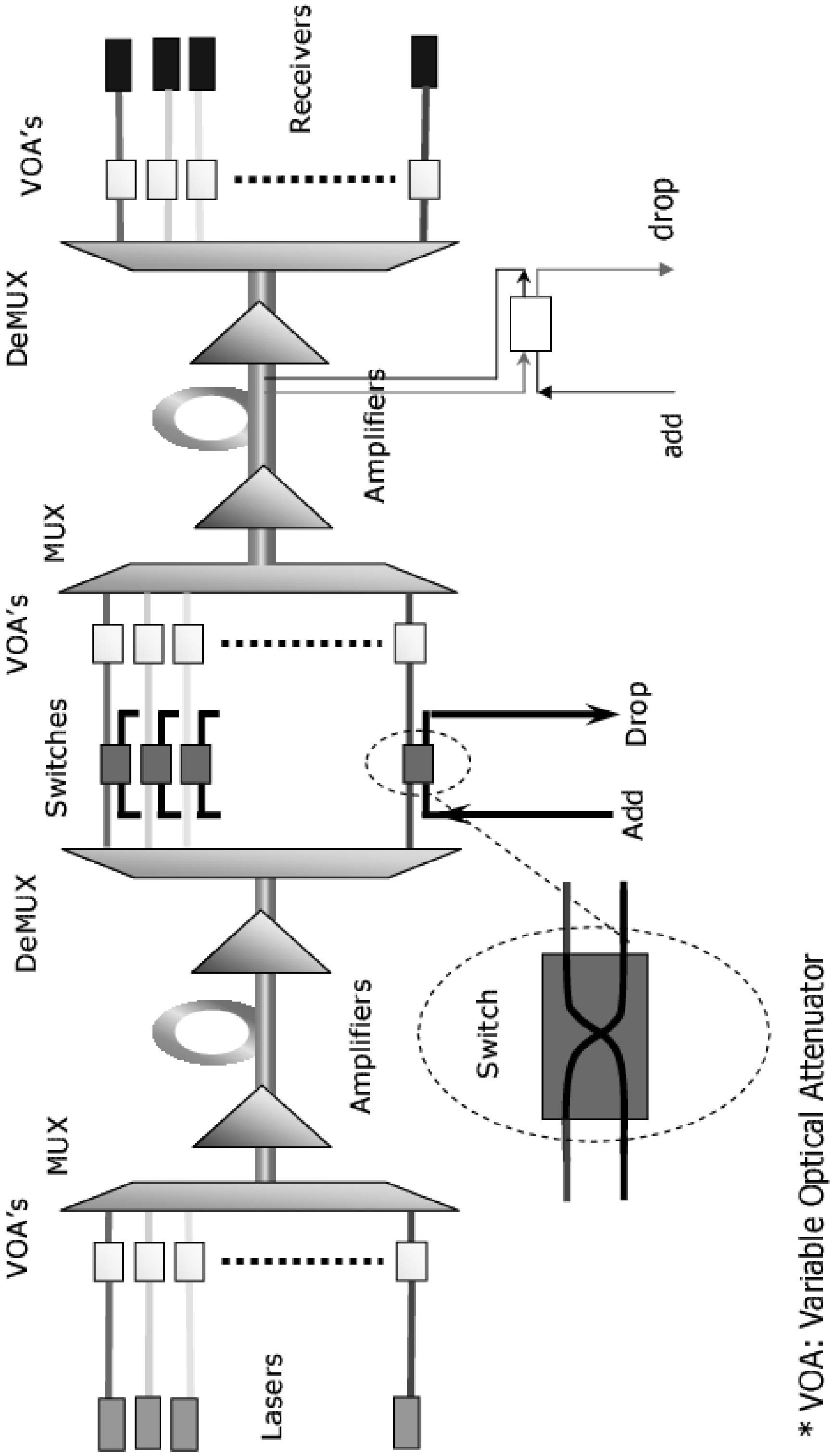

Figure 1.2: Typical MAN WDM link

based technologies appear to be cost-effective approaches that also reduce the maximum optical loss. However, reliability issues, such as thermal wavelength drift, and performance issues, such as channel transfer functions will determine whether these approaches will finally be competitive with the thin-film filter based technology in various contexts. We note that recently, the thin film filter technology has advanced into the realm of high channel-count demultiplexer with reduced optical loss.

In the first part of my doctoral research, thin-film filter based OADMs were built with ball lenses in place of the popular graded-index(GRIN) lenses [9,10]. The goal was to reduce the packaging complicacy and explore cost-effective engineering opportunities. Detailed aberration and tolerance analyses, coupled with careful packaging considerations, have allowed us to achieve these goals to a scale that the final device is a promising competitor of the commercial GRIN lens based OADMs.

1.2 A nanophotonic approach: photonic crystal based WDM devices

1.2.1 Nanotechnology for photonics

The beginning of the 21st century has witnessed the pervasive influence of nanotechnology. In photonics, nano-scale structures, particularly photonic crystals [11–17], hold the promise of achieving the same function in a significantly reduced device size. Accompanying the size reduction is the exciting prospect of ultimate power reduction (e.g. thresholdless laser [11]), unprecedented dispersion enhancement [15,16,18], and myriads of other benefits. As the advance of optical lithography played a critical role in the development of very large scale integration(VLSI) technology for microelectronics, the advance of electron beam(e-beam) lithography is defining the present and future of nanophotonics. In general, nanophotonics refers to a broad range of scientific and engineering areas and the fabrication techniques vary in these areas. Among those techniques, nanolithography, and particularly e-beam lithography may, I feel, provide a revolutionary technological base that will lead to some practical devices, which could enter every household and fundamentally change the way we live. I note that there are numerous new technologies being developed under the name of nanotechnology, and many of them work on even smaller scales. Yet many of them are essentially the conventional molecular-level technology, which is hardly considered a new area. There are exciting advancements appearing everyday in those areas, nonetheless they are more relevant to materials science, physics, chemistry, and biotechnology rather than immediate applications in electrical engineering or photonics.

In the development of electronic and photonic technology in the latter half of the last century, a burning desire of engineers was the endless miniaturization of devices. Nano-lithography feeds such a desire, and gives us virtually unlimited control of device geometry on deep submicron- and nano-scales. The key word here is "controllability." Other technologies may be able to produce structures on an even smaller scale(for example, quantum dots), but only e-beam nano-lithography allows people to shape the structures with the same latitude and accuracy that people design the structures of a car.

1.2.2 Photonic crystals and related devices

The issue of controllability is best exemplified in the development of photonic crystal technology. With periodic dielectric nano-structures, one can form perfect mirrors that reflect light totally for parts of the spectrum, regardless of the incident angle. This simple idea has stunning consequences that were first realized by Yablonovitch [11] and John [12] in 1987. The underlying principle is that periodic dielectric structures form optical bands and bandgaps in the frequency spectrum. In the photonic bandgaps, light is totally reflected.

In its first decade, the development of photonic crystal technology almost entirely surrounded this idea, which utilized photonic crystals as the photon-confining "walls" for ultra-compact optical cavities and waveguides. From another perspective, the photonic crystals were regarded as an "optical insulator" exclusively. That is why another term "photonic bandgap materials" was used more often in the early years of photonic crystal research. In 1998, Kosaka *et al.* published the first important paper about light refraction and propagation in photonic crystals. Exciting applications were discussed based on anomalous refraction and propagation effects in photonic crystals. In these applications, photonic crystals essentially act as "optical conductor." I have found that the study following the theme of "optical conductor" is promising and relatively unexplored even today.

In my doctoral study, I initially focused on waveguide-resonator systems based on photonic crystals to perform the optical add-drop function [19], which still treated photonic crystals as optical insulators. In a later stage, I began to consider the "conducting" characteristics of photonic crystals, and utilized anomalous refraction and propagation of light inside photonic crystals to develop demultiplexers.

Chapter 2

Ball-lens Based Optical add-drop Multiplexers: Designs and Implementations

2.1 Introduction

Wavelength-Division-Multiplexing (WDM) has been widely recognized as an enabling technology for ultra-high bandwidth optical networks. Optical add-drop multiplexers (OADM) are indispensable elements in WDM-based networks. Various approaches have been considered for making such a device, including thin-film bandpass filters, fiber Bragg gratings[3-6], and waveguide couplers[7,8]. Among these approaches, the one utilizing a thin film filter along with a pair of GRIN lenses has taken the lead due to low cost, satisfactory performance, and high reliability.

GRIN-lens based devices have achieved considerable success in micro-optics due to the general perception about relative ease of employment of GRIN lenses. However, recent improvement in ball-lens coating technology[20] has aroused significant interest in expanding the usage of ball lenses in micro-optical devices. Now in many situations, ball lenses offer competitive performance and obvious convenience, while presenting a distinct cost advantage over GRIN lenses.

In this part of my study, a variety of ball-lens based optical add-drop multiplexers (OADMs) were designed and implemented in collaboration with my colleagues. Insertion losses as low as 0.5 to 0.6 dB for the reflection light-path, and 1.2 to 1.5 dB for the transmission light-path were demonstrated. The 0.5-dB passband and 30-dB stopband for a 100-GHz OADM were 0.35 nm and 1.15 nm, respectively. The reflection path had an isolation of 15 dB. In addition to the distinct cost advantage of ball lenses over the GRIN lenses, the ball-lens based OADMs also offer a significant simplification in packaging due to the intrinsic spherical symmetry of ball lenses. For one of the designs, the overall performance of a ball-lens based OADM was competitive compared to that of a commercial GRIN-lens based counterpart. Optical designs and optics-related packaging issues will be discussed in detail.

2.2 Designs

2.2.1 Design Outline

In a beam-splitting ball lens studied earlier [21], a thin-film beam-splitting filter was disposed at the mid-plane of a full-ball lens. The light was incident on the filter at 45^o and was split into two beams perpendicular to each other. A straightforward idea of OADM would be to replace the beam-splitter filter with a narrowband WDM filter. However, to our knowledge, no WDM filter working at 45^o incident angle is available. And those narrowband filters intended to work at nearly normal incidence usually have very high transmission loss at large incident angles. Therefore, we designed our first OADM (Design A) employing a similar setting, but the incident angle was nearly normal. The design is schematically shown in Fig. 2.1. The transmission light-path is between input and drop fibers, and the reflection light-path is between

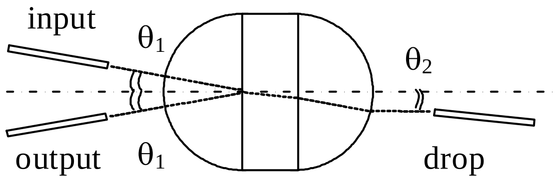

Figure 2.1: Design A: Half-ball lens OADM with tilted fibers

input and output fibers(when used as an add multiplexer, the light actually travels from drop to input fiber, and from output to input fiber for these paths). The ball lenses are made of SF2 glass and are 3.4 mm in diameter. The factors influencing the choice of glass and focal length will be discussed later. An ideal design would prefer the thin film filter to be deposited on the plano side of one of the half balls. Though not impossible, this substrate geometry is not compatible with mass production of filters. For this reason, we used a standard thin-film filter having a substrate of 1 mm thick sandwiched between the two half balls. It turned out that the additional thickness of the filter substrate affected only the angle of the drop fiber with the optical axis.

Through aberration study, no significant degradation of performance was found due to the presence of a thick substrate. The fiber endfaces were located at the focal planes of the corresponding half balls. In this arrangement, a collimated beam was incident on the filter. The input and output fibers were fixed in two v-grooves on a metal strip. These two v-grooves were separated by d (center to center) at the end, and each was tilted at an angle θ_1 toward the optical axis. The drop fiber was at an angle θ_2 with respect to the optical axis. The angles are given by

$$\theta_1 = \frac{d}{2(f+r)}, \tag{2.1a}$$

$$\theta_2 = \left[1 - \frac{n_a(n_a-1)}{r}\left(\frac{b}{n_b}+c\right)\right]\theta_1, \tag{2.1b}$$

where n_a and n_b are the refractive indices of the ball lenses and the filter substrate, respectively, r is the radius of curvature of the half-ball lenses, f the *front* focal length of the left half ball, b the thickness of the filter substrate, and c the thickness of the thin air gap between the filter backside and the second ball lens. These relations were determined by paraxial raytracing. Note θ_1 is actually the angle of incidence (AOI) onto the thin film filter. The choice of fiber spacing d will affect AOI and therefore the center wavelength(CWL) shift of the filter passband. The major advantages of this system are the simplicity of packaging and mechanical stability due to the fact that lenses and filters are closely packed together.

However, it turned out the aberrations of this system would be large if single-mode fibers(SMFs) were to be used. Following Smith[22], we studied the image aberration of a single point on the object because the fiber core is much smaller than $h = d/2$, the displacement of the fiber from the optical axis. An indication of small aberration is that the image spot size of the center point of input fiber endface is considerably smaller than the fiber mode-field radius. In this case, even after focusing adjustment, the root-mean-square(RMS) image spot radius was found to be larger than the SMF mode-field radius. We therefore introduced into this design the thermally-expanded-core (TEC) fibers, which have a larger mode field radius and a smaller numerical aperture(NA). The RMS aberration spot radius increases with NA, while the mode field radius of the TEC fiber is approximately inversely proportional to the numerical aperture[23], as shown in Fig. 2.2(a). One finds these two quantities cross at numerical aperture about 0.12 for typical lenses we used. Figure 2.2(b) shows the variation of the Strehl ratio [24] with NA. For NA less than 0.11, the central diffraction peak deduction due to aberration is less than 10% for both BK7 lenses and SF2 lenses. In the experiments, we used TEC fibers with NA approximately 0.04 for Designs A and C.

To further reduce the cost associated with TEC fibers, we developed Design

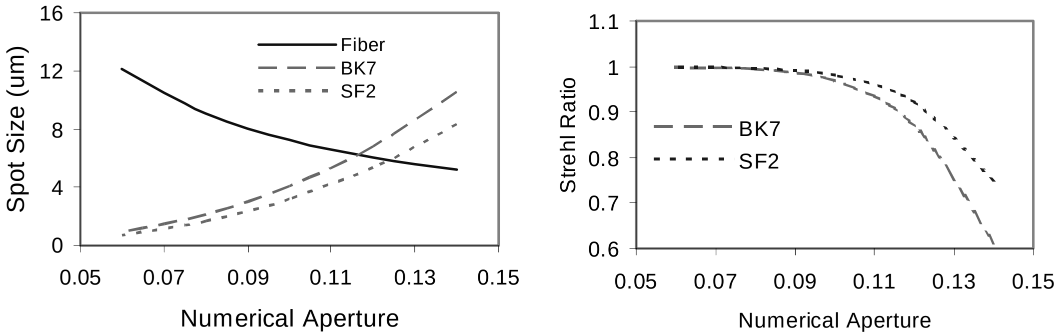

(a) (b)

Figure 2.2: Effect of NA reduction: (a) RMS Aberration spot radius and fiber mode-field radius vs. NA. (b) Change of Strehl ratio, which is indicative of normalized central peak intensity.

B [Fig. 2.3(a)], where a pair of full ball lenses were used. The aberration study showed that the aberrations in Design B would be acceptable if standard SMFs were used. For this system, there is not a natural center for the input and output fibers to aim at. Therefore, the fibers do not have to be tilted with respect to the axis. The airgaps a and c were determined through paraxial raytracing to be

$$a = f = \frac{(2 - n_a)}{(n_a - 1)} \frac{r}{2}, \tag{2.2a}$$

$$c = a - \frac{b}{n_b}, \tag{2.2b}$$

where f is the front focal length of the ball lens, other symbols denote the same quantities as in Design A. The paraxial AOI onto the filter is

$$AOI = \frac{2h(n_a - 1)}{n_a r}, \tag{2.3}$$

where h is the "object height," or the distance from the center of the input fiber endface to the optical axis.

Illustrated in Fig. 2.3 (b) is a comparative design of OADM using half-ball lenses in the parallel fiber setting. For this system, which we call Design C, the corresponding parameters are given by

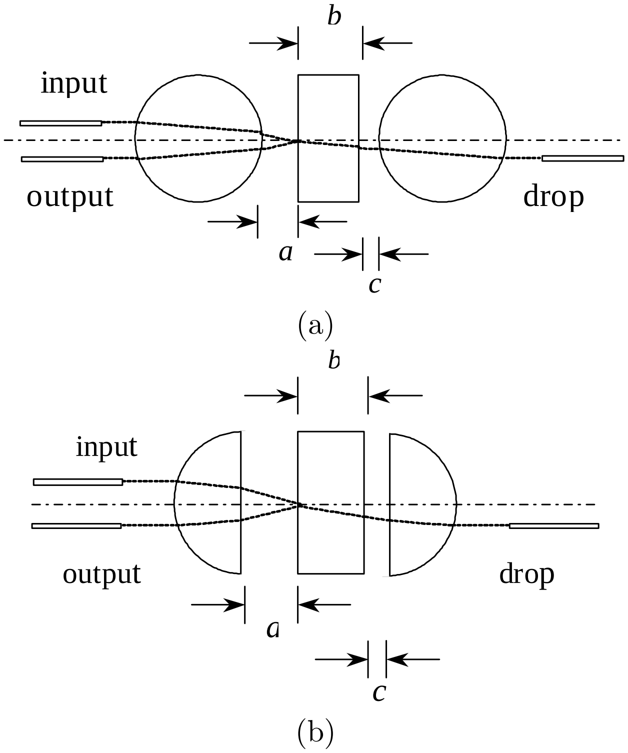

(a)

(b)

Figure 2.3: (a) Full-ball lens OADM (Design B). (b) Half-ball lens OADM with parallel fibers (Design C)

$$\begin{aligned} a =& \frac{r}{n_a(n_a-1)}, \\ c =& a - \frac{b}{n_b}, \\ AOI =& (n_a - 1)\frac{h}{r}. \end{aligned} \tag{2.4}$$

2.2.2 Aberration study

For comparison, we will analyze the aberration for both full ball and half ball cases in the setting where the fibers are all parallel to the optical axis, *i.e.* Designs B and C. Then we will show the fiber tilting in Design A would not introduce much difference in aberrations compared with Design C if both designs used the same type of fibers.

First, some commonalities of the aberrations in Design B and C are presented. Assume the axes of all three fibers are placed at a distance h from the optical axis and the light cones exiting the fibers have a half apex angle α. Since the object (the input fiber core) is much smaller than h, it is a convenient choice to pick the center ray of the light cone as the reference ray, and ray on the side of cone as the marginal ray. The aberration is essentially contributed by the spherical surfaces only. By raytracing one can easily show that in Designs B and C, when $c = a - b/n_b$ holds, there is a symmetry between the reflection and transmission light paths except for the region inside the filter substrate. Therefore, the aberration values are almost the same for the two "images" of the input fiber at the location of output and drop fibers. So the following aberration analysis applies to both output and drop fibers. A useful dimensionless parameter in evaluation of the aberration is q, as we call. For Design B and C, it is defined as

$$q_B = \frac{2h(n_a - 1)}{\alpha n_a r}, \tag{2.5a}$$

$$q_c = \frac{h}{\alpha r}(n_a - 1), \tag{2.5b}$$

respectively. For h=62.5 μm, NA=0.14 and n_a=1.50065(BK7), r=1.35 mm, one finds q_B=0.22 and q_C=0.16. For values of q small compared to unity, we can show that the contributions of astigmatism and Petzval to the overall aberration are all approximately q^2 times smaller than the spherical aberration, the distortion is q^3 times smaller than the spherical aberration. The sagittal coma on each surface is approximately q times smaller than the spherical aberration. However, sagittal comas on symmetrical pairs of spherical surfaces tend to have opposite signs and cancel each other, leaving the leading term in the total coma of order q^2. Note all spherical surfaces contribute to the total spherical aberration with a consistent sign. Therefore, in this system, the spherical aberration is the major concern.

The following semi-quantitative analysis shows that generally Design B has a significantly lower aberration than Design C. We assume that the fiber NA, material and radius of the lenses are same in both designs. According to aberration theory, the transverse spherical aberration TSC of a surface is given by [22]

$$TSC = C_1(u' + i)yi^2h \tag{2.6}$$

where C_1 is a constant same for same kind of surfaces in two systems, h the final image height, i the incident angle of a marginal ray on the surface, u the marginal ray slope after refraction, and y the height at which the marginal ray intersects the current surface. The angle i for the half ball system per surface is, on average, about twice larger than the corresponding value in the full ball system. The ray height y at each spherical surface is always smaller in Design B than in Design C. Particularly, it scales roughly linearly with the front/back focal length for the first/last surface. Note the front focal length of the half ball is about quadruple of that of the full ball (for index around 1.5). The remaining factor in Eq. (2.6), for most surfaces, yields higher values in the half ball case also. Now consider there are half number of spherical surfaces in Design C compared to Design B, we reach the estimate that the spherical aberration is 8 times or more in Design C compared to Design B. The results from rigorous Seidel aberration calculations are shown in Table 2.1. Note the spherical aberration, by convention, refers to its value at the paraxial image plane, while the RMS spot radius listed is its minimum value along the optical axis, see the last section of this chapter. According to Table 2.1, for both types of lenses listed, the ratios of the corresponding aberrations between the Design C and B are around 10, in reasonable agreement with the preceding estimate.

In addition, it turns out that we do not need to do a separate aberration analysis for Design A. By properly tilting the local coordinate system on each surface in Design C, one can prove that Design A has essentially the same aberration as a special case of Design C where $h = 0$. We also note the aberration only weakly depends on h for h below 250 μm.

Glass Diameter	BK7 2.7mm		SF2 3.4mm	
	Spherical Aberration	RMS spot radius	Spherical Aberration	RMS spot radius
Full Ball	7.1	1.18	5.04	0.84
Half Ball	69.1	11.5	53.1	8.85

Table 2.1: Aberration comparison of different designs(Unit: μm)

2.3 Implementation and practical issues

2.3.1 Choice of components

One design aspect we have not discussed until this point is the selection of glass material and the radius of the ball lenses. To lower the cost, we used the common materials such as BK7 and SF2, which are inexpensive but have low refractive indices. The use of a material having higher refractive index reduces the aberration further, but usually incurs higher cost for materials. Since Design B has demonstrated sufficiently low insertion losses, we have not proceeded to use materials other than BK7 for that design. The choice of the radius of the ball lenses needs to take into account the focal length and filter incident angle requirements from the optical design, the size of fiber ferrules, and total package size. It was found that for refractive index of ball lens around 1.5 and h=62.5 μm, the radius of the ball should be around 2.7 mm to yield the common 1.8^o incident angle on the filter in Design B. For half ball designs, the filter AOIs are in the range of 0.8 to 2.6 degrees, depending on h. Such a deviation from 1.8 degree introduces an extra shift in the central wavelength of the filter passband, and possibly a slight change in transmission loss, while leaving all other parameters virtually unchanged.

2.3.2 Packaging Considerations

A considerably simplified packaging scheme was designed for these systems. The general idea was to first package lenses and filters together into a lens set without alignment. Then the fibers, or fiber ferrules (or holders), are aligned to the lens set. In a typical GRIN-lens based OADM, there are three alignment steps. They are (1)between a dual-fiber ferrule and one GRIN lens, (2) between a drop fiber ferrule and the other GRIN lens, and (3) between the two GRIN lenses. Our packaging scheme of ball-lens based OADMs allowed the omission of the alignment procedure between lenses and filter, therefore saved a lot in alignment work compared to a GRIN-lens based OADM.

The viability of this packaging scheme is supported by several optical and mechanical considerations. The misalignments within the lens set have two effects: the change of the image position and orientation in space, and the increase of the aberration. The first effect can always be compensated by moving the receiving fibers. For example, in Design C, the tilt of the filter results in a change of image position Δy at the output fiber, one can move the dual fiber ferrule holding the input and output fibers by $\Delta y/2$ to compensate this change. For the image at the drop fiber, the compensational movement is straightforward. For various such compensations, the movement range is around a few dozens of microns. For the aberration increase due to misalignment, two attributes greatly simplify the analysis: (1) the intrinsic symmetry of half and full balls; (2) the extremely weak dependence of aberration on airgap thickness. By these two attributes, the leading contributions to the extra aberration in all designs come only from the lateral misalignments of axes of the two lenses, although in Design C the tilt of half ball may produce small extra aberration as well. All other misalignments are either geometrically equivalent to the above two types, or have negligible effects on the aberration. The aberration increases due to misalignments are presented in Figs. 2.4 & 2.5 for Designs B & C.

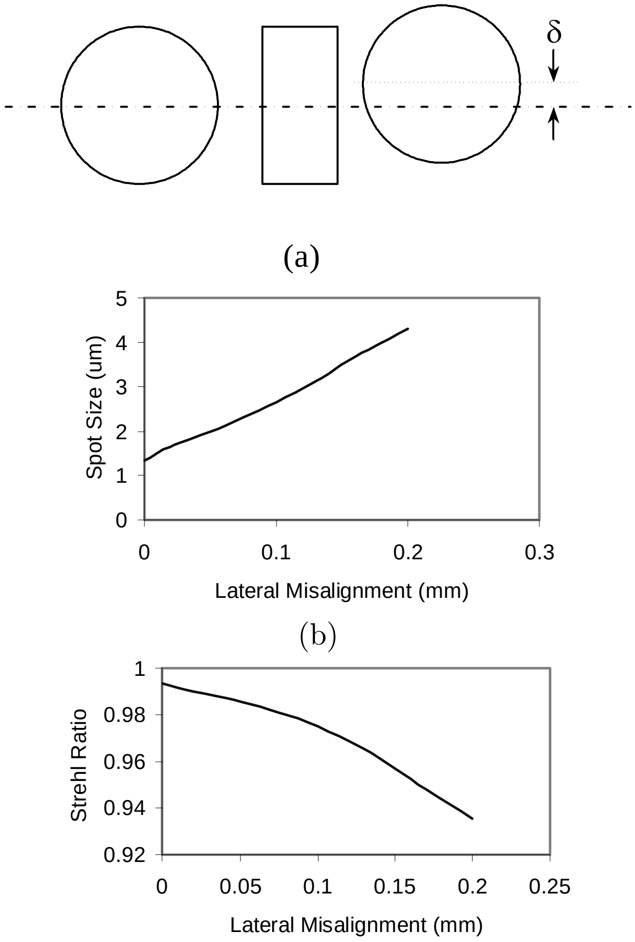

(a)

(b)

(c)

Figure 2.4: Analysis of lateral misalignments for Design B (a) Illustration of a misalignment; (b) The spot size change due to such a misalignment; (c) Change of Strehl ratio.

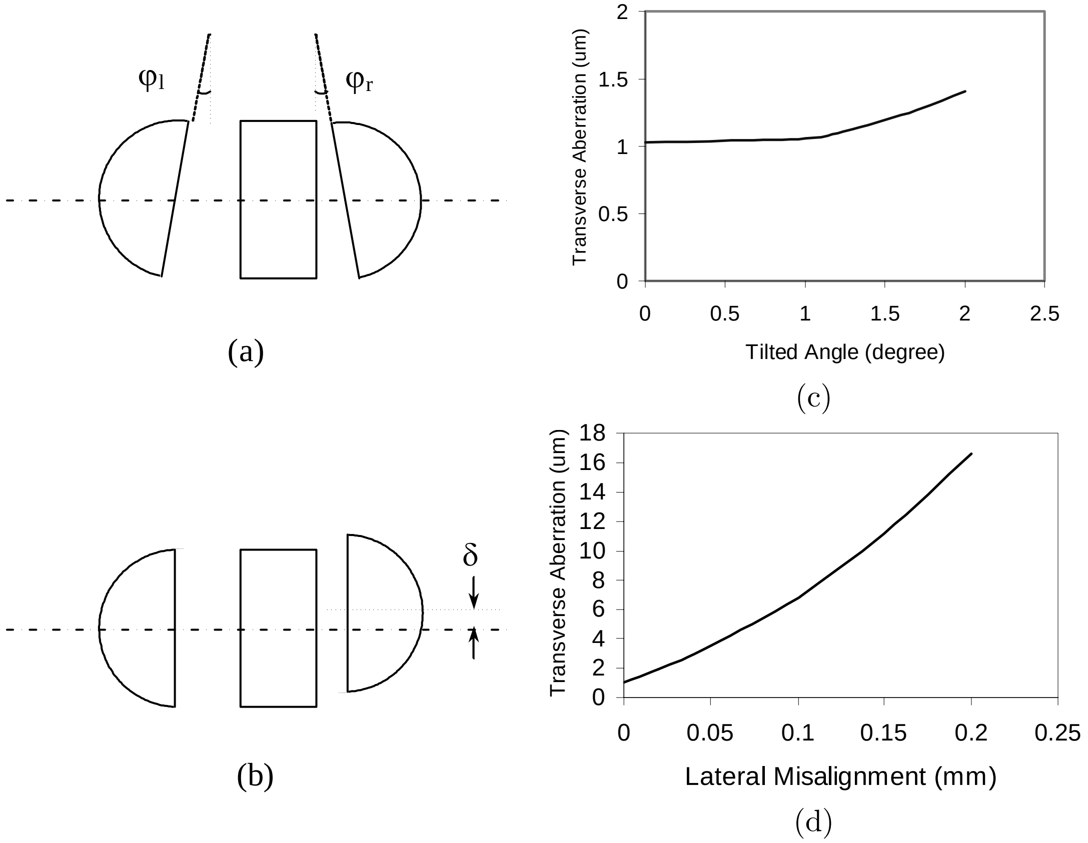

Figure 2.5: Misalignments in Design C and accompanying aberration increases. (a) Non-parallelism between the filter surface and the plano surfaces of the half-balls. (b) Lateral separation between the axes of two half-balls. The changes of transverse aberration with (c) angular misalignment, (d) with lateral misalignment.

For Design C, note the TEC fibers have core sizes around 35 μm. Therefore a lateral misalignment below 0.1 mm does not result in an unacceptable loss according to Fig. 2.5(d). For Design A, the misalignments have the same effects as for Design C, except we do not need to consider the tilts of half balls. The above compensational movements and the refocusing movements demand that the packaging design leaves enough space (usually in the range of 0.1 mm) during the alignment. On the other hand, epoxy application desires minimal spacing between parts to reduce the alignment shift after curing. This duality presents one major challenge in packaging, particularly due to the tight loss margin of OADMs. In our designs, small extra parts were used to fill in the position to reduce the space. To accommodate all possibilities of space geometry after alignment demands thoughtful shape designs of these parts. Combined with careful packaging labor, we achieved a loss increase of less than 0.1 dB after epoxy curing.

2.4 Testing and analysis

2.4.1 Comparison of Raw Filter Data and Packaged Device

In this chapter, some critical performance parameters after packaging will be compared with the original filter data. A 200-GHz OADM of design B using a pair of BK7 2.5-mm-diameter ball lenses is analyzed in Table 2.2. The "Raw Filter" data were provided with the filter and were measured at normal incidence. The spectra of transmission and reflection light-paths are presented in Fig. 2.6 for all three designs. The picture of a packaged OADM is shown in Fig. 2.7. Table 2.2 shows a slight reduction of the 0.5-dB bandwidth after packaging. However, it is still much higher than 0.5 nm, typical requirement of a 200-GHz OADM. The peak insertion loss is 1.26 dB. A more careful and stricter consideration of transmission bandwidth of this device needs to take into account the isolation capability of the

	CWL * (nm)	Bandwidth @0.5dB (nm)	Transmission Peak Loss(dB)	Stopband @30dB (nm)	Ripple (dB)
Raw filter	1549.63	0.86	0.39	2.24	0.12 ∼ 0.22
Device	1549.20	0.80	1.26	2.41	<0.2

* CWL: central wavelength, obtained by averaging two wavelengths at 3dB from the peak.

Table 2.2: Comparison between a packaged device and a raw filter

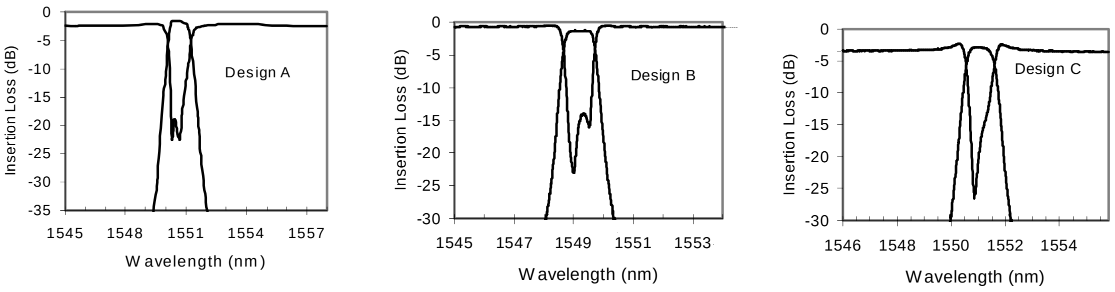

(a) (b) (c)

Figure 2.6: Measured spectra of devices pursuant to various Designs: (a) Design A; (b) Design B; (c) Design C

reflection light-path. Figure 6(b) shows that from 1548.84 nm to 1549.54 nm, the reflection path isolation is better than 16dB, a typical value of GRIN-lens OADM. The transmission path has its insertion loss less than 1.58 dB over this spectral width of 0.7 nm. The stopband increases slightly. The change of ripple is below detection. Polarization dependent loss (PDL) is less than 0.25 dB. The shift of central wavelength is expected. An ideal design B would require a 2.7-mm-diameter ball lens to produce the typical 1.8^o AOI, at which the filter may have a center wavelength shift of approximately 0.3 nm. Due to the unavailability of 2.7-mm ball lenses, we substituted a 2.5-mm-diameter, which should produce an AOI of 1.91^o by

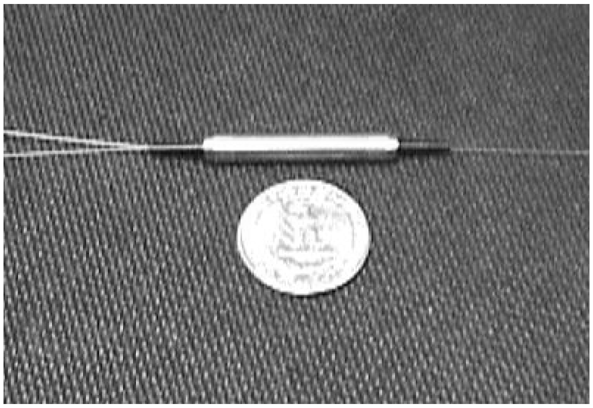

Figure 2.7: A packaged 200-GHz OADM (Design B), along with a quarter dollar coin for a sense of size

Eq. (2.3). The relation between the CWL shift and tilted angle is given by [25]

$$\frac{\Delta\lambda}{\lambda_0} = \frac{\theta_i^2}{2(n^*)^2}, \tag{2.7}$$

where λ_0 is the central wavelength of the filter at zero AOI, $\Delta\lambda$ is the CWL shift at incident angle θ_i, and n^* is the effective refractive index of the dielectric stack. Using this relation, the expected CWL shift is 0.34 nm for the designed 1.91^o AOI. Using the relation reversely, the actual 0.43 nm wavelength shift is found to correspond to 2.15^o incident angle. Though the universal equation (2.7) may not be accurate due to variations in filter production, we can estimate from our data that usually the angular misalignments are around quarter degrees. The slight bandwidth change is in accordance with the narrow band theory [25], which predicts it is of the order θ_i^4.

2.4.2 Comparison of measured performances and packaging issues of different designs

The performance of various designs are compared in Fig. 2.6 and Table 2.3. For Design A, from 1550.31 nm to 1550.90 nm, the transmission path has an insertion

Design	A	B	C
Reflection path	2.1 (1.4) *	0.5	2.3 (1.1)
Transmission path	1.5 (0.6)	1.26	2.8 (1.6)

* Expected insertion losses after deducting reflection loss are presented in parentheses, for Designs A and C.

Table 2.3: Peak Insertion Losses of different designs: experimental data

loss less than 1.87 dB (note the peak insertion loss for this path is 1.51 dB). The reflection path has an isolation greater than 15 dB for this wavelength range. This range is about 0.1 nm narrower than the data for Design B presented above because the filters used for Designs A and C have a 0.5-dB bandwidth about 0.1 nm(at normal incidence) narrower than the filter used in Design B. For Design C, from 1550.69 nm to 1551.27 nm, the insertion loss for the transmission path is less than 3.4 dB (peak at 2.78 dB), and the isolation of the reflection path is greater than 14 dB. The 30-dB stopband of the transmission path is around 2.42 nm for both cases. The ripple and PDL are both less than 0.25 dB.

Designs A and C were implemented using uncoated half-ball lenses and TEC fibers. The half-ball lenses are made up of SF2 glass and 3.4 mm in diameter. The expected losses are presented in parentheses in Table 2.3 after deducting the excess losses due to reflection. Note that for the SF2 lenses used in the half-ball designs, the reflection loss in the air is around 0.25 dB per surface. The reflection loss per fiber endface is estimated to be 0.15 dB. Each light path in Design C has 4 uncoated lens surfaces and 2 uncoated fiber endfaces, which correspond to a total of 1.3 dB excess loss. In Design A, the filter front surface is in contact with the plano surface of one half-ball lens and the coating was designed to roughly index-matched to SF2. Therefore, we have deducted reflection losses of 0.8 dB for the reflection path and 1.05 dB for the transmission path. (Since no AR coating is perfect, we leave about 0.1 dB margin for the reflection loss in Table 2.3).

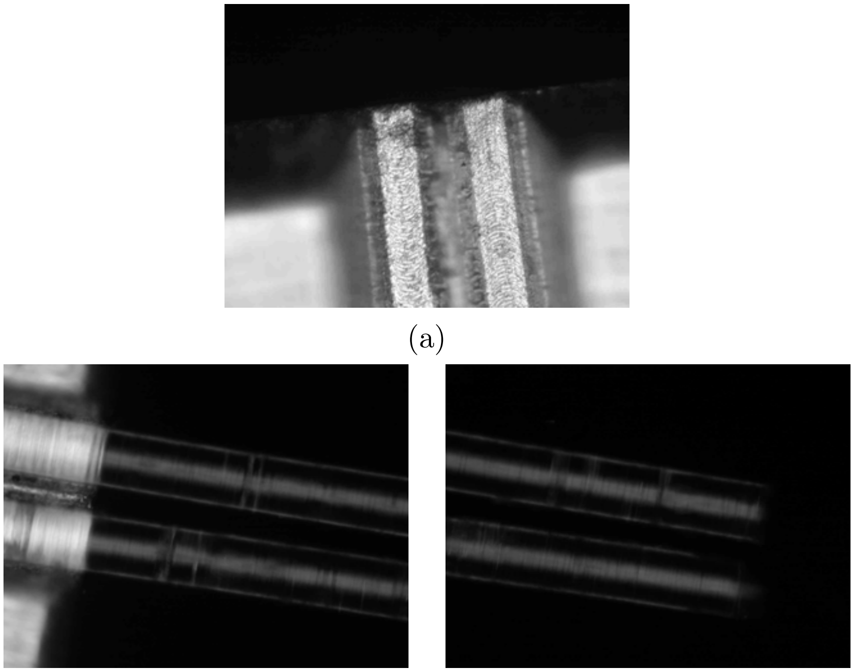

(a)

(b)

(c)

Figure 2.8: The microscopic pictures of v-grooves in Design A. (a) v-grooves only, (b) v-grooves with fibers therein, (c) fiber ends.

We look at Design A first. A major advantage of this design is that the pair of v-grooves do not need micron precision for the separation of the input and output fibers. Figure 8 shows microscopic v-groove pictures with and without fibers therein. Because the v-grooves have an angle with respect to each other, the fibers can be slid in the v-grooves to compensate for an error in the fiber end lateral separation over a range of 50 μm. In this way, it saves cost to use the metal v-groove compared to precision fiber ferrules.

Another advantage of the system is the mechanical stability of the system. In Design A, only one spacer ring is placed between two half-ball lenses for separation, while the filter is directly affixed to one of the half ball. In comparison, in Design C, two half-ball lenses are separated by a pair of spacer rings with a filter sandwiched in between. Due to the three intermediate elements, the angular alignment between left and right half balls is generally worse in Design C than in Design A. This is one of the factors explaining why Design A had a transmission-path insertion loss much better than Design C. The ferrules used in Design C separate fibers at 250 μm, corresponding to an object height of 125 μm, while in Design A the equivalent object height is zero. The higher the object height, the more the aberration. Another important source of extra loss in Design C is that the TEC fibers might suffer some damage when they were put into the ferrules. Since the TEC fibers are weakened in structure due to the extra thermal process [26], this type of damage easily occurs and may give fairly large losses (In Design A, the v-grooves holding the fibers are open-structures). We did not investigate this factor in depth since Design C was studied only for comparative purpose.

However, comparing the figures after deducting reflection losses, the reflection path in Design A has a slightly higher insertion loss than that in Design C. This can be explained as follows. In Design A, we used low precision metal v-grooves to hold the input and output fibers, as shown in Fig. 2.9 (a). If the separation of center line of v-grooves is $d + \Delta d$ (in actual machining, a pre-offset was added to make sure Δd always positive) at the edge of the metal strip, we can slide the input and output fibers outward until the centers of their endfaces are separated by d exactly. However, due to the resolution and measurement limitation of the microscope that was used in the alignment process, it is difficult to fix the separation d to an accuracy below 5 μm (note TEC fiber core size is 35 μm). Thus a moderate extra loss occurred. If SMFs are used, we can always convert such a translational misalignment into an angular misalignment.

In Fig. 2.9 (b), we illustrate such a situation. Ideally, the fibers are separated by d, and tilted at an angle θ_1. If the actual separation is $d - \Delta d (\Delta d$ can be positive or negative), one can rotate the metal strip holding two fibers counterclockwise by

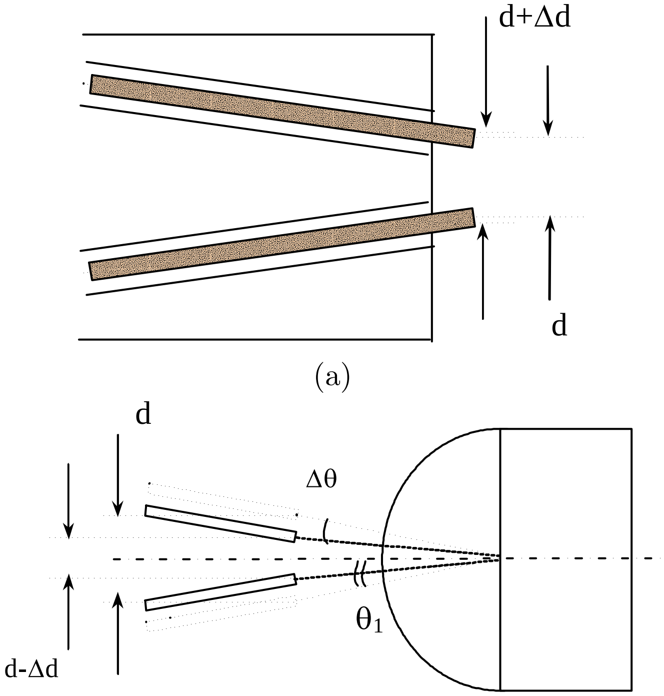

(a)

(b)

Figure 2.9: Compensation of mechanical inaccuracy and misalignments in v-groove assembly. (a) Compensation of mechanical inaccuracy. (b) Angular mismatch for SMF case: The ideal fiber position are shaded, at a separation d. The actual separation is $d - \Delta d$, Which is equivalent to an angular deviation of $\Delta\theta$ from the ideal angle θ_1. Note unlike for the TEC fibers, the single-mode fibers are not sensitive to angular misalignments. *Figures are not drawn to scale.*

an angle $\Delta\theta$, which can be computed from Δd by differentiating Eq. (2.1a). The rotation should centered around the end of upper fiber, accompanied with certain translational movement. Then the lower fiber solely has an angular misalignment of $2\Delta\theta$, with a translational misalignment, whose effect is negligible. For $\Delta d = 3\mu m$, one can estimate $\Delta\theta$ is about 0.03^o, which is much smaller than the NA angle of a SMF. The drop fiber does not suffer from such a problem because its location relative to the input fiber is not constrained by the v-grooves.

Comparing various designs in Table 2.3, it is obvious that Design B has superb optical performance compared to Design C. However, compared to Design A, Design B needs precision ferrules and 2 spacer rings between filters and ball lenses, which adds to the cost and the packaging complexity. If furnished with better alignment tools and AR coated lenses, Design A can yield best results with extremely low insertion losses in both paths. But it needs TEC fibers. We should point out that it is possible to produce an optical design for a full-ball lens OADM with SMF fibers tilted with respect to the axis. And the preceding discussion clarifies the solution to the misalignment problem of using tilted v-grooves to hold SMF fibers. Therefore, this design will eliminate the costs of TEC fibers in Design A and precision fiber ferrules in Design B. The performance is expected to be better than Design B. Further study is needed for some packaging issues associated with the open structure of the v-grooves that hold the fibers. The fiber endfaces can be angle-polished to reduce the return loss to below 50dB, but the fiber tilting angles must be changed accordingly.

2.4.3 100-GHz OADM

Due to the limited availability of 100 GHz WDM filters, most of our comparative experiments are conducted using 200 GHz filters. Experiments on 100 GHz OADMs are done for Design B only. The spectra of reflection and transmission paths are

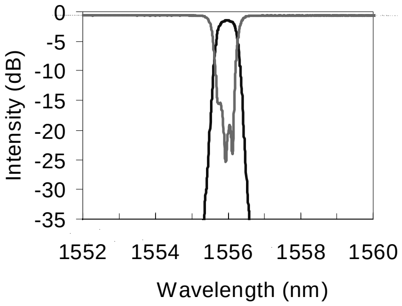

Figure 2.10: Measured spectra of a 100-GHz ball-lens based OADM

presented in Fig. 2.10. The 0.5-dB bandwidth is about 0.35 nm. The peak insertion losses are 0.54 dB and 1.44 dB for the reflection and transmission paths, respectively. The 30 dB stopband width is 1.15 nm for the transmission path. From 1555.80 nm to 1556.14 nm, the isolation of the reflection path is better than 15 dB. The PDL and ripple are less than 0.25 dB.

2.5 Conclusion

We studied a variety of designs and implementations of ball-lens based OADMs. At a lower cost, the ball-lens based OADMs were demonstrated to have competitive performance compared to GRIN-lens based OADMs. The ball-lens based OADMs also save one third of the alignment work in packaging. Among various designs, Design A does not need micron precision ferrule and is mechanically simple and stable, but needs TEC fibers. Design B has lower aberration under the same conditions and does not need TEC fibers, but needs precision ferrules.

2.6 Appendix: Defocusing and RMS spot size for seidel aberrations

The root-mean-square spot radius was used here because it usually yields a better estimate of actual spot size compared to the spot radius given simply by the transverse aberration of the marginal rays. Consider an on-axis point. When the third order aberration is dominant in an uncorrected positive lens, the marginal rays focus at a point closer to the lens than the paraxial focus. We can assume that the rays that exit the lens at an angle θ with respect to the optical axis focus at $z = f(\theta)$. For convenience, we choose the paraxial focus to be the origin of z axis, therefore, $f(0) = 0$. For a system dominated by the third order aberration, $f(\theta) = -A\theta^2$, where A is a constant. For simplicity, we always take the sign of θ to be positive in this part of calculation. Suppose an image plane is placed at z. To the accuracy of third order, a ray exiting the lens at an angle θ strikes this plane at the radius

$$r(z,\theta) = |[z - f(\theta)]\theta|$$

For a system with small image NA and reasonable third order aberration, the exit pupil has an area element $dA_e = f_0^2\theta d\theta d\phi$, where ϕ is the azimuthal angle and f_0 is the focal length of the lens. To the accuracy of third order, the root-mean-square spot size can be evaluated

$$\begin{aligned} r_{rms}^2(z) &= \frac{\int r^2(z,\theta)dA_e}{\int dA_e} \\ &= \frac{1}{2}\alpha^2 z^2 + \frac{2}{3}A\alpha^4 z + \frac{1}{4}A^2\alpha^6 \qquad (2.8) \end{aligned}$$

The minimum RMS spot size is found to be $\frac{1}{6}A\alpha^3$ when the image plane is located at $z = -\frac{2}{3}A\alpha^2$. These results are slightly different from those obtained by measuring a spot through the maximum aberration [22]. Note the absolute values of the transverse and longitudinal aberrations for marginal rays are $A\alpha^3$ and $A\alpha^2$, respectively. The RMS spot size at the paraxial focus is half of the transverse aberration of marginal rays, which is obtained by evaluating Eq. (2.8) at $z = 0$. By moving the image receiving plane along the axis for a distance of two thirds of the longitudinal aberration, the RMS spot size is reduced 3 times. The above analysis is valid for an off-axis object as well, as long as the object height $h << f \cdot NA$.

Chapter 3

Optical Add-Drop Processes in Symmetrical Waveguide-Resonator Systems

3.1 Introduction

Filters based on photonic crystals (PC) have been discussed for single-channel OADM applications. Fan *et al.* first proposed a structure of two parallel waveguides in a photonic crystal, with two resonators in-between [13], as illustrated in Fig. 3.1. Light of multiple wavelengths enters one waveguide from a fiber. By proper design of the resonators, light of a specific wavelength will be transferred to the other waveguide completely, while light of the other wavelengths will pass through the original waveguide and be coupled into another fiber. Quantum Green's function has been used to analyze the problem. On the other hand, simulations were performed to study PC-based single-channel OADMs [27] and demultiplexers. [28]

A major problem encountered in current simulations of these devices is that, for many ports, the light transfer efficiencies are fairly low; that is, a significant por-

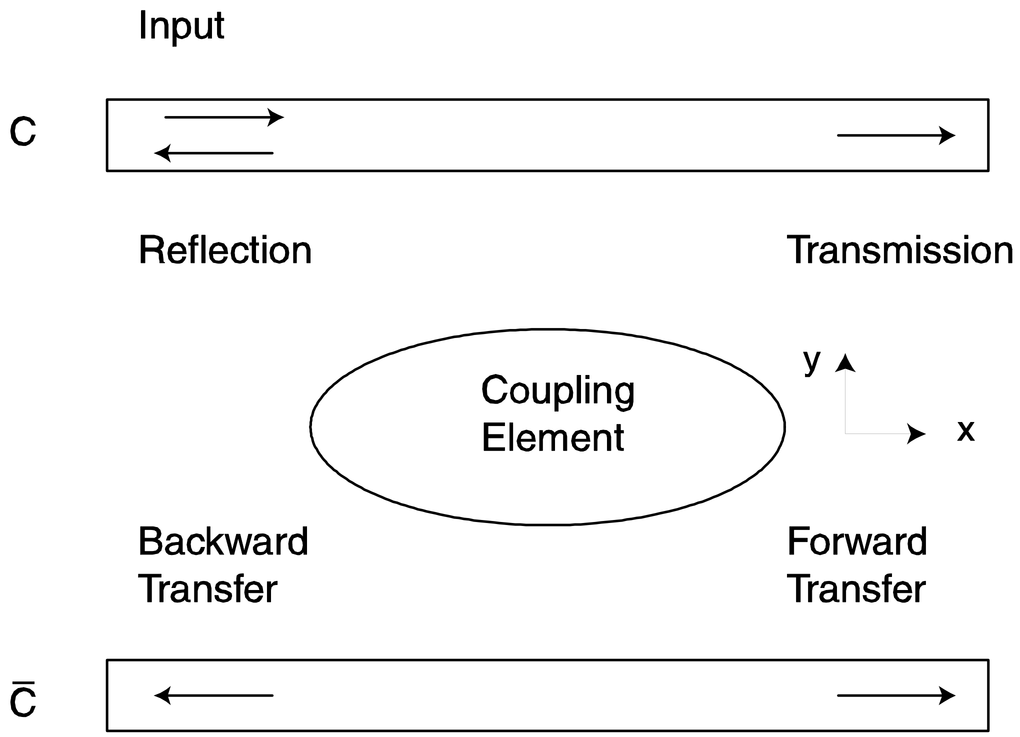

Figure 3.1: The schematic of a single-channel OADM presented in Ref. [29]. Light enters the upper waveguide. Through interaction with the resonator system in the middle, light of a specific wavelength is transferred to the other waveguide. Other wavelengths remain in the original waveguides. A portion of light is reflected in the upper waveguide.

tion of light is lost in the non-optimized transfer processes. Also, for a multi-channel OADM, one needs to ensure that no light of the dropped wavelengths remains in the pass-through port, which may be hard to achieve in simulations (This is not a problem for a demultiplexer, in which all wavelengths of light are separated into their respective ports and there is no need for a pass-through port). Clearly, an analytic theory is needed to explore the characteristics and ultimate performance of PC-based multi-channel OADMs, and to give direction to the simulation efforts. New system architecture may be needed to overcome the limitations of the old systems.

In this chapter, I propose a class of new structures that can add-drop multiple wavelengths simultaneously. In such a structure having an n-fold symmetry, n pairs of resonators and n waveguides are arranged in a symmetrical manner. An n-fold structure can achieve 100% add and drop of light at $n-1$ different wavelengths. These structures also provide a way of suppressing the remnant light intensity at the pass-through port for the bands of dropped frequencies. Such improvement in optical isolation is very important for WDM applications. Realizing these structures based on photonic crystals will yield compact integrated devices although they can be realized by conventional waveguiding structures also.

Simulations demonstrated that (nearly) perfect (100%) channel-drop efficiency could be achieved in a carefully designed photonic crystal based OADM, in excellent agreement with the theory [13, 29]. However, an in-depth examination of the theory still leaves some questions unanswered. Three major issues are:

(1) The direct coupling between waveguides was neglected in the theory, which seemed to lack a quantitative argument.

(2) According to the theory, a peak drop efficiency of 100% requires that the even and odd modes are strictly degenerate (*i.e.* , they must have the exactly same frequency). However, in all simulated examples, the actual modes discernibly departed from strict degeneracy while the peak drop

efficiency degradation was almost indistinguishable.

(3) The model assumes that the couplings between waveguides and cavities are all frequency independent. As John pointed out, when casted into certain Hamiltonian form, the electromagnetic wave equation has a photonic "potential energy" that is frequency dependent [30]. This means that the aforementioned couplings will also have a frequency-dependent coupling constant. Finding a general method that can solve this model with arbitrary frequency-dependent coupling constants is a challenging problem.

The first question was later explained by Y. Xu *et al.* from Dr. Yariv's group at Caltech [31]. Some additional discussions are presented in Sec. 3.2.3. The second and third questions will be examined in Sec. 3.3.6.

3.2 Optical channel-drop process in a photonic crystal waveguide-resonator system

In this section, we will review the theoretical framework proposed by Fan *et al.* and the major conclusions of the theory. Part of the theory will be presented in a form slightly different from the original work by Fan *et al.* Such a form will heuristically lead us to a more general theory, around which the main body of this chapter will be built upon.

The schematic diagram of a channel drop system is shown in Fig. 3.1 (from Ref. [29], redrawn with adaptation). The system is composed of two identical waveguides, labeled C and $\overline{C}$, side coupled through a resonator system. Following the notation of Fan *et al.* [29], the propagating states (or guided modes) with a wavevector k in two single-mode waveguides are labeled $|k\rangle$ and $|\overline{k}\rangle$, respectively. The resonator system supports cavity modes (or resonator modes, localized states) labeled as $|c\rangle$. The complete Hamiltonian for such a system is

$$
\begin{aligned}
H &= H_0 + V \\
H_0 &= \sum_k \omega_k |k\rangle\langle k| + \sum_c \omega_c |c\rangle\langle c|, \qquad (3.1)\\
V &= \frac{1}{L}\sum_{k_1 \neq k_2} V_{k_1,k_2} |k_1\rangle\langle k_2| + \sum_{c_1\neq c_2} V_{c_1,c_2}|c_1\rangle\langle c_2| + \frac{1}{\sqrt{L}}\sum_{k,c}\left[V_{c,k}|c\rangle\langle k| + V_{k,c}|k\rangle\langle c|\right].
\end{aligned}
$$

where ω_k is the frequency of the state $|k\rangle$, and L is the length of the waveguides. The interaction coefficient V_{ab} (a and b can be either localized or propagating states) satisfies the conjugate relation $V_{ab} = V_{ba}^*$. The sum over k includes both waveguides. The direct coupling between two waveguides is represented by V_{k_1,k_2}, which we shall neglect following Fan *et al.* [13, 29]. The justification of this omission will be presented in Sec. 3.2.3.

When the direct coupling is absent, the Lippmann-Schwinger equation for this Hamiltonian can be solved with ease if there are only a small number of cavity modes. The essence of the treatment is the reduction of the dimension of effective interaction matrix to the number of cavity modes. In this section, the case of four cavity modes will be reviewed.

By employing symmetry, we can transform the states of the two waveguides into the following two kinds of states:

$$|ke\rangle = \frac{1}{\sqrt{2}}(|k\rangle + |\overline{k}\rangle), \qquad (3.2a)$$

$$|ko\rangle = \frac{1}{\sqrt{2}i}(|k\rangle - |\overline{k}\rangle), \qquad (3.2b)$$

where e and o denote the states that have even or odd parity with respect to the mirror plane normal to y axis. Because of the symmetry of the system, the Hamiltonian commutes with the reflection M_y with respect to the mirror plane perpendicular to y axis,

$$[H, M_y] = 0.$$

There can not be interaction between even and odd states. Therefore, in the new basis, the Hamiltonian has the form

$$\begin{aligned}
H &= H_0 + V \\
H_0 &= \sum_{k,\delta_y} \omega_{k,\delta_y} |k\delta_y\rangle\langle k\delta_y| + \sum_{c} \omega_c |c\rangle\langle c|, \\
V &= \sum_{c_1 \neq c_2} V_{c_1,c_2} |c_1\rangle\langle c_2| + \frac{1}{\sqrt{L}} \sum_{k,\delta_y,c} \left[V_{c,k\delta_y} |c\rangle\langle k\delta_y| + V_{k\delta_y,c} |k\delta_y\rangle\langle c| \right].
\end{aligned} \tag{3.3}$$

where the sum over δ_y includes the even and odd states.

3.2.1 Solve the Lippmann-Schwinger Equation

To calculate the transmitted, transferred, or backscattered wave, one needs to solve the Lippmann-Schwinger equation, which relates the scattered wave function $|\psi\rangle$ to the incoming wave $|k\rangle$

$$|\psi\rangle = |k\rangle + \frac{1}{\omega_k - H_0 + i\epsilon} V |\psi\rangle \equiv T|k\rangle \tag{3.4}$$

where ω_k is the frequency of the incoming wave (for this part, we use k only to denote a propagating state and omit δ_y for convenience as there is no necessity of distinguishing the even and odd states), and ϵ is an infinitesimally small positive number introduced to enforce the outgoing boundary condition for the scattered wave.

The Lippmann-Schwinger Equation can be solved iteratively. As a result, the T matrix can be represented as a sum of an infinite series

$$T_{k'k} = \sum_{m=0}^{\infty} \langle k'| \left(\frac{1}{\omega_k - H_0 + i\epsilon} V \right)^m |k\rangle \tag{3.5}$$

Since there is no direct coupling between the propagating states, it is possible to reduce the scattering process to the subspace spanned by the cavity modes. With a bit laborious derivation, the sum in Eq. (3.5) can be computed, which gives the following form for the transition matrix [31, 32]

$$T_{k'k} = \delta_{k'k} + \frac{1}{\omega_k - \omega_{k'} + i\epsilon} \sum_{c_1,c_2} V_{k',c_2} G_{c_2,c_1}(\omega_k) V_{c_1,k} \tag{3.6}$$

where

$$G_{c_1,c_2}(\omega) = \langle c_2| \frac{1}{\omega - H + i\epsilon} |c_1\rangle \tag{3.7}$$

is the Green's function in the subspace of cavity modes. In other words, G can be expressed as an $N_c \times N_c$ matrix. Here N_c is the number of cavity modes. The Green's function has the standard form

$$G = (1 - G^0\Sigma)^{-1} G^0 \tag{3.8}$$

and G^0 and Σ are also in the subspace of the cavity modes. The unperturbed Green's function is

$$G^0_{c_1,c_2}(\omega) = \frac{1}{\omega - \omega_{c_1} + i\epsilon} \delta_{c_1,c_2} \tag{3.9}$$

and the self-energy is summed exactly [31, 32] to be

$$\Sigma_{c_1,c_2} = V_{c_1,c_2} + \frac{1}{L} \sum_q V_{c_1,q} \frac{1}{\omega - \omega_q + i\epsilon} V_{q,c_2} \tag{3.10}$$

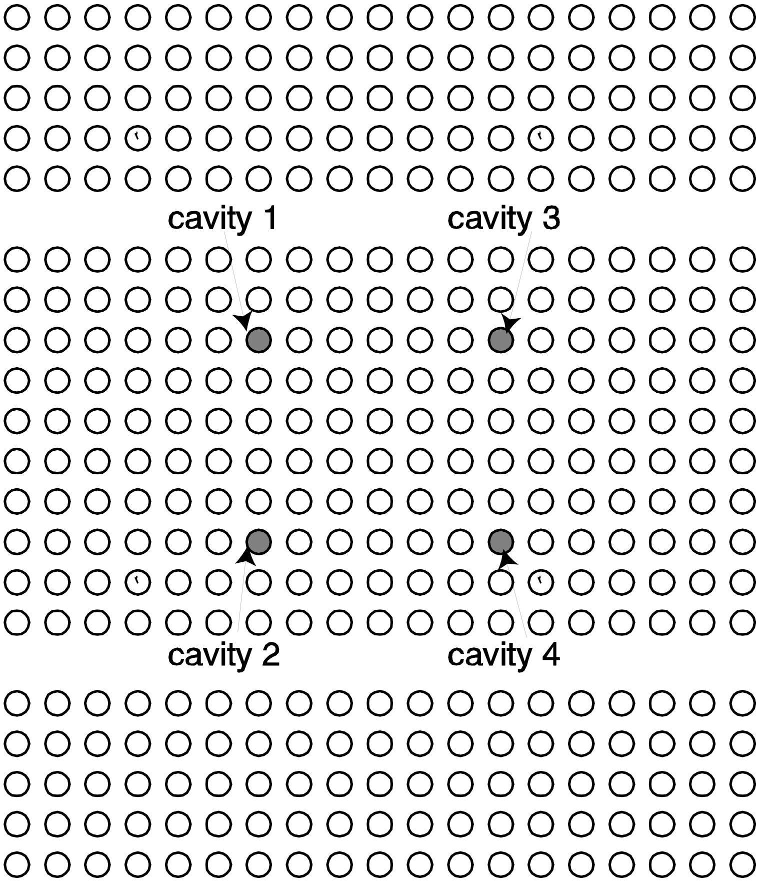

Figure 3.2: Four-cavity photonic crystal based OADM proposed in Ref. [29]

3.2.2 Four-Cavity Filter: Flat-top Transfer Function

For the system with four cavity modes [29] as shown in Fig. 3.2, one advantage is the transfer function of the channel drop system can be improved compared to a two-cavity system. Generally, flat-top and sharp edges are desirable features of the transfer function. The derivations in this section mostly follow the steps of Fan *et al.* [29]. However, we will use the symmetrized modes $|k\delta_y\rangle$ instead of the original modes $|k\rangle$ and $|\overline{k}\rangle$, which allows us to see the connection with a more general model to be presented later.

Assume the four states represented by $|\delta_x\delta_y\rangle$ have the symmetry δ_x and δ_y

with respect to the mirror planes normal to x and y axes, respectively. Here, δ_x and δ_y take values e or o, which indicate even and odd states, respectively.

For such a system, both the $|ke\rangle$ and $|ko\rangle$ waves are scattered by the resonator system. For this system, the self-energy is given by

$$\Sigma_{\delta'_x\delta'_y,\delta_x\delta_y} = \frac{1}{L}\sum_{q,\delta''_y} \frac{V_{\delta'_x\delta'_y,q\delta''_y} V_{q\delta''_y,\delta'_x,\delta'_y}}{\omega - \omega_{q\delta''_y} + i\epsilon}. \tag{3.11}$$

Because $V_{\delta'_x\delta'_y,q\delta''_y} = V_{\delta'_x\delta'_y,q\delta'_y}\delta_{\delta'_y,\delta''_y}$, we have $\Sigma_{\delta'_x\delta'_y,\delta_x\delta_y} = \Sigma_{\delta'_x\delta_y,\delta_x\delta_y}\delta_{\delta_y,\delta'_y}$. By changing the sum over q to over $-q$, one easily shows the self-energy is also diagonal with respect to the δ_x subspace. Therefore, the self-energy has the form

$$\Sigma_{\delta'_x\delta'_y,\delta_x\delta_y} = \frac{1}{L}\sum_{q} \frac{V_{\delta_x\delta_y,q\delta_y} V_{q\delta_y,\delta_x,\delta_y}}{\omega - \omega_{q\delta_y} + i\epsilon}\delta_{\delta_x,\delta'_x}\delta_{\delta_y,\delta'_y}. \tag{3.12}$$

The diagonal element of the self-energy is given by

$$\begin{aligned}
\Sigma_{\delta_x\delta_y,\delta_x\delta_y} &= \frac{1}{2\pi}\int \frac{dq}{d\omega_{q\delta_y}} d\omega_{q\delta_y} \frac{|V_{q\delta_y,\delta_x\delta_y}|^2}{\omega - \omega_{q\delta_y} + i\epsilon} \\
&= \frac{\mathcal{P}}{2\pi}\int \frac{d\omega_{q\delta_y}}{g(\omega_q\delta_y)} \frac{|V_{q\delta_y,\delta_x\delta_y}|^2}{\omega - \omega_{q\delta_y}} - i\frac{|V_{q(\omega)e,\delta_x\delta_y}|^2}{g(\omega)} \\
&= -\Delta\omega_{\delta_x\delta_y} - i\gamma_{\delta_x\delta_y}
\end{aligned} \tag{3.13}$$

where the real part is the principle value of the integral and $g(\omega)$ is the group velocity at frequency ω.

Now the Green's function in the reduced space of the cavity modes is

$$G_{\delta_x\delta_y,\delta_x\delta_y}(\omega) = \frac{1}{\omega - \widetilde{\omega}_{\delta_x\delta_y} + i\gamma_{\delta_x\delta_y}} \tag{3.14}$$

where the renormalized frequency and the linewidth of the cavity modes are given by

$$\widetilde{\omega}_{\delta_x\delta_y}(\omega) = \omega_{\delta_x\delta_y} + \frac{\mathcal{P}}{2\pi}\int dq \frac{|V_{\delta_x\delta_y,q\delta_y}|^2}{\omega - \omega_{\delta_x\delta_y}} \tag{3.15}$$

$$\gamma_{\delta_x\delta_y}(\omega) = \frac{1}{g(\omega)}|V_{\delta_x\delta_y,q\delta_y}|^2 \tag{3.16}$$

The forward transmission for the $|k\delta_y\rangle$ states is

$$\begin{aligned}
\langle x=\infty|T|k\delta_y\rangle &= \sum_{k'\delta_y'}\langle x=\infty|k',\delta_y'\rangle\langle k'\delta_y'|T|k\delta_y\rangle \\
&= \lim_{x\to\infty}\frac{L}{2\pi}\int dk'|\delta_y\rangle\frac{1}{\sqrt{L}}e^{ik'x}\left[\delta_{k'k} + \frac{1}{L}\frac{\sum_c V_{k'\delta_y,\delta_x\delta_y}G_{\delta_x\delta_y}V_{\delta_x\delta_y,k\delta_y}}{\omega_{k\delta_y}-\omega_{k'\delta_y}+i\epsilon}\right] \\
&= \lim_{x\to\infty}\frac{1}{\sqrt{L}}e^{ikx}|\delta_y\rangle\left[1-\frac{i}{g(\omega_{k\delta_y})}\sum_{\delta_x}V_{k\delta_y,\delta_x\delta_y}G_{\delta_x\delta_y}(\omega_{k\delta_y})V_{\delta_x\delta_y,k\delta_y}\right] \\
&= \lim_{x\to\infty}\frac{1}{\sqrt{L}}e^{ikx}|\delta_y\rangle\left[1+\chi_{e,\delta_y}+\chi_{o,\delta_y}\right] \\
&= \lim_{x\to\infty}\langle x|k\delta_y\rangle\left[1+\chi_{e,\delta_y}+\chi_{o,\delta_y}\right]
\end{aligned}$$

where the scattering amplitude due to the state $|\delta_x\delta_y\rangle$ is

$$\begin{aligned}
\chi_{\delta_x\delta_y} &= -\frac{i}{g(\omega_{k\delta_y})}V_{k\delta_y,\delta_x\delta_y}G_{\delta_x\delta_y c}(\omega_{k\delta_y})V_{\delta_x\delta_y,k\delta_y} \\
&= -\frac{i\gamma_{\delta_x\delta_y}}{\omega_{k\delta_y}-\widetilde{\omega}_{\delta_x\delta_y}+i\gamma_{\delta_x\delta_y}}. \qquad (3.17)
\end{aligned}$$

Similarly, one readily verifies that the reflected wave is

$$\langle x=-\infty|T|k\delta_y\rangle = \lim_{x\to\infty}\langle x|k\delta_y\rangle\left[\chi_{e,\delta_y}-\chi_{o,\delta_y}\right] \tag{3.18}$$

Following Fan *et al.*, we enforce the so-called accidental degenerate condition

$$\widetilde{\omega}_{ee} = \widetilde{\omega}_{oe},\ \widetilde{\omega}_{eo} = \widetilde{\omega}_{oo} \tag{3.19}$$

$$\gamma_{ee} = \gamma_{oe} = \gamma_{eo} = \gamma_{oo} \equiv \gamma \tag{3.20}$$

$$\widetilde{\omega}_{ee} - \widetilde{\omega}_{oo} = 2\gamma \tag{3.21}$$

Obviously, it follows

$$\chi_{e,\delta_y} \equiv \chi_{o,\delta_y}, \delta_y = e, \text{or } o.$$

This further yields

$$\begin{aligned} \langle x = -\infty | T | k\delta_y \rangle &= 0, \\ \langle x = \infty | T | k\delta_y \rangle &= \lim_{x \to \infty} \langle x | k\delta_y \rangle \left[1 + 2\chi_{e,\delta_y} \right] \end{aligned}$$

We have been using symmetrized states $|k\delta_y\rangle$. To calculate the scattering amplitudes in the original waveguides, we need the inverse relation of Eq. (3.2)

$$|k\rangle = \tfrac{1}{\sqrt{2}}(|ke\rangle + i|ko\rangle), \tag{3.22a}$$

$$|\overline{k}\rangle = \tfrac{1}{\sqrt{2}}(|ke\rangle - i|ko\rangle), \tag{3.22b}$$

Now it is straightforward to compute the scattering amplitudes. For example, if light enters the upper waveguide with unity amplitude, one first use Eqs. (3.2) to transform the incoming waveguide mode into the symmetrized modes; then the scattering amplitudes are calculated for the symmetrized modes; finally the symmetrized modes that have been produced by the scattering process are transformed back into the real modes in the upper and lower waveguides. Note that Fan *et al.* computed the scattering amplitudes for the original modes directly, without utilizing the fully symmetrized modes. As we shall see in the following section, the formulation that involves fully symmetrized modes can be generalized to a generic symmetric system.

For the incoming beam $|k\rangle$ in the upper waveguide, the outgoing waves are computed to have the amplitudes

$$\begin{aligned}
\text{Forward transmission} &: 1 + (\chi_{ee} + \chi_{oo}) \\
\text{Forward transfer} &: (\chi_{ee} - \chi_{oo}) \\
\text{Backward transmission} &: 0 \\
\text{Backward transfer} &: 0
\end{aligned}$$

The forward transmission is thus given by

$$\frac{(\omega - \omega_0)^4}{(\omega - \omega_0)^4 + 4\gamma^4} \tag{3.23}$$

where $\omega_0 = \frac{1}{2}(\widetilde{\omega}_{ee} + \widetilde{\omega}_{oo})$ and the forward transfer is given by

$$\frac{4\gamma^4}{(\omega - \omega_0)^4 + 4\gamma^4} \tag{3.24}$$

which has the form of "maximum-flat" function, as shown in Fig. 3.3.

The backward reflection and backward transfer waves both vanish. However, one should bear in mind that these formulae are only approximately correct near the region of resonance. Because, generally speaking, the renormalized resonance frequency and the linewidth of the cavity modes are functions of $\omega_{k\delta_y}$, the frequency of the propagating states interacting with this cavity modes. This was testified by the difference in the intensity profiles (or the actual linewidth) between $|ee\rangle$ and $|oe\rangle$, or $|eo\rangle$ and $|oo\rangle$ states [29]. Note this difference also exists in the case of two cavity modes. However, in the case of two cavity modes, this doesn't affect the 100% transmission at the resonance because by forcing the degeneracy of the even and odd cavity modes at resonance only, the contributions from these two modes are exactly

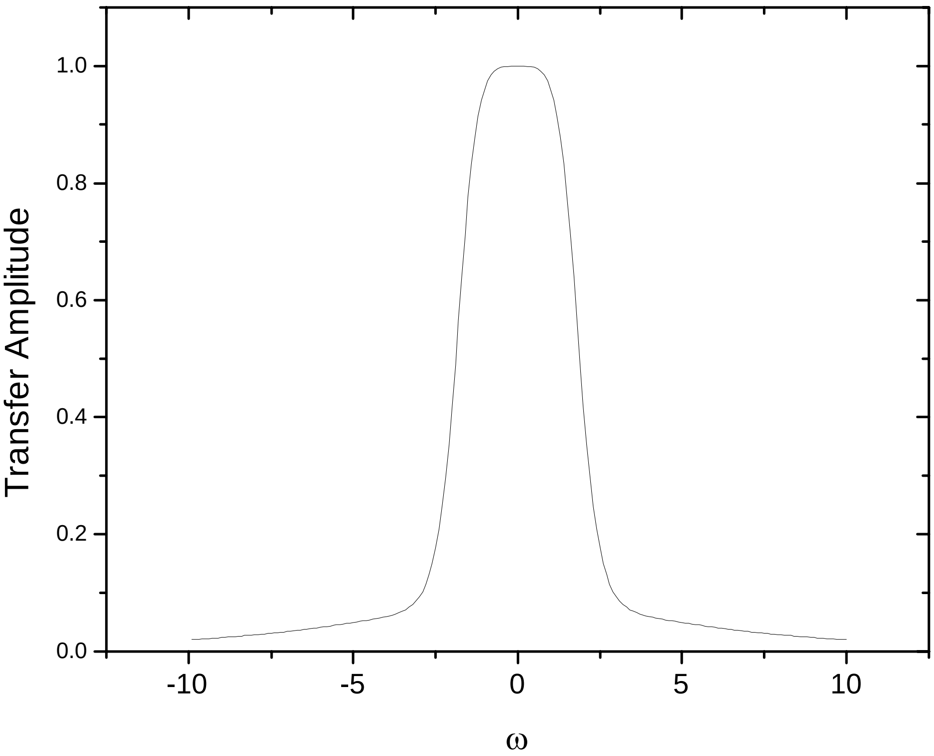

Figure 3.3: The amplitude of light that is transferred to the lower waveguide is described by the maximum-flat function

the same at resonance. Even we introduce the coupling between the propagating states, this is still true because the odd propagating states are not scattered, we need to force the degeneracy at one frequency, i.e. ω_{ke}.

3.2.3 Direct coupling between waveguides

In the foregoing discussions, the direct coupling between the waveguides is assumed negligible. At first glance, this is not apparent. For example, we assume that the wavefunction of a cavity state has the form

$$\psi_c(x) = \langle x|c\rangle \propto \beta_c e^{-\beta_c r},$$

where r is the distance from the center of the cavity, and β_c is a constant. Also assume the wavefunction of the propagating mode of a waveguide has the form

$$\psi_k(x) = \langle x|k\rangle \propto \sqrt{\frac{\beta_k}{L}} e^{ikx-\beta_k|y|},$$

where β_k is another constant. By calculating the overlap integral between respective states, one can estimate the direct coupling strength

$$\langle k_1|V|k_2\rangle \propto \frac{\sin(\Delta kL/2)}{\Delta kL/2} e^{-\beta_g d} \sim \delta_{k_1,k_2} e^{-\beta_g d}, \tag{3.25}$$

where $\Delta k = k_2 - k_1$. In a similar fashion, the indirect coupling strength is computed as

$$|\langle k|V|c\rangle|^2 \sim \frac{1}{\beta' L} e^{-\beta' d},$$

where $\beta' = \max(\beta_c, \beta_k)$. The exponential terms which are the primary factors in two equations are comparable if β_k and β_c are comparable. This means that the direct coupling can not be neglected. This problem was clarified by Xu *et al.* [31] for a general case.

There is another noteworthy point that Xu *et al.* did not touch. According to Eq. (3.25), the direct coupling between k_1 mode in the upper waveguide and k_2 mode in the lower waveguide occurs only if their wavevectors are the same, this is clearly a consequence of the momentum conservation. We note that the argument of Xu *et al.* is based on energy(or frequency) conservation, which can be applied to more general cases when the two waveguides are not parallel.

3.3 Optical add-drop in a symmetrical waveguide-resonator system with frequency dependent coupling constants: a general theory

3.3.1 Introduction

Fan *et al.* explored the possibility of generating higher order flat top functions by increasing the number of cavities, and hence the number of cavity modes [33]. But as the number cavity modes increases, a simplifying assumption was made that each waveguides couples to the pair of cavities closest to it. They also neglected the coupling V_{c_1,c_2} between most of cavity modes. Khan *et al.* worked further on this problem with a simplification stemming from a theory of resistor networks. In my master's study, I proposed a system with three waveguides and three pairs of cavities forming a 3-fold symmetric structure as illustrated in Fig. 3.4.

In this model, I assumed that the cavity modes had frequency independent parameters(resonant frequency and linewidth), and the system overall was lossless. Group theory was not fully employed to analyze the system. The output amplitudes of the "output" and "drop1" ports are given in Figs. 3.5 & 3.6. Through tuning the ratio b of the linewidths of different cavity modes, the transfer curves can be optimized for the drop1 and output ports. Figures 3.5 and 3.6 clearly demonstrate that the three-waveguide OADM has a much better performance than the two-

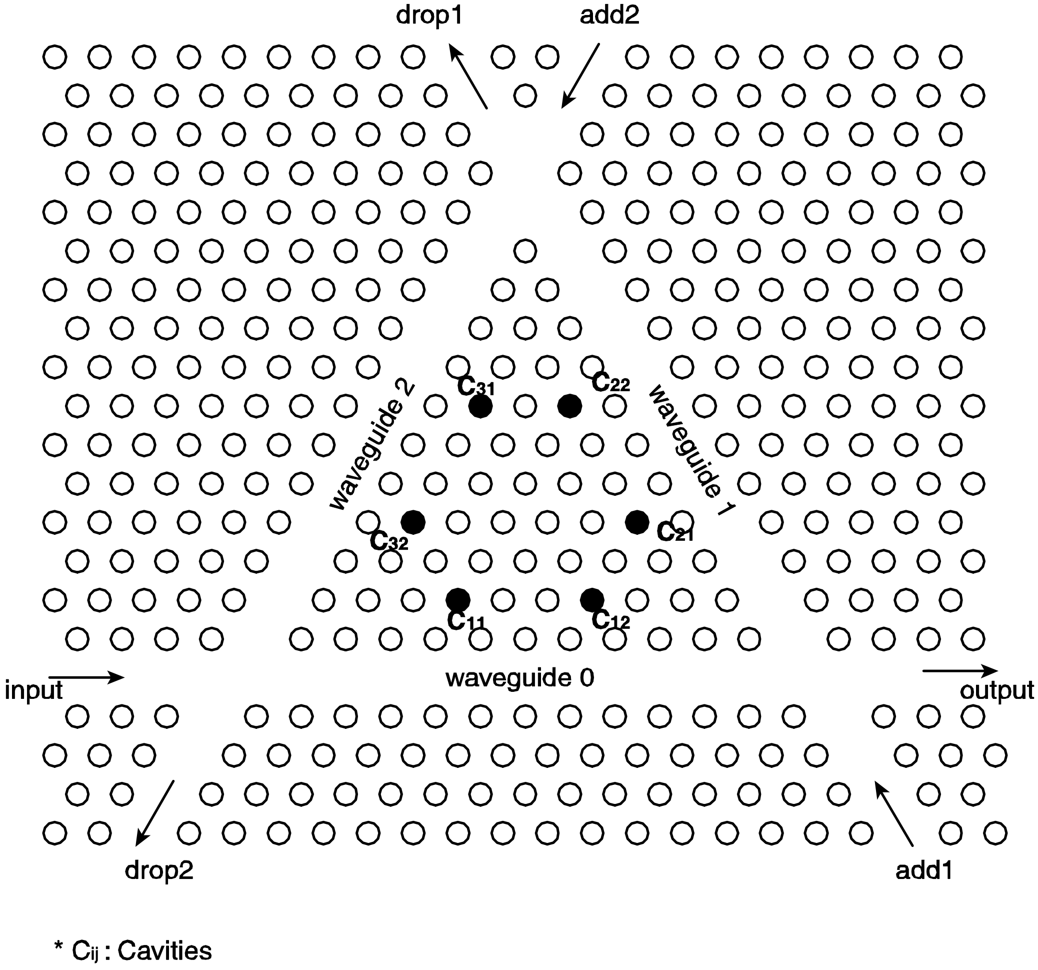

Figure 3.4: Layout of a photonic crystal based 3-fold symmetric optical add-drop multiplexer Each of the 3 waveguides are accompanied by a pair of cavities. Light of multiple wavelengths comes in from the input port. Two wavelengths are dropped to the drop1 and drop2 ports, respectively. Light of the corresponding wavelengths is coupled in through the add1 and add2 ports, then merges with the undropped light and reaches output port altogether.

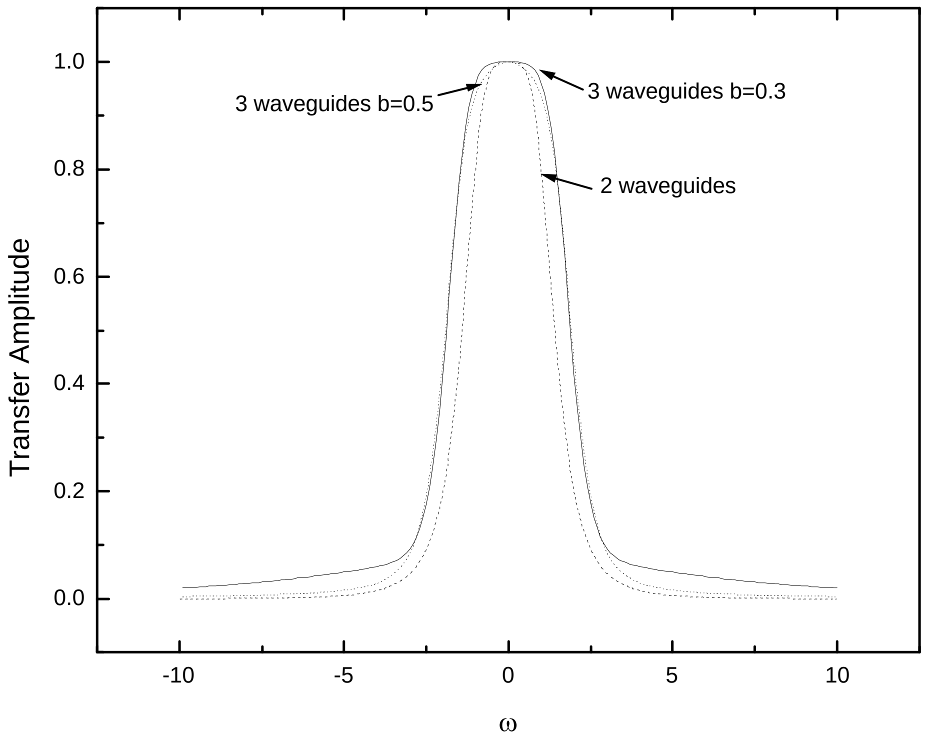

Figure 3.5: Transfer curve for the drop1 port for various linewidth ratios compared with the corresponding curve for a two-waveguide OADM

waveguide OADM. However, the transfer curve for the drop2 port is totally useless. This three-waveguide OADM virtually functions as a single-channel OADM, the add2 and drop2 ports are wasted. In the above optimization process, a single parameter is varied, namely the ratio of linewidths between certain cavity modes. By varying more parameters, one may improve the drop2 port. However, there were some intrinsic limitations of the underlying assumptions and the analysis techniques, which shall be exposed and overcome in this section.

Group theory, which governs the symmetry properties of any physical system, sheds light on this problem. From the point view of group theory, it is the orthogonality of different symmetric states that results in the decoupling of cavity modes. In a desirable situation, each decoupled cavity mode is an eigenstate of the

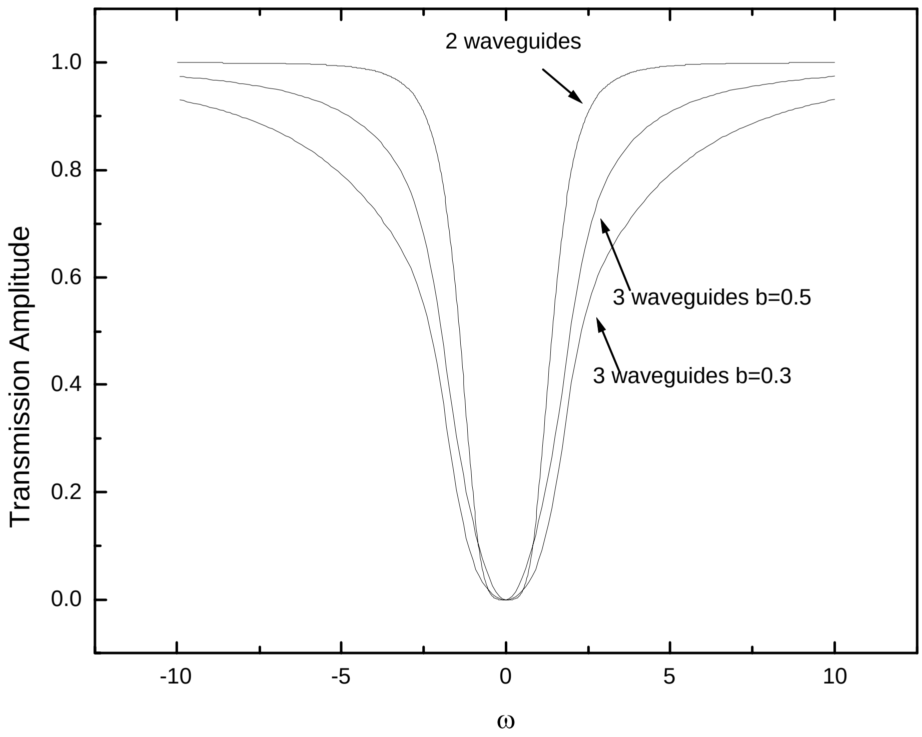

Figure 3.6: Transfer curve for the output port for various linewidth ratios compared with the corresponding curve for a two-waveguide OADM

complete set of commuting operators(CSCO) of the symmetry group of the Hamiltonian. And due to symmetry, the propagating modes couple only to those cavity modes that have the same symmetry in mode profile as their own. The symmetry naturally diagonalizes the Hamiltonian in the reduced space of cavity modes. Unfortunately, this happens only if the symmetry group is abelian, which means all symmetry operations of the group commute with each other, or in a group theory jargon, all irreducible representations of the group are one-dimensional.

As we shall see, generally, the symmetry groups encountered in real OADM systems are not abelian, which brings forth a significant degree of difficulty in analysis.

3.3.2 Hamiltonian and group theoretical analysis

Consider a system having n waveguides on the edges of a regular n-polygon. Inside the polygon, near the middle of each edge, there are a pair of identical cavities, each having a single resonant mode. Their modes can be combined to form one even and one odd mode with respect to the mirror plane between them. With the resonators placed symmetrically, the system possesses a symmetry of point group C_{nv}. Figure 3.4 illustrates the case $n = 3$. An n-fold system is described by a Hamiltonian [13]

$$\begin{aligned} H &= H_0 + V, \\ H_0 &= \sum_{m=0}^{n-1} \sum_{k} \omega_k |mk\rangle\langle mk| + \sum_{m=0}^{n-1} \sum_{c} \omega_{mc} |mc\rangle\langle mc|, \\ V &= \sum_{m,m'} \sum_{c,c'} (1 - \delta_{m,m'}\delta_{c,c'}) V_{mc,m'c'} |mc\rangle\langle m'c'| \\ &\quad + \sum_{m,m'} \sum_{k,c} \left[V_{mc,m'k} |mc\rangle\langle m'k| + V_{m'k,mc} |m'k\rangle\langle mc| \right], \end{aligned} \tag{3.26}$$

where $|mk\rangle$ is a propagating mode with wavevector k and frequency ω_k in waveguide $\#m$. The mode $|mc\rangle$ is a cavity mode of the resonator pair next to waveguide $\#m$, $c = e,\ o$ for the even and odd modes, respectively; ω_{mc} is its frequency. The coefficients $V_{mc,m'c'}$ and $V_{mc,m'k}$ measure the coupling between the corresponding modes. Note that we now place k as the second label in the "bras" and "kets." This is different from the labeling in the previous sections. We have neglected the coupling between the propagating modes of different waveguides as discussed by Xu *et al.* [31] For $n > 2$, the symmetry operations of the group C_{nv} do not commute with each other, therefore irreducible representations of dimensions higher than unity appear. [34] In simple words, a set of basis functions that are the eigenstates of all symmetry operations do not exist. Furthermore, the standard choice of basis function related to irreducible representation is found not helpful here. We nevertheless find that the eigenfunctions of C_n operations offer convenience to analysis. One can readily show, constructed from $|mk\rangle$, the modes

$$|\alpha k\rangle = \frac{1}{\sqrt{n}} \sum_{m=0}^{n-1} e^{-i\frac{2\pi}{n}\alpha m} |mk\rangle,\ \alpha = 0,\ 1, ...,\ n-1 \tag{3.27}$$

are eigenfunctions of C_n. One can construct $|\alpha e\rangle$ and $|\alpha o\rangle$ from $|me\rangle$ and $|mo\rangle$ similarly. The reflection M_j by the mirror plane bisecting waveguide $\#j$ gives

$$M_j|\alpha c\rangle = \pm e^{-i\frac{2\pi}{n}2\alpha j}|\overline{\alpha}c\rangle, \quad c = e, o \tag{3.28}$$

where $\overline{\alpha} \equiv -\alpha$, and the plus and minus signs are for e and o, respectively. A similar relation holds for $|\alpha k\rangle$. Note $|\alpha e\rangle$ and $|\alpha o\rangle$ are no longer eigenfunctions of any M_j, which brings difficulties to analysis. From these, it follows $V_{\alpha k,\beta k'} = V_{\alpha c,\beta c'} = V_{\alpha k,\beta c} = 0,$ for $\alpha \neq \beta$. As a side note, a mirror operation in general incurs a change from α to $-\alpha$. In terms of the symmetrized basis, the Hamiltonian can be simplified to

$$
\begin{aligned}
H &= H_0' + V', \\
H_0' &= \sum_{\alpha=0}^{n-1} \sum_{k} \omega_k |\alpha k\rangle\langle \alpha k| + \sum_{\alpha=0}^{n-1} \sum_{c=c_1,c_2} \omega_{\alpha c} |\alpha c\rangle\langle \alpha c|, \\
V' &= \sum_{\alpha} \sum_{k,c} \left[V_{\alpha c,\alpha k} |\alpha c\rangle\langle \alpha k| + V_{\alpha k,\alpha c} |\alpha k\rangle\langle \alpha c| \right].
\end{aligned}
\tag{3.29}
$$

The decoupled $|\alpha c_1\rangle$, $|\alpha c_2\rangle$ can be expressed as

$$|\alpha c_1\rangle = u_\alpha |\alpha e\rangle + v_\alpha |\alpha o\rangle, \tag{3.30}$$

$$|\alpha c_2\rangle = -v_\alpha^* |\alpha e\rangle + u_\alpha^* |\alpha o\rangle, \tag{3.31}$$

where u_α and v_α are complex coefficients satisfying $|u_\alpha|^2 + |v_\alpha|^2 = 1$, their values can be easily solved given $V_{\alpha e,\alpha o}$.

3.3.3 Solution of the Lippmann-Schwinger equation

Solving the Lippmann-Schwinger equation [35], one finds the transfer matrix has elements $T_{\alpha' k',\alpha k} = T_{\alpha k',\alpha k} \delta_{\alpha' \alpha}$,

$$T_{\alpha k',\alpha k} = \delta_{k',k} + \sum_{c,c'} \frac{V_{\alpha k',\alpha c'} G_{\alpha c',\alpha c}(\omega_k) V_{\alpha c,\alpha k}}{\omega_k - \omega_{k'} + i\epsilon}, \tag{3.32}$$

where the Green's function is determined by

$$(G^{-1})_{\alpha c',\alpha c}(\omega) = (\omega - \omega_{\alpha c} + i\sigma_{\alpha c})\delta_{c' c} - \Sigma_{\alpha c',\alpha c}, \tag{3.33}$$

where $\sigma_{\alpha c}$ represents the cavity loss. [31, 36] Note $\sigma_{\alpha c}$ may depend on frequency because the coupling coefficients $V_{m_1 c, m_2 c'}$ usually are frequency dependent due to the nature of "photonic potential." [30] The self-energy is

$$\Sigma_{\alpha c',\alpha c}(\omega) = \sum_k V_{\alpha c',\alpha k} \frac{1}{\omega - \omega_k + i\epsilon} V_{\alpha k,\alpha c}.$$

The scattered wave is given by $|\psi^{(+)}_{\alpha k}\rangle = \sum_{k'} T_{\alpha k',\alpha k} |\alpha k'\rangle$. The forward and backward scatterings for $|\alpha k\rangle$ are

$$\begin{aligned} \langle x = +\infty|\psi^{(+)}_{\alpha k}\rangle &= \langle x|\alpha k\rangle \\ &\quad + \frac{-iL}{v(\omega_k)} \langle x|\alpha k\rangle \sum_{c,c'} V_{\alpha k,\alpha c'} G_{\alpha c',\alpha c}(\omega_k) V_{\alpha c,\alpha k}, \\ \langle x = -\infty|\psi^{(+)}_{\alpha k}\rangle &= \frac{-iL\langle x|\alpha \overline{k}\rangle}{v(\omega_{\overline{k}})} \sum_{c,c'} V_{\alpha \overline{k},\alpha c'} G_{\alpha c',\alpha c} V_{\alpha c,\alpha k}. \end{aligned}$$

To further the calculation, we temporarily *assume* $\Sigma_{\alpha c',\alpha c}$ is diagonal. We will revisit this issue shortly. We denote the diagonal terms as $\Sigma_{\alpha c,\alpha c}(\omega) = \Delta\omega_{\alpha c}(\omega) - i\gamma_{\alpha c}(\omega)$.

In an OADM, we require the backscattering amplitude vanish or

$$V_{\alpha \overline{k},\alpha c_1} V_{\alpha c_1,\alpha k} G_{\alpha c_1,\alpha c_1}(\omega_k) + V_{\alpha \overline{k},\alpha c_2} V_{\alpha c_2,\alpha k} G_{\alpha c_2,\alpha c_2}(\omega_k) = 0. \tag{3.34}$$

Following Fan *et al.*, accidental degeneracy conditions [36] are adopted, $\omega_{\alpha c_1} + \Delta\omega_{\alpha c_1} = \omega_{\alpha c_2} + \Delta\omega_{\alpha c_2}$, $\gamma_{\alpha c_1} = \gamma_{\alpha c_2}$, and $\sigma_{\alpha c_1} = \sigma_{\alpha c_2}$. Due to these equalities between c_1 and c_2, we hereafter use c to represent c_1 or c_2 unless a confusion occurs. Now solving Eq. (3.34) gives

$$\frac{V_{\alpha k,\alpha e}}{V_{\alpha k,\alpha o}} = -\frac{V_{\alpha \overline{k},\alpha e}}{V_{\alpha \overline{k},\alpha o}} = e^{i\eta_{\alpha k}}, \tag{3.35}$$

where $\eta_{\alpha k}$ is an arbitrary phase angle. We express this condition in the representation of $|\alpha e\rangle$ and $|\alpha o\rangle$ because we find that in this representation the condition has, surprisingly, an invariant form. Even more surprising is that this condition automatically ensures the self energy is diagonal, $\Sigma_{\alpha c_1,\alpha c_2} = 0$. Note this is not a circular reasoning. One can verify Eq. (3.35) simultaneously satisfies $\Sigma_{\alpha c_1,\alpha c_2} = 0$ and Eq. (3.34), two apparently independent equations.

The symmetrized forward scattering amplitude is calculated as

$$A_{\alpha k} = 1 + \frac{-2i\gamma_{\alpha c}}{\omega_k - (\omega_{\alpha c} + \Delta\omega_{\alpha c}) + i(\gamma_{\alpha c} + \sigma_{\alpha c})}, \tag{3.36}$$

where $\Delta\omega_{\alpha c}$, $\gamma_{\alpha c}$, and $\sigma_{\alpha c}$ are evaluated at ω_k. Now consider a light of a single wavelength coupled into waveguide #0 with unity amplitude. This light can be decomposed into symmetrized modes by Eq. (3.27), thus the forward scattering amplitude in waveguide $\#m$ is

$$a_m = \frac{1}{n}\sum_\alpha A_{\alpha k} e^{-i\frac{2\pi}{n}\alpha m}. \tag{3.37}$$

The sum of the scattering amplitudes is found to be independent of the terms $\alpha \neq 0$,

$$\sum_m a_m = A_{0k}. \tag{3.38}$$

The sum of the intensities is given by

$$\sum_m |a_m|^2 = \frac{1}{n}\sum_\alpha |A_{\alpha k}|^2. \tag{3.39}$$

If $\sigma_{\alpha c} = 0$ for all α, then all $|A_{\alpha k}| = 1$, total light intensity is conserved after scattering. Generally, in a passive device, all $\sigma_{\alpha k}$'s and $\gamma_{\alpha k}$'s are non-negative, hence $|A_{\alpha k}| \leq 1$, an optical loss occurs.

The equation $a_m = A_{0k_1}\delta_{mm_1}$ characterizes that a complete drop from waveguide #0 to waveguide $\#m_1$ occurs at wavelength $2\pi/k_1$. Such a drop occurs if and only if

$$A_{\alpha k_1} = A_{0k_1} e^{i\frac{2\pi}{n}\alpha m_1},\ \alpha = 0,\ 1,\ ...,\ n-1. \tag{3.40}$$

Two interesting cases are considered. First, consider an ideal lossless case with $\sigma_{\alpha c} = 0$ for all α. However, it turns out that the "optical isolation" in this case is very poor. Physically, it means that when a *lossless* drop occurs from waveguide $\#0$ to $\#m_1$ at ω_{k_1}, it is impossible to keep the light intensities in other $n-2$ waveguides to infinitesimally small over a band of frequency centered at ω_{k_1}. Without loss of generality, consider a drop to waveguide $\#1$. Over a frequency range centered at the dropped frequency, assume the light intensities are essentially zero in all waveguides except $\#0$ and $\#1$, which yields $a_0 = A_{0k} - a_1$ from Eq. (3.38). Inverting Eq. (3.37), one can calculate $A_{\alpha k}$ from a_m's. Then

$$|A_{\alpha k}|^2 = 1 + 2|a_1|(|a_1| - \cos\delta)(1 - \cos\frac{2\pi\alpha}{n}) - 2|a_1|\sin\frac{2\pi\alpha}{n}\sin\delta \qquad (3.41)$$

where $\delta \equiv \arg A_{0k} - \arg a_1$. One readily shows that for $n \geq 3$, $|A_{\alpha k}| = 1$ can not hold for all α when $|a_1|$ varies continuously on interval $[1-\eta, 1]$, where η is an arbitrarily small, positive number. This contradicts our lossless assumption according to Eq. (3.39).

Illustrated in Fig. 3.5 is a case where one drop port has relatively good transfer function, but the transfer curve for the other drop port is totally useless. The preceding proof predicts that for a lossless system, no matter how one varies the parameters in attempt to optimize the transfer curves, desirable curves can not be simultaneously achieved in both waveguides. This was exactly my experience in the early study of this 3-fold symmetric system. After failing to optimize the transfer curves in all attempts, I began to realize that maybe these curves could not be simultaneously optimized. Later I proved my intuition rigorously. The proving process also supplied me with the insight that optical loss, when deliberately introduced, can lend itself to the benefit of device performance, as we shall see.

The second case we will study is that $\sigma_{0k} = 0$ and all other $\sigma_{\alpha c}$'s take non-negative values. This case is no longer lossless. But we will see that loss is essentially introduced only in certain frequency ranges in favor of the performance of the device. To begin with, we show that $\sigma_{0k} = 0$ places a constraint on the phase angle relation between A_{0k} and a_1. In fact, one finds from Eq. (3.41)

$$|A_{\alpha k}|^2 + |A_{-\alpha k}|^2 - 2 = 8|a_1| \sin^2 \frac{\alpha\pi}{n} (|a_1| - \cos\delta). \tag{3.42}$$

Since the left hand side must not be positive, one obtains $\cos\delta \geq |a_1|$. Subject to this constraint, a variable phase $\delta(\omega)$ can be chosen. However, we can show it equivalent to the case where $\delta' = 0$ and $a'_m = e^{-i\delta} a_m$ for all m when solving for $A_{\alpha k}$'s. Note the overall phase does not change the filter intensity profile $|a_m|^2$. Also if δ is a constant, it must be zero since $max(|a_1|) = 1$, hence we have $A_{0k} = \frac{a_1}{|a_1|}$ by the definition of δ.

For the second case, given the desired $a_m(\omega)$ curves, one can solve for $\widetilde{\omega}_{\alpha c} = \omega_{\alpha c} + \Delta\omega_{\alpha c}$, $\sigma_{\alpha c}$, $\gamma_{\alpha c}$ as functions of frequency. Then one can design the resonators having these characteristics. Consider the system shown in Fig. 3.4. Assume

$$a_1(\omega) = \frac{-i\gamma_a e^{i\phi_a}}{\omega - \omega_a + i\gamma_a}, \tag{3.43}$$

$$a_2(\omega) = \frac{-i\gamma_b e^{i\phi_b}}{\omega - \omega_b + i\gamma_b}, \tag{3.44}$$

$$a_0(\omega) = A_{0k} - a_1 - a_2 \tag{3.45}$$

where ω_a, ω_b, γ_a, and γ_b are constants. Hereafter, the frequency range where the magnitude of a_1 is appreciable will be referred to as band a. A similar reference applies to band b. The appearance of variable phase angles $\phi_a(\omega)$ and $\phi_b(\omega)$ is necessary for the continuity of the solved quantities at the frequencies between band a and b. We require these phases remain constant over their respective bands, varying only when the corresponding amplitudes are negligible. Therefore, they practically have no effect on the delay or other properties of the filter. [37]

3.3.4 Numerical examples

To solve for $\widetilde{\omega}_{\alpha c}$, $\sigma_{\alpha c}$, $\gamma_{\alpha c}$, one substitutes Eq. (3.36) and Eq. (3.3.3) into Eq. (3.37), noting ω in Eq. (3.3.3) is just ω_k in Eq. (3.36). Due to the constraints discussed above(constant in-band ϕ_a, ϕ_b, non-negative $\gamma_{\alpha c}$, $\sigma_{\alpha c}$, and continuity), the solution is not straightforward. Certain optimization algorithms can be used. As an example, we plot one set of solutions for a system with parameters $\gamma_a = \gamma_b$, $\omega_b - \omega_a = 11\gamma_a$ in Fig. 3.7. However, infinite sets of $\widetilde{\omega}_{\alpha c}$, $\sigma_{\alpha c}$, $\gamma_{\alpha c}$ can produce the desired filter. This gives plentiful freedom in design. Such freedom is very desirable when this theory is combined with finite difference time-domain(FDTD) simulation to design a planar lightwave circuit. The larger the space of the solutions, the easier some of these solutions can be achieved with simple resonators like those formed by varying the diameters of the defect "atoms." A detailed investigation of the space of the solutions is beyond the scope of this work.

To obtain the set of solutions in Fig. 3.7, we have applied the additional constraint that $\widetilde{\omega}_{\alpha c}$'s are constant when the magnitudes of filter transfer functions are appreciable and we connect $\widetilde{\omega}_{\alpha c}$'s of different bands using linear interpolation(other smooth interpolations are possible). In Figure 3.7 (d), the transmission spectrum for each port is reconstructed from the solutions presented in (a)-(c). One sees 100% drops occur at ω_a and ω_b. Assume ω_a and ω_b differ by 0.8nm(centered at 1.55μm), then the 0.5dB and 30dB bandwidths are 0.05nm and 0.93nm, respectively. The sum of the three spectra shows prominent loss. And the loss penalizes only the pass-through port in the bands of dropped wavelengths, as indicated by a reference lossless pass-through spectrum. From the total intensity spectrum(which is also the total loss) at the bottom of Fig. 3.7(d), we can also see that the loss increases fast in the transition regions between passbands and stopbands. This feature certainly steepens the transition part of the transfer curve(for the pass-through port), which is desirable for most applications. The isolation at the 0.5dB edges of each passband

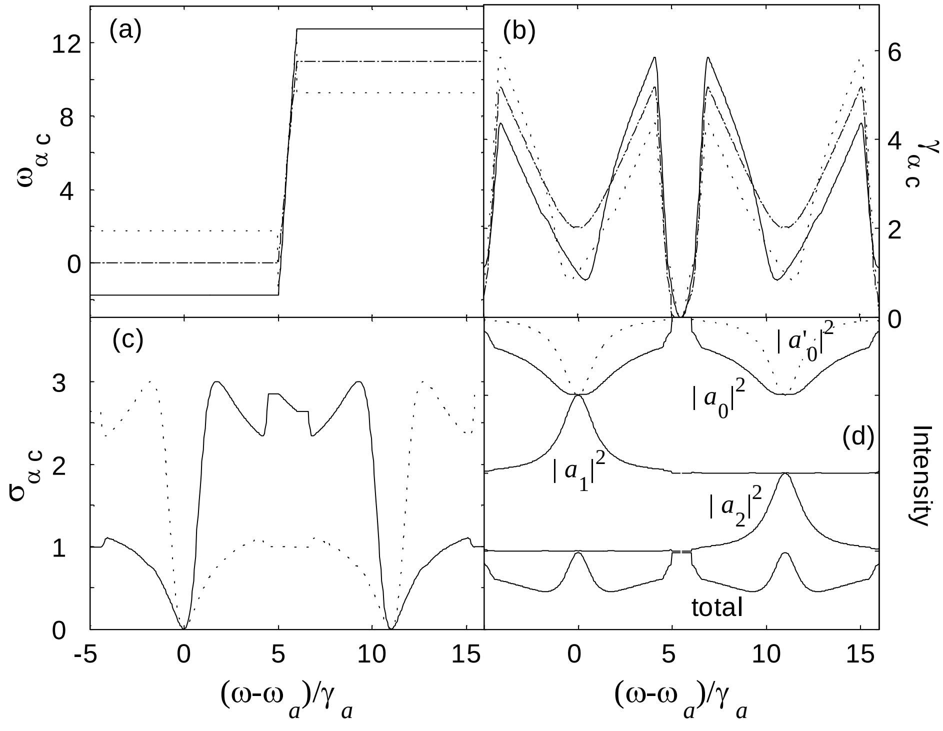

Figure 3.7: The solved $\widetilde{\omega}_{\alpha c}$, $\sigma_{\alpha c}$, and $\gamma_{\alpha c}$ are plotted in (a)-(c). Dashdot, solid, and dotted lines correspond to $\alpha = 0$, 1, and 2, respectively. Reconstructed spectra are shown in (d) on a linear scale, where $|a_0'|^2$(dotted line) is a reference lossless spectrum. Each intensity reaches maximum 1 and minimum 0, except the total intensity, whose minimum is greater than zero.

is enhanced from -9.6dB(for $|a_0'|^2$) to -25dB(for $|a_0|^2$). For an FDTD-aided design, one may start with designing resonators having spectra closest to the set of exact solutions, then design the whole system. Without the first step, the algorithm may have no clue to search a big design space and may never converge. Lossless constraint should not be applied across the spectrum, as discussed. Many techniques in traditional filter design [37] can facilitate the OADM design, including minimax approaching, prototyping and frequency warping.

Higher order Butterworth functions are highly desirable for an add-drop filter. [29, 33] Our theory is also applied to an $n = 3$ OADM having a third-order Butterworth intensity profile $\frac{\gamma_a^6}{(\omega-\omega_a)^6+\gamma_a^6}$. Figure 3.8 presents the solved spectra of the two relevant ports in one band, along with a reference lossless spectrum for the pass-through port. Again, the remnant light in the pass-through port is desirably reduced in the dropped frequency ranges. Also seen is the obvious flat-top lineshape of the drop port compared to the first-order case. The 0.5dB to 30dB bandwidth ratio now increases to 0.22, indicating a much sharper transition between the passband and stopband.

3.3.5 A linear transformation perspective

In the foregoing discussions, it was assumed that incoming light is present only at the input port. However, for a true multi-channel OADM, incoming light of different wavelengths may enter into other "add" ports as well (see Fig. 3.4), which requires further analysis.

From an engineering point of view, a simple picture of the proposed n-fold symmetric system is that for a set of input amplitudes c_l, a set of output amplitudes d_m are given through a linear transformation $\mathcal{T}$, as illustrated in Fig. 3.9. Here c_0 represents the incoming light amplitude in the input port while c_1, c_2, ..., c_{n-1} represent the incoming light amplitudes in the correspondingly numbered add ports.

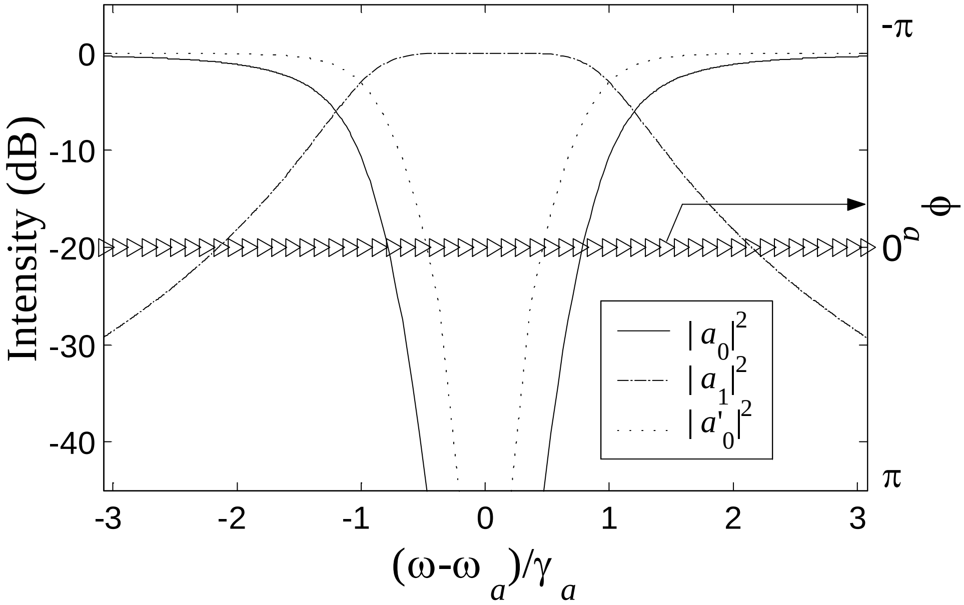

Figure 3.8: Reconstructed spectra for the 3rd-order Butterworth case, $\phi_a \equiv 0$ for appreciable $|a_1|$.

Similarly, d_0 is the outgoing light amplitude in the output port, and other d_m's are for the corresponding drop ports. In this way, all the ports of the original system are included in the model of this linear system(if the backscatterings are not all exactly zero, then another n output ports must be introduced in Fig. 3.9. This case will not be discussed here for simplicity, though it is not difficult to analyze.) Physics plays the role of calculating the transformation coefficients. Actually, the following analysis will show that when the transformation is expressed as a matrix $\mathcal{T}$, the matrix elements must be

$$\mathcal{T}_{ml} = a_{m-l},$$

where a_m is given in Eq. (3.37).

To start, we rewrite the scattering state in the following form for the case

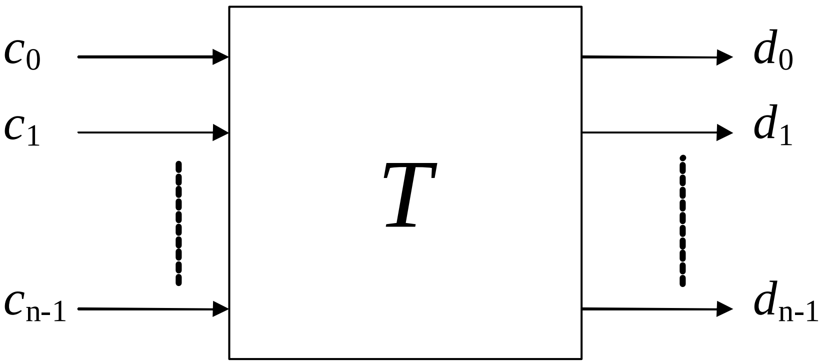

Figure 3.9: A linear system perspective of a multichannel OADM

that light enters waveguide #0 only

$$|\psi_{0k}^{(+)}\rangle = \sum_m a_m |mk\rangle. \tag{3.46}$$

The scattering state $|\psi_{0k}^{(+)}\rangle$ is a collection of the outgoing scattering waves in all waveguides. In terms of the linear system shown in Fig. 3.9, this means

$$\text{input} : c_0 = 1, \quad c_1 = c_2 = ... = c_{n-1} = 0, \tag{3.47}$$

$$\text{output} : d_m = a_m, \quad m = 0,\, 1,\, 2,\, ...,\, n-1, \tag{3.48}$$

Now consider another case where light enters into the "add1" port only(no light entering the input port). As the system is complete symmetric, under a cyclic permutation of the waveguide labels, we may regard the "add1" port as the input port. Then one easily finds that the scattering state for such a case is (expressed in the original waveguide labeling)

$$|\psi_{1k}^{(+)}\rangle = \sum_m a_{m-1} |mk\rangle \tag{3.49}$$

In terms of the linear system shown in Fig. 3.9, this means

$$\text{input}: \quad c_0 = 0, \quad c_1 = 1, \quad c_2 = c_3 = ... = c_{n-1} = 0, \tag{3.50}$$

$$\text{output}: \quad d_0 = a_{n-1}, \quad d_1 = a_0, \quad d_2 = a_1, ..., \; d_{n-1} = a_{n-2}. \tag{3.51}$$

Similarly, we can derive the scatter state for a general case where light enters l-th add port only,

$$|\psi_{lk}^{(+)}\rangle = \sum_m a_{m-l}|mk\rangle \tag{3.52}$$

Now if light enters multiple ports simultaneously, as described by the following input state

$$|\phi_{in}\rangle = \sum_l c_l|lk\rangle, \tag{3.53}$$

Based on the principle of linear superposition, the corresponding output state is given by

$$\begin{aligned} |\psi_{out}^{(+)}\rangle &= \sum_l c_l|\psi_{lk}^{(+)}\rangle \\ &= \sum_m d_m|mk\rangle \end{aligned} \tag{3.54}$$

Clearly, the scattering amplitude d_m in the output port of waveguide $\#m$, *i.e.* the "drop$m$" port, is given by

$$d_m = \sum_l a_{m-l}c_l \tag{3.55}$$

This proves that the transformation matrix has elements $\mathcal{T}_{ml} = a_{m-l}$.

Furthermore, we have the following relation

$$\begin{aligned} \sum_l \mathcal{T}_{m_1 l}\mathcal{T}^*_{l m_2} &= \frac{1}{n^2}\sum_{\alpha\alpha'}\left[\sum_l e^{i(2\pi/n)(\alpha-\alpha')l}\right] A_{\alpha k}A^*_{\alpha' k}e^{-i(2\pi/n)(\alpha m_1 - \alpha' m_2)} \\ &= \frac{1}{n}\sum_\alpha |A_{\alpha k}|^2 e^{-i(2\pi/n)\alpha(m_1-m_2)}. \end{aligned} \tag{3.56}$$

For a lossless system, the modulus of each symmetrized scattering amplitude is unity, $|A_{\alpha k}| = 1$, according to Eq. (3.36). It follows that the transformation $\mathcal{T}$ is represented by a unitary matrix

$$\sum_l \mathcal{T}_{m_1 l}\mathcal{T}^*_{l m_2} = \delta_{m_1 m_2} \tag{3.57}$$

3.3.6 Effect of departure from perfect accidental degeneracy

A general set of conditions have been given under which the backscattering amplitudes exactly vanish [19]. Part of the condition relies on the "accidental degeneracy" [29]. However, usually it is difficult to satisfy this condition *exactly* in simulations or design, even for an $n = 2$ case. Nonetheless, simulations have demonstrated close to 100% forward transfer and almost vanishing backscattering, despite the departure from perfect accidental degeneracy. A tolerance analysis is necessary in regard to how stably the forward and backward transfer spectra can retain its desirable features as a realistic system deviates from perfect accidental degeneracy.

First, let us define the difference of Green's functions between two cavity modes

$$\Delta G(\omega_k) \equiv G_{\alpha c_1,\alpha c_1} - G_{\alpha c_2,\alpha c_2} \tag{3.58}$$

It is straightforward to show that

$$|\Delta G(\omega_k)|^2 = \frac{\Delta\omega^2 + \Delta\Gamma^2}{\left[(\omega-\omega_1)^2 + \Gamma_1^2\right]\cdot\left[(\omega-\omega_2)^2 + \Gamma_2^2\right]}, \tag{3.59}$$

where for simplicity we have denoted $\omega_i = \widetilde{\omega}_{\alpha c_i}$, $\Gamma_i = \Gamma_{\alpha c_i} = \sigma_{\alpha c_i} + \gamma_{\alpha c_i}$, $\Delta\omega = \omega_2 - \omega_1$, and $\Delta\Gamma = \Gamma_2 - \Gamma_1$. The normalized backscattering intensity is proportional to

$$I_{back} \approx \gamma_1^2 |\Delta G(\omega)|^2, \tag{3.60}$$

where we have neglected the difference between γ_1 (*i.e.* $\gamma_{\alpha c_1}$) and γ_2 (*i.e.* $\gamma_{\alpha c_2}$).

In a passive system (*i.e.* no any electrical or optical power input other than the incoming wave in the input waveguide), the damping constants σ_i, γ_i, and Γ_i must be non-negative. Now it is straightforward to show that the maximum backscattering intensity, or strictly speaking an upper bound of the intensity, is given by

$$(I_{back})_{max} \approx \frac{\gamma_1^2\left(\Delta\omega^2 + \Delta\Gamma^2\right)}{\Gamma_1^2\Gamma_2^2} \leq \frac{\Delta\omega^2 + \Delta\Gamma^2}{\Gamma_2^2}, \tag{3.61}$$

The second inequality follows from $\gamma_1 \leq \Gamma_1$. It possible to derive a more accurate bound, which will involve quite complicated terms like $\max(\Gamma_1, \Gamma_2)$ or $\min(\Gamma_1, \Gamma_2)$ and will also have more convoluted dependence on $\Delta\omega$. However, it is usually sufficient to use Eq. (3.61) to estimate the backscattering intensity.

Evidently, the upper bound given in Eq. (3.61) is relatively tolerant to the departure from the accidental degeneracy. Even if both the frequency degeneracy and the linewidth degeneracy are violated by an amount as much as 10% of the value of the ideal linewidth, *i.e.* $\Delta\omega = \Delta\Gamma = 0.1\Gamma$, the normalized backscattering intensity does not exceed 1.7%. The actual number is usually even lower. Figure 3.10 illustrates such a case with 10% departure from degeneracy for both center frequency and linewidth. The actual peak intensity of the backscattering spectrum is about 1.3%, lower than the predicted value. In calculating the intensity in Fig. 3.10, we have assumed $\sigma_i = 0$, otherwise, the peak backscattering intensity will usually be even lower.

In conclusion, we have shown that even the accidental degeneracy is not perfectly realized, a low backscattering intensity can still be maintained. This applies to a system with any n(including $n = 2$).

3.3.7 Summary and further study

In this part of my doctoral study, a general theory of symmetrical waveguide- resonator systems that can be used for optical add-drop multiplexers was developed.

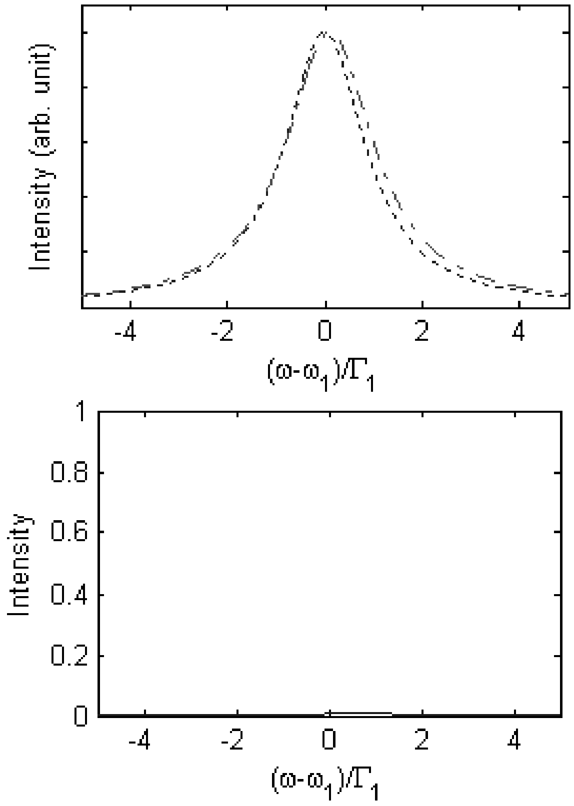

Figure 3.10: Backscattering amplitude for imperfect accidental degeneracy: $\omega_2 - \omega_1 = \Gamma_2 - \Gamma_1 = 0.1\Gamma_1$. (a) Resonant spectra of the two cavity mode, (b) Normalized backscattering amplitude, the actual peak intensity of the backscattering spectrum is about 1.3%, lower than the predicted value 1.7%

The major contributions of my work include:

(1) Developed a general technique for solving a general model where the coupling constants are frequency-dependent.

(2) Utilized group theory to extend the theory to systems with any C_{nv} symmetry, and succeeded in solving the general case where the even and odd modes are not completely decoupled.

(3) Discovered that such an add-drop multiplexer generally can not both be lossless and have low crosstalk in all ports. An interesting scheme was proposed to introduce loss deliberately, which actually improves the device performance compared to an ideal lossless OADM.

(4) Improved on the theoretical framework originally proposed by Fan *et al.* : addressed the problem of departure from perfect degeneracy, and explicitly derived a sum rule of scattering intensities(or normalization condition), and a convenient transformation matrix at the phenomenological level.

Further study of the system that we proposed requires extensive simulations. The current theory gives the important design guidelines, and some ideal solutions. A good numerical strategy is: With a given ideal solution, find an actual system whose parameters $\widetilde{\omega}_{\alpha c}$, $\sigma_{\alpha c}$, and $\gamma_{\alpha c}$ have frequency dependences closely resembling the ideal curves (such as the example shown in Fig. 3.7). Then one starts from this "tentative" actual system and search the whole design space to find the optimized solution (*i.e.* the optimally designed OADM).

Generally, the crosstalks and losses at the crossings of the waveguides will not be a concern for conventional [38] or PC-based [39] waveguides after optimizing the crossings properly, although further study is needed in actual systems.

Chapter 4

A General Theory of Light Refraction at a Surface of a Photonic Crystal

4.1 Introduction

Anomalous refraction of light at an interface between a photonic crystal [11, 12] and a homogeneous medium has been experimentally studied recently [14, 40]. The refraction angle was found to be sensitive to the incident angle and wavelength in certain cases. These phenomena were called "superprism" effect accordingly, and were proposed to be utilized for wavelength-division-multiplexing(WDM) and other applications [14, 40–45]. Furthermore, in some cases, the light beam refracts to the opposite side of the surface normal(see Fig. 4.1), which is expected only when the refractive index of one medium happens to be negative. This "negative refraction" phenomenon has been further studied in the context of building superlenses with photonic crystals [43].

The physics behind the anomalous refraction is related to the coupling of the incident light with the propagating modes of the photonic crystal. Although the light beam direction inside the PC can be fairly easily determined from the dispersion surface(*i.e.* the equi-frequency surface in the reciprocal space of the lattice) of the PC, other characteristics of photonic crystal(PC) refraction deserve further study [46]. Particularly important is the coupling amplitude (or insertion loss) of each excited mode, which is commonly calculated using Finite Difference Time Domain (FDTD) techniques [42–44]. However, FDTD simulations are often time consuming, and in many cases prohibitive for studying the anomalous refraction. To study such an effect that is characterized by high wavelength and angular sensitivity, fine spatial and temporal grids and a large simulation region are inevitable and are frequently beyond the capacity of commonly available computing facilities. Actually, no one has successfully calculated a transmission vs. wavelength, or transmission vs. angle curve based on FDTD simulations. In addition, FDTD simulations give the insertion loss values case by case–it cannot reveal some general features or trends when the wavelength, incident angle, or other parameters vary. In particular, the effect of varying surface orientation is never addressed, and the effect of various lattice type and surface termination is rarely seen in the literature. Like the refraction theories for homogeneous media(Snell's law) and layered media [47], a general PC refraction theory that can handle any type of lattice, any surface orientation, and any lattice termination is of fundamental importance from a basic research point of view. Such a theory also provides great flexibility in exploring novel device geometries [42] that have been proposed for valuable applications. Some conceptual novel device geometries are illustrated in Fig. 4.1, which clearly demonstrates the need for a theory that can deal with arbitrary surface orientation.

A variety of numerical and theoretical methods other than FDTD have been employed to study the transmitted optical field amplitude through photonic crystals, including the transfer matrix method [48–50], the scattering theory of dielectric

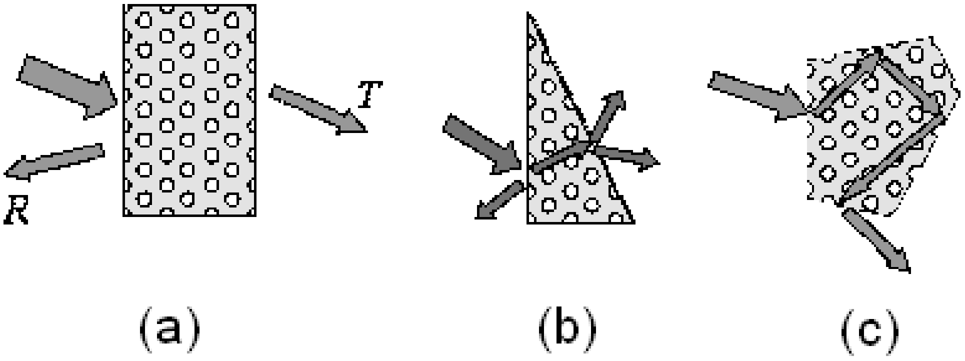

Figure 4.1: Conceptual sketches of novel device geometries. Entrance and exit surfaces may not be parallel, and light may reflect internally(may lose part of intensity during each reflection though) a number of times before it exits.

sphere/cylinder lattices [51–53], and the internal field expansion method [54, 55], as well as other methods [43–45].

Using these methods, plane-parallel slabs have been extensively studied for their transmission spectra, which exhibit interference features due to multiple reflections between two surfaces [51, 54–56]. However, in real devices, due to the finite width of the incident beam, the interference is often not in effect for a plane-parallel slab; see more explanation in Sec. 4.1.1 In addition, there are many cases where the entry and exit surfaces are not parallel. Study of single-surface transmission is necessary to understand and design a wider class of devices. As a matter of fact, in the situation of a half-space photonic crystal, the single-surface transmission is nothing but refraction.

Recently, single-surface transmission was studied in the context of endface coupling into a photonic crystal waveguide [50, 57]. In addition, the transfer matrix method was used to calculate the transmission spectrum of a single PC surface for cubic or rectangular lattices with special surface orientations such as (001) or (10) [49, 50, 53].

Despite the extensive progress, there is not a general PC refraction theory that covers arbitrary lattice type and surface orientation. As we shall see, *only when analytically studying the refraction problem in such a general case does the rich physics of PC refraction begin to unfold.* Our discussions focus on two-dimensional(2D) PCs, but most conclusions can be generalized to 3D easily.

In fact, many of these transmission problems are not new; some of them have been studied in X-ray diffraction [58] and electron diffraction [59]. However, in these diffraction phenomena, the complicated interactions between the probing wave and the matter hinder rigorous theoretical study. More fundamentally there is frequently no way to exactly calculate the diffraction of these probing waves by a single atom or molecule of corresponding material, owing to the nonlinearity of the interaction and complicated time-dependent transition processes. Many-body interactions further complicate the diffraction processes in a solid. Therefore, many approximations have been made to study these diffractions. On the other hand, optical gratings, most of which can be regarded as one-dimensional(1D) photonic crystals, have been studied for decades. Some phenomena similar to the superprism effect have been experimentally found in 1D and 2D(was called doubly gratings) gratings. Preliminary explanation of the beam directions was proposed [60, 61]. However, the study of transmission intensity was inadequate, not mentioning the study of other aspects. A number of rigorous diffraction theories have been developed, mostly for 1D gratings. Unfortunately, as we shall see, there are still two unsolved issues with popular grating theories that prevent them being applied to two-dimensional(2D) or three-dimensional (3D) photonic crystals.

4.1.1 Interference effect in a photonic crystal slab

In most prior transmission theories for photonic crystals, the problem is formulated as calculating the transmission and reflection coefficients, T and R, for a plane-parallel slab, rather than for each surface. These calculations always include the effect of multiple reflections within the slab. The transmitted and reflected waves are a superposition of all internal reflection orders. Therefore, the overall coefficients R and T for the slab are infinite sums of the products of single-interface transmission and reflection coefficients r and t

$$R,\ T \sim \sum_n c_n r^n t^{(n+j)}. \tag{4.1}$$

In the above relation, c_n is a coefficient that contains the information of optical phase change when light travels between two surfaces, and j is an integer constant. This is adequate for the case of a wide incident beam and a thin slab, where the secondary beams generated by multiple reflections in the photonic crystal have significant overlaps in space, particularly on the exit surface of the slab, as shown in Fig. 4.2 (a). However, this is not adequate for the case where the beam width is relatively narrow, the refraction angle is large, and the slab is relatively thick. After one round-trip reflection, the secondary beam may not overlap with the direct-through beam, as illustrated in Fig. 4.2 (b). Therefore, one has to know the single-interface transmission and reflection amplitudes to compute each exiting beam. A more complicated case is illustrated in Fig. 4.2 (c), where a number of single-interface refraction problems must be solved sequentially to obtain the final exiting beam. The knowledge of r, t for single-interface refractions will be crucial to optimize device performance in many other cases. For instance, the solutions to the single interface refractions are needed to explore the proposed WDM demultiplexers with non-parallel front and back surfaces [42]. Note that once we know single-surface coefficients r and t, we can, in principle, calculate the ideal thin slab transmission problem through infinite sums in Eq. (4.1). Solving the single-interface refraction problem gives us more freedom to deal with non-parallel surface geometries, and any times of internal reflections.

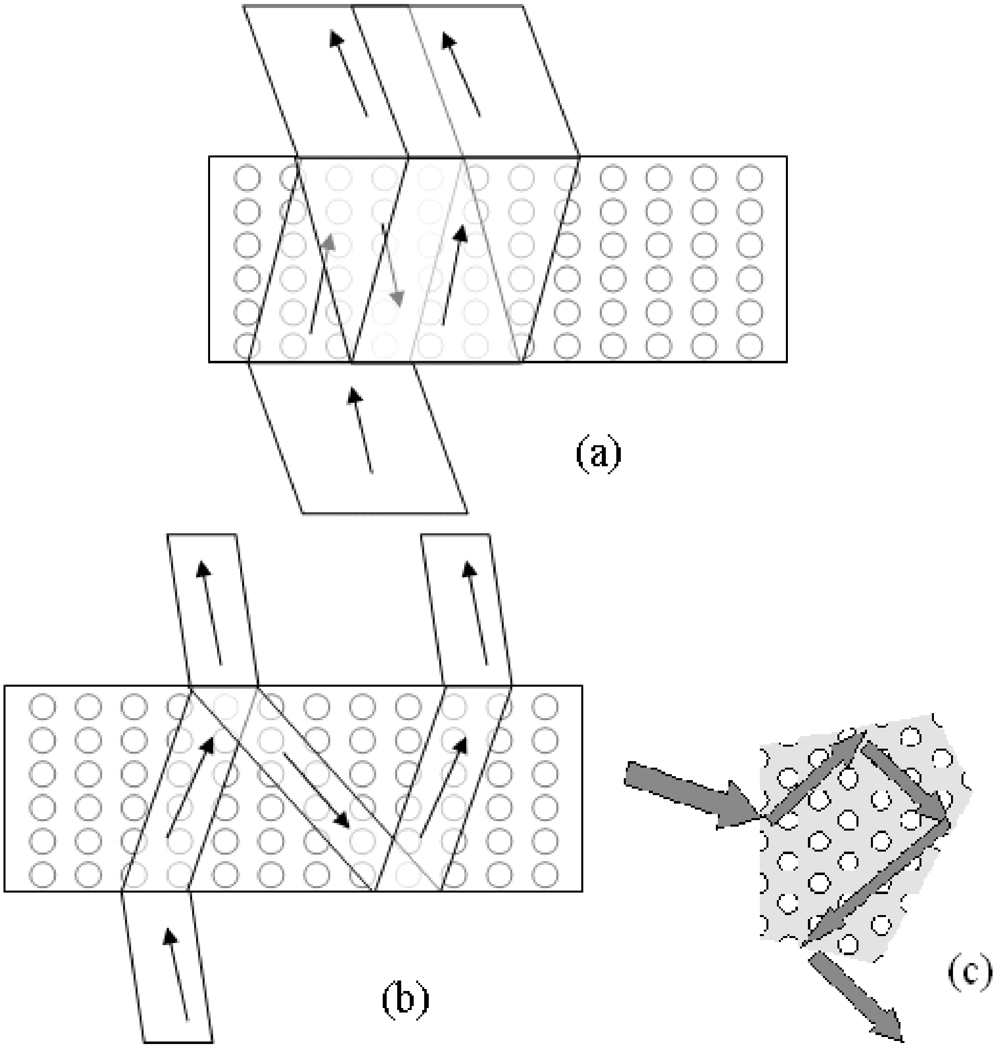

Figure 4.2: Interference effect in a photonic crystal slab. (a) Case of wide beam and small refraction angles: Beams inside photonic crystal (and exiting beams) overlap significantly in space after a round-trip internal reflection inside a photonic crystal slab. A negative refraction case is presented, although the overlap and separation of beam appear regardless of negative refraction. For simplicity, only one round-trip internal reflection is drawn. (b) Case of narrow beam and large refraction angles. Beams separate after one-round trip reflection. The single-interface refraction problem must be solved to obtain the intensity each of exiting beam. (c) Multiple internal reflections for non-parallel surfaces. Our theory can address all three cases. Conventional theory can only address case (a).

4.1.2 Summary of my prior work

I began to pay attention to the single surface coupling problem more than four years ago. It started with an attempt to develop a rigorous analytic theory for photonic crystal waveguides. I soon realized that the prerequisite for the waveguide theory is a rigorous theory for light coupling at a surface of a photonic crystal. When such a theory is available, it can be applied to left and right walls of a 2D photonic crystal waveguides, from which one could further analytically calculate the waveguide modes.

In my Master's thesis, I simplified the problem and showed some good results with an approximate theory. I studied 2D photonic crystal waveguides solely. First, I presumed that the 2D photonic crystals have a complete bandgap. Second, I assumed that for frequencies inside the bandgap, the decaying modes inside the photonic crystal can be derived from the Bloch modes in other frequencies by replacing the real wave vector $\mathbf{k}$ with some complex or imaginary wavevectors α. I managed to calculate the imaginary wavevectors approximately from the Maxwell's equations. The final results were so good for certain cases that it surprised me. I could predict the propagation constant with less than 7% error for a given frequency ω when the photonic crystal parameters were not far from the optimized values(corresponds to largest bandgap). In light of the rigorous refraction theory developed in my doctoral study, of course, that approximate waveguide theory was inadequate. As we shall see, whether the frequency is inside or outside the bandgap, the surface coupling always involves numerous decaying modes, few of which may be obvious derivatives(or vestiges) of some Bloch modes. However, in some cases, it is possible that one decaying mode that is derived from a Bloch mode dominates over all other decaying modes, which explains the good outcome of my prior theory in certain cases.

Arrangement of this chapter

In this chapter, I will give a general, rigorous PC refraction theory that can deal with arbitrary lattice type, arbitrary surface orientation, and arbitrary surface termination. Two key issues, the partition of the forward and backward modes, and the surface-dependent mode degeneracy will be discussed in detail. While most researchers are used to considering solid state physics problems in the reduced Brillouin zone(BZ) scheme, the *periodic BZ scheme* [62] will be demonstrated to be indispensable to understanding the refraction on a PC surface. The natural emergence of a quasi-periodic surface will be discussed, and its relation to surface-dependent mode degeneracy will be uncovered.

This chapter will use some elementary knowledge of some apparently fancy concepts, such as quasi-periodicity and topology. I have made a thorough effort to present these materials in a way that, I hope, is accessible to most photonics researchers. In most cases, this is achieved by avoiding explicit long mathematics and resorting to intuitive arguments.

Some practical and/or more detailed issues will be left for the next chapter.

4.2 Refraction at a surface of a photonic crystal

4.2.1 Master equation and its matrix form

Consider a TM wave(E normal to the plane) incident upon a 2D PC as illustrated in Fig. 4.3. The incident light is a planar wave $e^{i\mathbf{q}_0\mathbf{x}}$ with frequency ω. By Fourier expansion, the field equation in PC is(let the speed of light $c = 1$)

$$-[(k_x + G_x)^2 + (k_y + G_y)^2]E(\mathbf{G}) + \omega^2 \sum_{\mathbf{G}'} \epsilon(\mathbf{G} - \mathbf{G}')E(\mathbf{G}') = 0, \tag{4.2}$$

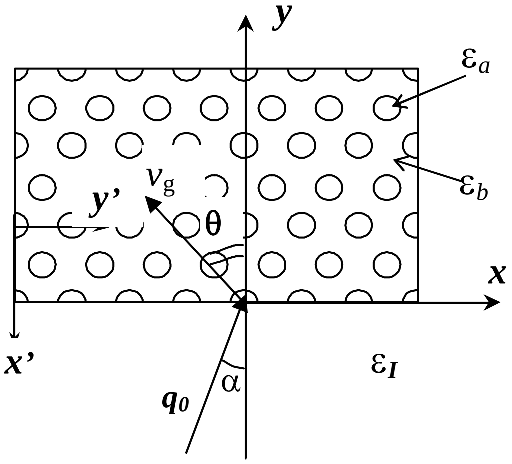

Figure 4.3: A planar wave illuminates a PC surface. The dielectric constant of the incident medium is ϵ_I. For the PC, the background medium has a dielectric constant ϵ_b, while the materials inside the columns have a dielectric constant ϵ_a. Each surface has its own local coordinate system for refractions through a series of surfaces.

where $k_x \equiv q_{0x}$, and $E(\mathbf{G})$ and $\epsilon(\mathbf{G})$ are the Fourier coefficients of $E(\mathbf{x})$ and PC dielectric function $\epsilon(\mathbf{x})$, respectively; $\mathbf{G}$ is a reciprocal lattice vector, explicitly

$$\mathbf{G}_{lm} = l\mathbf{b}_1 + m\mathbf{b}_2,$$

where $\mathbf{b}_1$ and $\mathbf{b}_2$ are the basis vectors of the reciprocal lattice.

This set of linear equations for $E(\mathbf{G})$ can be converted into a matrix equation

$$[W][E] = 0.$$

The elements of column vector $[E]$ are

$$E(\mathbf{G}_{lm}), \qquad -L \leq l \leq L, \quad -M \leq m \leq M,$$

Let

$$N = (2L+1)(2M+1).$$

Clearly,$[W]$ is an $N \times N$ matrix and $[E]$ is an $N \times 1$ matrix. It is straightforward to show that

$$[W] = k_y^2[A] + k_y[B] + [C],$$

where $[A]$, $[B]$, and $[C]$ are matrices. There is a general numerical scheme for such an eigenvalue problem [63, 64]. However, for this particular problem, $[B]$ and $[C]$ depend on k_x and ω in a specific way.

Note that the solution of Eq. (4.2) must satisfy $det[W] = 0$. One readily proves the determinant can be written as a real-coefficient polynomial

$$det[W] = F(k_x, k_y, \omega) = \sum_{lmn} c_{lmn} k_x^l k_y^m \omega^n,$$

where the degree of each variable is $2N$ or less. To prove this, first we notice from Eq. (4.2) that each element of $[W]$ is a polynomial of k_x, k_y, and ω. Note that a determinant is a sum of products of matrix elements, therefore the determinant of $[W]$ is a polynomial of k_x, k_y, and ω as well,

$$det[W] = F(k_x, k_y, \omega) = \sum_{lmn} c_{lmn} k_x^l k_y^m \omega^n.$$

Furthermore, consider the identity

$$det[W] \equiv \left[det[W] + det([W]^T) \right] / 2,$$

where T stands for transpose. Because $\epsilon(\mathbf{G})$ is Hermitian, one can readily show that all c_{lmn}'s must be real. Note k_x^2 and k_y^2 appear on every diagonal element of $[W]$, and ω^2 appears in every element, one can show that in general their highest powers are all $2N$.

In principle, the eigenvalue problem amounts to solving $det[W] = 0$ for $2N$ roots $k_y(s)$, $s = 1, 2, ..., 2N$, for given ω and k_x. Then each $k_y(s)$ is substituted back into $[W]$ to find the corresponding eigenvector $[E_s]$. We note that each mode $E_s(\mathbf{x})$ satisfies the real space wave equation everywhere inside the PC in Fig. 4.3 despite the presence of a surface.

4.2.2 Different perspectives of equation $F(k_x, k_y, \omega) = 0$ and periodic Brillouin zone scheme

It is interesting to remark on some properties of $F(k_x, k_y, \omega) = 0$. When considered from different perspectives, the equation $F(k_x, k_y, \omega) = 0$ gives different meaning. For a given wavevector $\mathbf{k} = k_x\mathbf{e}_x + k_y\mathbf{e}_y$, the equation can be solved for ω to obtained the Bloch modes. The function $\omega(k_x, k_y)$ gives the common band curves we are familiar with in solid state physics. And, as we all know, we only need to compute the value of $\omega(k_x, k_y)$ for k_x and k_y inside the first Brillouin Zone(BZ) because the function repeats itself outside 1st BZ

$$\omega(k_x + G_x, k_y + G_y) = \omega(k_x, k_y). \tag{4.3}$$

where G_x and G_y are the components of an arbitrary reciprocal lattice vector $\mathbf{G}$.

On the other hand, if k_x and ω are given as independent variables, one tries to solve for $k_y(k_x, \omega)$ as a function of k_x and ω, it is a completely different story. Some, or all of the solved k_y roots can be complex. The real k_y roots have the exact correspondence with the ordinary Bloch case, but the complex k_y roots correspond to decaying or evanescent waves that would never show up in the Bloch wave calculation. More importantly, the periodicity in Eq. (4.3) does not transfer in a straightforward manner to this case. First, the complex k_y's don't appear in the previous case, they are not necessarily governed the by the periodicity described by Eq. 4.3). Second, for the real k_y's, one may be tempted to assume that $k_y(k_x, \omega)$ and $k_y(k_x+G_x, \omega)$ are the same, which means that the diffraction effect is equivalent if you change your incident wavevector x-component q_x from k_x to $k_x + G_x$. This is clearly wrong: when G_x is large enough, the incident wavevector y-component $q_y = \sqrt{\omega^2 - q_x^2}$ in the case of $q_x = k_x + G_x$ will be imaginary, which means the incident wave is evanescent. Third, the last hope would be that the periodicity of k_y remain untouched, that is if there is a solution $k_y = k_{y0}$, then $k_{y0} + G_y$ must also be a solution. Unfortunately, this is not always true, either, as we shall see. The discussions on this perspective of $F(k_x, k_y, \omega) = 0$ lie in the heart of the paradigm of solid state physics. To the best of our knowledge, this perspective has not been examined in a way that is presented in the following sections. One reason that this remains unexplored is probably that the interactions in solids are so complicated that this pure effect can never be studied accurately. On the other hand, photonic crystals provide an ideal environment to study this problem owing to the simple, linear nature of Maxwell's equations.

A third perspective comes when we fix the frequency and consider the contours on the k_x, k_y plane described by $F(k_x, k_y, \omega_0) = 0$ at certain frequency ω_0. One immediately recognizes that this gives the dispersion surface (or equi-frequency surface) at ω_0 in the reciprocal space(or k-space), which is an analogy of Fermi surface for electrons in solids.

4.2.3 Separation of forward and backward propagating modes

Only a subset of the solved PC modes from Eq. (4.2) are allowed in the region $y > 0$. Complex $k_y(s)$ roots always appear in conjugate pairs(because F has real coefficients), they are allowed only if $\mathrm{Im} k_y > 0$. As we will see later, the real $k_y(s)$ must be partitioned into equal number of up propagating modes ("up mode") and down propagating modes ("down mode"), otherwise the boundary equations can not be satisfied. Here "up modes" refer to those modes that have group velocity pointing upward to $+y$ direction, and vice versa. Some authors call them forward and backward propagating modes in certain contexts. A similar partition problem arose in the transfer matrix method, and was solved only if a lattice has mirror symmetry M_y [65, 66]. The problem is not solved for an arbitrary lattice type and an arbitrary surface orientation.

To study this problem, first I derive the expressions of the Poynting vector $\mathbf{S}$ and $\nabla_{\mathbf{k}}\omega$. Define

$$\mathcal{H}(E_s) = [E_s]^{\dagger}[W][E_s].$$

For real eigenvalues, $[W][E_s] = 0$ yields $[E_s]^{\dagger}[W] = 0$. Therefore, I have

$$\frac{\partial}{\partial k_y}\mathcal{H}(E_s) = [E_s]^{\dagger}\frac{\partial[W]}{\partial k_y}[E_s].$$

Similarly, $\frac{\partial\mathcal{H}}{\partial\omega}$ is computed. Then note $\frac{\partial\omega}{\partial k_y}$ can be computed from

$$\frac{\partial\mathcal{H}}{\partial k_y} + \frac{\partial\mathcal{H}}{\partial\omega}\frac{\partial\omega}{\partial k_y} = 0.$$

Similarly, $\frac{\partial\omega}{\partial k_x}$ is computed. Thus one finds

$$\nabla_{\mathbf{k}}\omega = \frac{\epsilon_0}{2\omega\mathcal{E}_{em}(s)}\sum_{\mathbf{G}}(\mathbf{k}_s + \mathbf{G})|E_s(\mathbf{G})|^2, \tag{4.4}$$

where $\mathbf{k}_s = k_x\mathbf{e}_x + k_y(s)\mathbf{e}_y$, and

$$\mathcal{E}_{em}(s) = \frac{\epsilon_0}{2\omega^2}\sum_{\mathbf{G}}(\mathbf{k}_s + \mathbf{G})^2|E_s(\mathbf{G})|^2$$

is always positive for real $\mathbf{k}$ modes. For real $\mathbf{k}_s$ modes, the Poynting vector averaged per cell per period of time is readily computed

$$< \mathbf{S} >_{cell,T} = (1/2\mu_0\omega)\sum_{\mathbf{G}}(\mathbf{k}_s + \mathbf{G})|E_s(\mathbf{G})|^2, \tag{4.5}$$

where μ_0 is the vacuum permeability. Hereafter I omit the average brackets of

$\mathbf{S}$. Our calculation of $\nabla_{\mathbf{k}}\omega$ differs from the calculation by the Hellmann-Feynman theorem [67] as I use $\frac{\partial\mathcal{H}}{\partial\omega} \sim \mathcal{E}_{em}$.

$$\mathbf{S} = \mathcal{E}_{em}\nabla_{\mathbf{k}}\omega, \tag{4.6}$$

in accordance with the Green's function result [66]. Even earlier, Yeh derived this relation in a more general context(for both 2D and 3D) [68]. The result from Hellmann-Feynman theorem is a bit more complicated, and direct correlation between $\mathbf{S}$ and $\nabla_{\mathbf{k}}\omega$ is difficult to be revealed by looking at that result. Note that Botten *et al.* derive Eq. (4.6) through Green's function, but no simple formula as in Eq. (4.4) is given.

Same relation holds for TE wave except

$$\mathbf{S} = (4\omega\epsilon_0)^{-1}\sum_{\mathbf{G},\mathbf{G}'} H_s^*(\mathbf{G})(\frac{1}{\epsilon})_{\mathbf{G}\mathbf{G}'}[2\mathbf{k}_s + \mathbf{G} + \mathbf{G}']H_s(\mathbf{G}').$$

Define the sets of up modes and down modes as

$$\mathcal{M}^+ = \{\text{PC mode}|S_y \geq 0 \text{ or } \text{Im}k_y > 0\},$$
$$\mathcal{M}^- = \{\text{PC mode}|S_y \leq 0 \text{ or } \text{Im}k_y < 0\}.$$

The sign tests of S_y apply to real k_y modes only. Now I prove that half of the real k_y modes have $S_y \geq 0$. Due to the relation between $\mathbf{S}$ and $\nabla_{\mathbf{k}}\omega = v_g\mathbf{n}$ ($\mathbf{n}$ is a dispersion surface normal), it amounts to proving that a constant k_x line always intersects the dispersion surface of a given ω at equal number of positive n_y and negative n_y points.

Consider the equation $F(k_x, k_y, \omega) = 0$ for a given ω. As $L, M \to \infty$, it describes an infinite set of contours, *i.e.* the dispersion surface repeated in all Brillouin zones(BZs), on the (k_x,k_y) plane. Here I temporarily assume that the dispersion surface consists of *closed* curves. According to topology [69] (and intuitively), a straight line must intersect a closed contour even number of times except for a tangent case.

For an arbitrary contour shown in Fig. 4.4(a), establish a *local* polar coordinate system (ρ, ϕ) for the shorter contour segment between a and a'. The components of $\mathbf{k}$ are

$$k_x = \rho \cos\phi + k_{Ox},$$
$$k_y = \rho \sin\phi + k_{Oy}.$$

where k_{Ox} and k_{Oy} are the coordinates of point O. The outward normal is given by

$$\mathbf{n} = \frac{dk_y}{d\phi}\mathbf{e}_x - \frac{dk_x}{d\phi}\mathbf{e}_y, \tag{4.7}$$

note $\mathbf{n}$ need not be a unit vector here. One easily computes

$$n_y = -\frac{d\rho}{d\phi}\cos\phi + \rho\sin\phi.$$

In a regular polar coordinate system $\phi_a = \pi/2$ and $\phi_{a'} = 3\pi/2$, therefore

$$n_{ya} = \rho_a > 0, \qquad n_{ya'} = -\rho_{a'} < 0.$$

It is not difficult to prove that n_{ya} and $n_{ya'}$ always have opposite signs regardless of the choice of the azimuthal direction $\phi = 0$.

For contours that have complicated connectivity(maybe unreal) as in Fig. 4.4(b), the above argument always applies if one associates the neighboring crossings into pairs, for example (cc') and (dd') [an equally correct pairing is (cd') and (c'd)]. Therefore, $n_y > 0$ and $n_y < 0$ always appear in pairs no matter how twisted a contour is. This implies a topological nature.

The case where a constant k_x line is tangent to a contour can be understood "dynamically." As illustrated in Fig. 4.4, when a constant k_x line sweeps from left

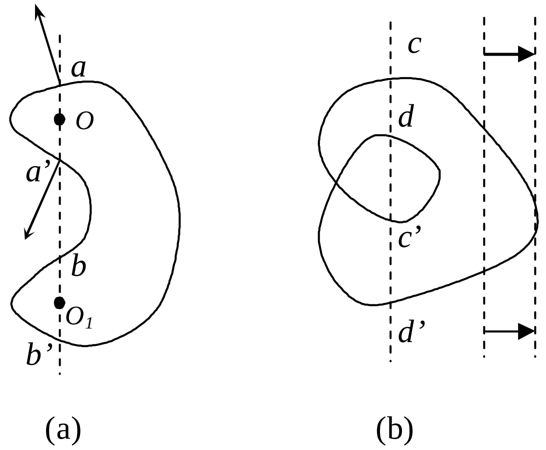

Figure 4.4: Conceptual dispersion surfaces. The vertical lines are constant k_x lines. Note that the contours in (b) may not be realistic. Generally, as the name implies, a contour is closed, and usually never self-intersects.

to right, two intersections with the contours will merge into one when the constant k_x line is tangent to the contour. Mathematically, this means two k_y roots of $F(k_x, k_y, \omega) = 0$ become one doubly degenerate root. These two roots were in $\mathcal{M}^+$ and $\mathcal{M}^-$ respectively before the constant k_x line sweeps to the tangent position, they should remain in their own set at the tangent position. In other words, the doubly degenerate roots should be treated as two roots, one in $\mathcal{M}^+$, and one in $\mathcal{M}^-$.

So far I have neglected open contours(extend to infinity if they exist). A rigorous, yet lengthy, proof can be given for both 2D and 3D PCs, regardless of the presence of open contours. It involves more algebraic topology [69].

4.2.4 Surface orientation, implicit degeneracy, and quasiperiodic surface

Now I find the coupling amplitude t_s for each “up mode". The field in the PC is

$$E(\mathbf{x}) = \sum_{s \in \mathcal{M}^+} \sum_{\mathbf{G}} t_s E_s(\mathbf{G}) e^{i(k_x+G_x)x+i(k_y(s)+G_y)y}.$$

On the surface, such a PC field excites reflected waves $e^{i\mathbf{q}(\mathbf{G})\mathbf{x}}$, where

$$q_x(\mathbf{G}) = q_{0x} + G_x,$$
$$q_y(\mathbf{G}) = -\sqrt{\epsilon_I \omega^2 - q_x(\mathbf{G})}$$

Throughout this section, square roots are taken on the Riemann surface with argument $0 \le \phi < 2\pi$. Note if $G_x = G'_x$, then $\mathbf{q}(\mathbf{G}) = \mathbf{q}(\mathbf{G}')$ even if $G_y \ne G'_y$. Denote the number of reflected waves, *i.e.*, the number of *distinct* $\mathbf{q}(\mathbf{G})$ by $N_{\mathbf{q}}$, one immediately sees that in general, $N_{\mathbf{q}} \le N$. The field in the region $y < 0$ (region I) is then

$$E_I(\mathbf{x}) = e^{i\mathbf{q}_0\mathbf{x}} + \sum_{\mathbf{G}} r_{\mathbf{q}(\mathbf{G})} e^{i\mathbf{q}(\mathbf{G})\mathbf{x}}. \tag{4.8}$$

By matching $E(x,0)$ and $H_x \propto \frac{\partial E(x,0)}{\partial y}$ for each $e^{iq_x(\mathbf{G})x}$ wave, the boundary conditions are given as

$$\delta_{\mathbf{G},0} + r_{\mathbf{q}(\mathbf{G})} = \sum_{s\in\mathcal{M}^+} t_s E_s(\mathbf{G}), \tag{4.9a}$$

$$q_y(\mathbf{G})\left[-\delta_{\mathbf{G},0} + r_{\mathbf{q}(\mathbf{G})}\right] = \sum_{s\in\mathcal{M}^+} t_s [k_y(s) + G_y] E_s(\mathbf{G}) \tag{4.9b}$$

Evidently, the number of $r_{\mathbf{q}(\mathbf{G})}$ is $N_{\mathbf{q}}$, and the number of equations in Eqs. (4.9) is $2N_{\mathbf{q}}$.

Consider a simple example, the (01) surface of a rectangular lattice, *i.e.* $\mathbf{a}_1 = a\mathbf{e}_x$ and $\mathbf{a}_2 = a'\mathbf{e}_y$. The distinct $q_x(\mathbf{G}_{lm}) = q_{0x} + lb_1$ depends on l only, hence $N_{\mathbf{q}} = 2L + 1 < N$. Apparently, the number of up modes equals N. However, due to the periodicity of BZ, all $k_y^{(m)} = k_y + mb_2$, $m = -M, \quad -M+1, ..., \quad M$ are just one "degenerate" solution, as illustrated in Fig. 4.6. Therefore, the number of distinct up modes (and t_s) is

$$N_+ = \frac{N}{2M+1} = 2L + 1.$$

The number of unknowns $\{r_{\mathbf{q}(\mathbf{G})}, t_s\}$ in Eqs. (4.9) matches the number of equations.

In general, because k_x is given(or fixed) in a refraction problem, one easily sees that the degeneracy exists only if the constant k_x line passes multiple points of the periodic set

$$\{\mathbf{k}_s + l\mathbf{b}_1 + m\mathbf{b}_2\},$$

as illustrated in Fig. 4.6(d). I call such a degeneracy "surface-dependent degeneracy." The presence of degeneracy and the degree of it need more analysis if $\mathbf{b}_1$, $\mathbf{b}_2$ are not along x, y axes[see Fig. 4.5(b) and Fig. 4.6(b)]. In general, two cases must be considered.

First, consider the case where the surface of an *arbitrary* lattice has Miller indices (h_1h_2). It turns out the degeneracy also leads to the coincidence $\mathbf{q}(\mathbf{G}) = \mathbf{q}(\mathbf{G}')$ for certain $\mathbf{G}$, $\mathbf{G}'$. Without loss of generality, assume $0 < h_1 < |h_2|$, and h_1 and h_2 are coprime; the basis vectors $\mathbf{a}_1$, $\mathbf{a}_2$ may have *arbitrary* lengths and angles. Define new basis vectors as

$$\begin{aligned} &\mathbf{A}_1 = h_2\mathbf{a}_1 - h_1\mathbf{a}_2, \quad \mathbf{A}_2 = \mathbf{a}_1, \\ &\mathbf{B}_1 = -(1/h_1)\mathbf{b}_2, \qquad \mathbf{B}_2 = \mathbf{b}_1 + (h_2/h_1)\mathbf{b}_2. \end{aligned} \tag{4.10}$$

One can verify $\mathbf{A}_1$ is the surface basis vector(along x), and $\mathbf{B}_2$ is along y axis. Figure 4.5 illustrates a case where $(h_1h_2) = (23)$.

Now start over, expand the E field in the cell spanned by $\mathbf{A}_1$ and $\mathbf{A}_2$ and obtain the new Eq. (4.2) with $\mathbf{G}_{lm} = l\mathbf{B}_1 + m\mathbf{B}_2$, then solve for $k_y(s)$, E_s. For the new $\mathbf{G}_{lm}$, one finds $\mathbf{q}(\mathbf{G}_{lm}) \equiv \mathbf{q}(\mathbf{G}_{l0})$. Let $\mathbf{q}_l = \mathbf{q}(\mathbf{G}_{l0})$, and the distinct reflected waves are $e^{i\mathbf{q}_l\mathbf{x}}$; hence $N_\mathbf{q} = 2L + 1$. Now Eqs. (4.9) become

$$(\delta_{l,0} + r_l) = \sum_{s\in\mathcal{M}^+}\sum_m t_s E_s(\mathbf{G}_{lm}), \tag{4.11a}$$

$$q_{ly}(-\delta_{l,0} + r_l) = \sum_{s\in\mathcal{M}^+}\sum_m t_s \left[k_y(s) + lB_{1y} + mB_2\right] E_s. \tag{4.11b}$$

One readily shows that $k_y(s)$ (real or complex) and $k_y^{(m)} = k_y(s) + mB_2$ lead to

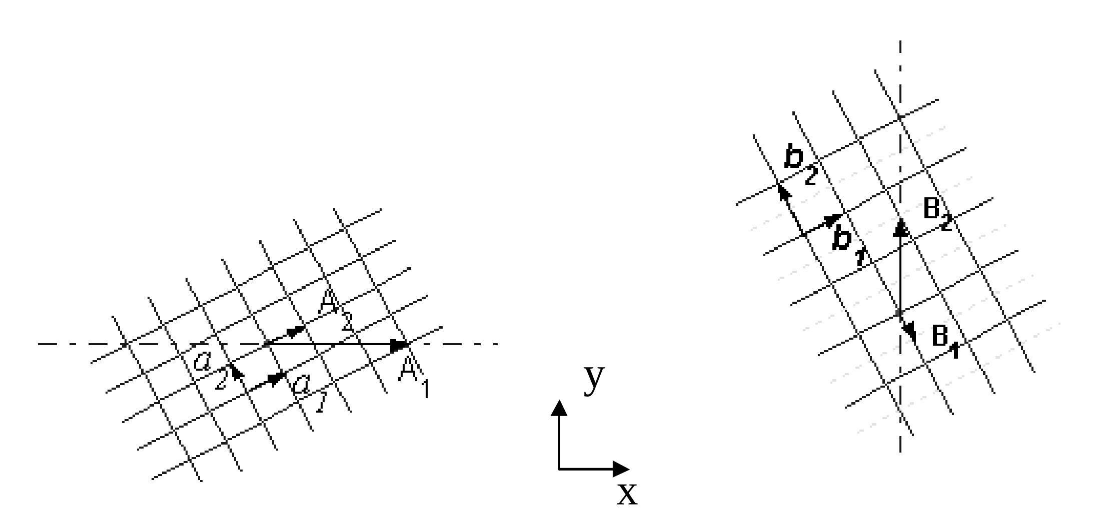

(a) (b)

Figure 4.5: 2D PC lattice with $(h_1 h_2) = (23)$ surface orientation: (a) rotated crystal lattice, (b) rotated reciprocal lattice. The crystal surface is parallel to the x-axis

identical eigenfunctions in real space: $E_s(\mathbf{x}) \equiv E^{(m)}(\mathbf{x})$. [1] Therefore, all of the non-degenerate k_y are in the new one-dimensional(1D) BZ:

$$-B_2/2 \leq \mathrm{Re}k_y < B_2/2;$$

and the number of independent $[E_s]$ (or t_s) is $N_+ = \frac{N}{2M+1} = 2L + 1$. Hence the numbers of equations and unknowns always match for any $(h_1 h_2)$ surface by choosing $\mathbf{B}_1$ and $\mathbf{B}_2$ given in Eqs. (4.10). Second, one can show no degeneracy appears if no two $\mathbf{q}(\mathbf{G})$ (or G_x) coincide. This amounts to the case where h_1/h_2 is an irrational number and the crystal surface is quasi-periodic. [2] In such a case, one needs to

---

[1] Actually, simply rotating the dispersion contours in the reciprocal space, Fig. 4.6(d) is not a faithful drawing of the dispersion contours in the new reciprocal space. According to Eq. 4.10, the unit cell of the reciprocal space must be halved, and there should be a replicated set of dispersion contours that is shifted by $\mathbf{B}_1$ from the set of contours shown. (according to band folding principle [17]) In this way, the density of states in the new unit cell of the reciprocal space is same as the original (2 times larger) unit cell. To avoid the confusion, this is not shown in Fig. 4.6(d).

[2] Quasi-periodicity in 1D refers to a lattice that is characterized by two incommensurate periods, for example, 1 and $\sqrt{2}$. In 2D or 3D, quasi-periodicity means that the lattice has certain order, but

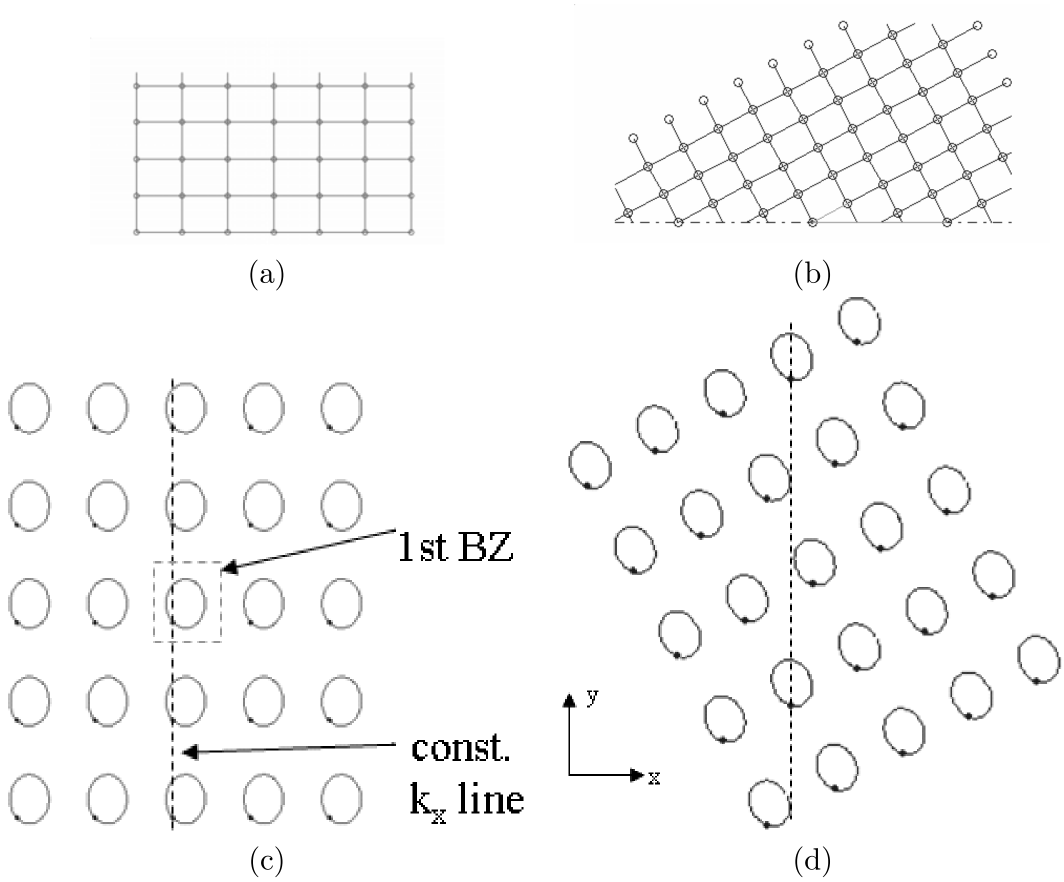

Figure 4.6: Dispersion surface contours for $(h_1h_2) = (10)$ & (23) surface orientation: (a) & (c) crystal lattice, (b) & (d) contours of dispersion surface in the reciprocal lattice. The crystal surface is parallel to the x-axis

solve $2N$ equations in Eqs. (4.9) for $2N$ unknowns. From a higher point of view, the presence of a surface breaks the discrete translational symmetry. This causes the 2D periodicities in the real and reciprocal spaces to be projected onto x and k_y axes, respectively, which may lead to periodic or quasi-periodic 1D sections [70–72].

Remarks

I note that a quasi-periodic surface is rarely achieved in an atomic crystal because an atom can not be divided or "cut" into a fraction. While artificial structures such as photonic crystals can form an ideal flat surface as illustrated in Fig. 4.3, an atomic surface will appear ragged (*i.e.* with lattice voids) even if one intends to cut it into a flat one. For certain surface such as (100) or (111), in principle, one may still have an ideal surface without void if exquisite experiments can be done at a low temperature. But for a general orientation, an atomic surface will be ragged irregularly.

Furthermore, I note that the partition of up/down modes and the surface- dependent degeneracy can both be regarded as classification "filters" that sift the complete set of solved modes of Eq. (4.2) for usage in the boundary condition Eqs. (4.11). These two mode "filters"(or sifter) are independent of each other, and do not interfere each other. Among the complete set of solved modes of Eq. (4.2), there are N up modes and N down modes. For a periodic surface, I have proved that among the N up modes, there are $2L + 1$ unique(or non-degenerate) modes, each having a degree of degeneracy $2M + 1$. However, it is not difficult to see that the foregoing discussion on the surface-dependent degeneracy is equally applicable to the down modes because no part of the proof relies on the direction of the group velocity(which differentiates up modes and down modes). Therefore, the N down modes can be as well reduced to $2L + 1$ unique modes, each of which has a degree of degeneracy

---

the order will be decoded only when considering the lattice as a projection of a higher-dimensional periodic lattice.

$2M+1$. Note that the doubly degeneracy that appears when a constant k_x line is tangent to a contour is of different origin from the surface-dependent degeneracy. The former is a true degeneracy, the latter is of a subtle nature. I sometimes call it implicit degeneracy, as the degenerate modes have apparently distinctive k_y's.

For a quasi-periodic surface, the down modes will not have any surface-dependent degeneracy, either.

4.2.5 Numerical Examples

In Fig. 4.7(a)-(b), I present the result of our theory for an incident-angle sensitive case, compared with the Finite Difference Time Domain(FDTD) simulation results. Hexagonal lattices with air holes($\epsilon_a = 1$) are used in this work, with $\epsilon(\mathbf{G})$ calculated analytically [55]. In most cases, about $N = 120$ planar waves are sufficient to yield an S_y accuracy of 0.3%. The FDTD S_y data are obtained through Eq. (4.5) based on the simulated $E(\mathbf{x}, t)$. The two sets of data agree well. The slight difference comes from FDTD discretization error. A wavelength sensitive case is presented in Fig. 4.7(c)-(d). Only one PC mode is excited here. The FDTD simulations are almost impossible for this case because all phenomena are due to a 2% change of the wavelength λ, while a typical simulation grid spacing is around 2-3% of λ(or the simulation region will be too small). Our theory does not assume a special shape of scatterers, and need not approximate a PC cell by many thin layers. For each incident beam, one essentially solves the field in but one cell per surface. Hence this theory gives a general, efficient, and accurate calculation method.

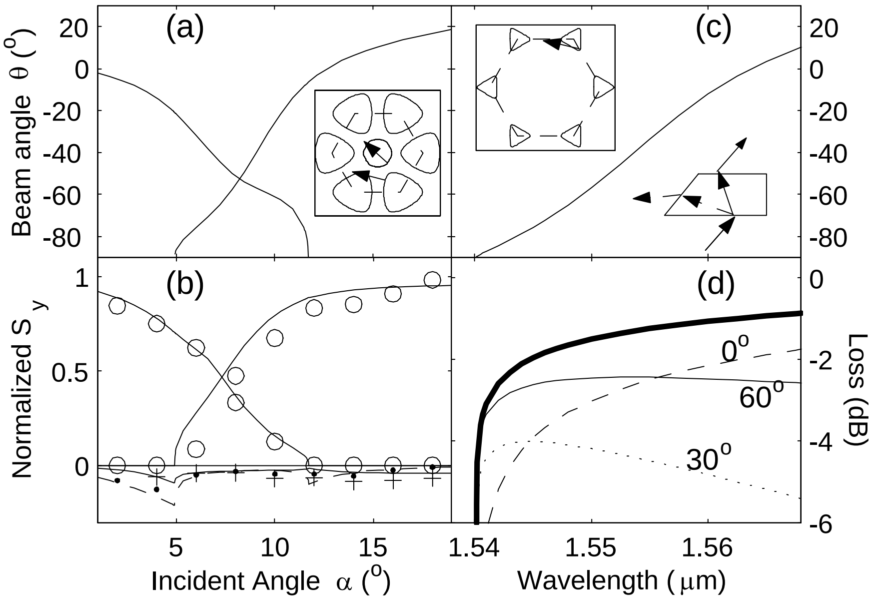

Figure 4.7: Intensities of the refracted and reflected beams calculated by rigorous refraction theory (a) Refraction angles of two PC modes for a structure $\epsilon_b = \epsilon_I = 2.25$, $r/a = 0.3$, and $a/\lambda = 0.677$. Inset shows the dispersion surface with BZ drawn by dashed lines. (b) Same structure as in (a), S_y for PC modes($S_y > 0$) and reflected waves($S_y < 0$). FDTD: markers; Theory: lines. (c) Refraction angle of a PC mode for a structure $\epsilon_b = \epsilon_I = 12$, $r/a = 0.3$, and $a = 0.29\mu m$, $\alpha = 40°$. The inset sketches a demultiplexer design. (d) Insertion losses for the structure in (c). Thick curve: insertion loss after entering PC. Other curves: losses after exiting PC through tilted surfaces.

4.3 Summary and implication of some important results

In summary, an analytic theory is developed for light refraction at a PC surface. For the applications of current interest, I have primarily discussed wavelength or incident-angle sensitive refraction. However, our theory is a general refraction theory that can treat any insensitive case as well. Moreover, the importance of our analysis of the PC surface refraction goes far beyond merely giving amplitudes $\{t_s, r_l\}$. First, incident light recognizes a lattice by its "face." For a square lattice, if the incident surface has Miller indices other than (10) or (01), the light may nevertheless "see" an oblique lattice, according to Eqs. (4.10). This "misinterpretation" completely shuffles the intrinsic mode degeneracy of the original lattice. Secondly, for an *ideal* periodic surface, the coincidence of the wavevectors of different reflection orders, $\mathbf{q}(\mathbf{G}_{lm}) \equiv \mathbf{q}(\mathbf{G}_{l0})$, means the reflected waves only carry the information of the surface periodicity. The surface BZ [17] remains a useful concept. Other Bragg planes inside the PC are hidden. But if a surface is quasi-periodic, the reflected waves carry the information of all Bragg planes. Thirdly, it can be shown that a slight change of surface orientation may split one PC beam into many beams(as obvious in a quasi-periodic case). How to observe such a phenomenon is an interesting question.

Chapter 5

Extension and Applications of the Rigorous Refraction Theory

In the preceding chapter, the refraction of light when a planar wave enters a photonic crystal from a uniform medium was analyzed in detail. In this chapter, the theory will first be extended to the case in which a Bloch wave illuminates an interface from inside a PC, which further allows us to compute the transmissions along a complete light path through a series of interfaces. In addition, the transmission of a Gaussian beam is analytically discussed and the insertion loss formulae are established on a rigorous basis. Other realistic beam profiles are discussed. Lastly, I will discuss the surface termination issue. With all of these issues solved, a complete theoretical framework of photonic crystal refraction and transmission will thus be established. The theory will be applied to design a high channel-count, low-loss WDM demultiplexer.

In addition, the theory will be extended to consider a plane-parallel slab. Rather than explicitly completing the infinite sums in Eq. 4.1 on page 70, I consider the combined boundary conditions at the front and back surfaces. A rigorous and neat theoretical formulation results from this approach. The theory is applied to treat surface relief gratings, whose dielectric functions vary in two dimensions. The gratings are regarded as a 2D PC with but one period in the direction normal to grating surface(this picture is rigorously correct, though a bit uncommon). This approach gives almost perfect agreement with a prior grating theory.

5.1 Light refraction for a Bloch mode exiting a PC

This theory can also calculate the case where a propagating PC mode E_0 with a Bloch vector $\mathbf{k}_0$ is incident upon a boundary from inside a PC(when a beam exits the PC). One readily shows that the boundary conditions must be

$$\begin{aligned} t_l &= \sum_{s\in\mathcal{M}^+}\sum_m r_s E_s(\mathbf{G}_{lm}) + \sum_m E_0(\mathbf{G}_{lm}) \\ q_y t_l &= \sum_{s\in\mathcal{M}^+}\sum_m r_s\left[k_y(s) + lB_{1y} + mB_2\right]E_s(\mathbf{G}_{lm}) + \sum_m (k_{0y} + lB_{1y} + mB_2)E_0(\mathbf{G}_{lm}) \end{aligned}$$

Furthermore, this theory allows us to explore device geometries other than slabs [42, 45], provided that we define local y axes normal to each surface along a light path [as y' in Fig. 4.3(a)] and solve the refraction problems surface by surface. In this way, one essentially solves the field in only a few surface cells to obtain the field in the whole space. Figure 5.1 demonstrates the power of this theory by an extreme case: a vertical exiting surface.

5.2 Refraction of a Gaussian beam

To fully understand Fig. 5.1, one needs to analyze the refraction of a Gaussian beam. The standard technique first decomposes the Gaussian beam into planar wave components, finds the refracted wave for each planar wave, then adds them together to find the total refracted beam [73]. Though not difficult, some calculations are still presented to certain details for clarity and completeness. Consider an incident

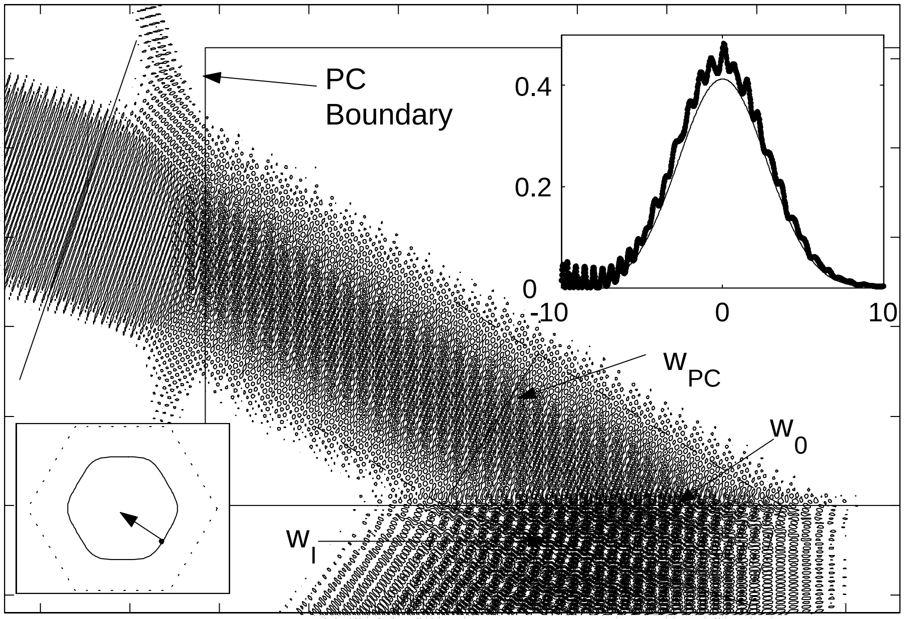

Figure 5.1: Transmission of a Gaussian beam through a PC($\epsilon_b = \epsilon_I = 12$, $r/a = 0.3$). The beam widths w_I, w_{PC}, and w_0 are defined in Eq. (5.9). The observation plane for the exiting beam is indicated by a line. Top inset shows exiting beam profile (FDTD: dense dots; Theory: line). Bottom inset shows dispersion surface.

beam with a distribution in q-space

$$a(\mathbf{q}) = a(\mathbf{q}_0 + \delta\mathbf{q}) = \frac{\sqrt{2\pi}}{\Delta q_\perp}\exp(-\frac{\delta q_\perp^2}{2\Delta q_\perp^2}) \cdot 2\pi\delta(\delta q_\|) \tag{5.1}$$

where $\delta\mathbf{q}$ is decomposed into components $\delta q_\|$ and $\delta q_\perp$, parallel to $\mathbf{q}_0$ and perpendicular to $\mathbf{q}_0$, respectively. Note $\Delta q_\perp$ is a constant indicating lateral spread of $\mathbf{q}$. The incident field is

$$E_{in}(\mathbf{x}) = (2\pi)^{-2}\int a(\mathbf{q})e^{i\mathbf{q}\mathbf{x}}d^2q \tag{5.2}$$

Using the identity,

$$(\sqrt{2\pi}a)^{-1}\int_{-\infty}^{\infty} e^{-\frac{x^2}{2a^2}+ibx}dx = e^{-\frac{1}{2}a^2b^2}$$

the incident field is evaluated

$$E_{in}(\mathbf{x}) = e^{i\mathbf{q}_0\mathbf{x}}e^{-\frac{1}{2}\Delta q_\perp^2 x_\perp^2}. \tag{5.3}$$

The field in PC is $E_{PC}(\mathbf{x}) = \sum_s \widetilde{E}_s(\mathbf{x})$, where

$$\widetilde{E}_s(\mathbf{x}) = (2\pi)^{-2}\int a(\mathbf{q})t_s E_s(\mathbf{x})d^2q \tag{5.4}$$

Note t_s and $E_s(\mathbf{x})$ both depend on the incident wavevector $\mathbf{q}$. If the beam is sufficiently wide, one can evaluate the integral and find

$$\widetilde{E}_s(\mathbf{x}) \approx t_s^{(0)}E_s^{(0)}(\mathbf{x})e^{-(1/2)\Delta k_\perp^2 x_\perp^2}, \tag{5.5}$$

where the term $t_s^{(0)}E_s^{(0)}$ is evaluated at $\mathbf{q}_0$; and $\Delta k_\perp \equiv (\frac{\partial k_\perp}{\partial q_\perp})_\omega \Delta q_\perp$ gives the lateral spread of $\mathbf{k}_s$; $x_\perp$ is the component of $\mathbf{x}$ along $k_\perp$. For simplicity, the mode index s for $k_\perp$ is omitted.

With the chain rule, I have

$$(\frac{\partial k_\perp}{\partial q_\perp})_\omega = (\frac{\partial k_\perp}{\partial k_x})_\omega(\frac{\partial k_x}{\partial q_x})_\omega(\frac{\partial q_x}{\partial q_\perp})_\omega \tag{5.6}$$

By definition of $k_\perp$ and $q_\perp$, one may derive

$$(\frac{\partial k_\perp}{\partial k_x})_\omega = \frac{1}{\cos\theta}$$
$$(\frac{\partial q_x}{\partial q_\perp})_\omega = \cos\alpha$$

Now note $k_x \equiv q_x$, then it is obvious

$$(\frac{\partial k_\perp}{\partial q_\perp})_\omega = \frac{\cos\alpha}{\cos\theta}, \tag{5.7}$$

Define beam width

$$w_I = \sqrt{8}\Delta q_\perp^{-1}, w_{PC} = \sqrt{8}\Delta k_\perp^{-1}. \tag{5.8}$$

Then

$$w_I/\cos\alpha = w_{PC}/\cos\theta = w_0. \tag{5.9}$$

This means the crosssections of the two beams along the boundary have the same width as shown in Fig. 5.1.

Note the reflection smears the true w_I in Fig.5.1. The peak of $\widetilde{E}_s(\mathbf{x})$ remains at the value of the planar incident wave case. The power for a Gaussian PC beam is

$$P = \int S dx_{s\perp} \approx \sqrt{\pi/8}\cdot\overline{S}w_{PC} = \sqrt{\pi/8}w_0(\overline{S}\cos\theta), \tag{5.10}$$

where $\overline{S}$ is the peak value of the Poynting vector. One thus finds the conservation of $S_y = S\cos\theta$ relates to the conservation of total power P as

$$\sum_l R_l + \sum_s T_s = \sum_l \frac{|S_{ly}|}{S_{0y}} + \sum_s \frac{S_{sy}}{S_{0y}} = 1 \tag{5.11}$$

where R_l and T_s are the normalized powers of a reflected beam and a PC mode $\widetilde{E}_s$, respectively; $\mathbf{S}_l$ and $\mathbf{S}_s$ are the corresponding Poynting vectors, and $\mathbf{S}_0$ is the incident Poynting vector. The summations should be limited to the propagating modes. The insertion loss is given by $10log_{10}(T_s)$ for a PC mode. A beam coming from inside a PC can be treated similarly. Figure 5.1 shows the planar wave theory gives the beam peak and width accurately.

5.3 Refraction of an arbitrary beam

For a general beam profile, our theory also provides a convenient way of calculating the refracted and reflected beams. First, the incident beam is decomposed into its planar wave components $a(\mathbf{q})$ in the wave vector space. Then for each incident planar wave component with a distinctive q_x (ω is fixed as a monochromatic beam is considered here), one can calculate the refracted and reflected waves. Because our theory is essentially an analytic theory, only a small number of coefficients contains all the information of the refracted and reflected waves. Specifically, with the following quantities

$$r_l, \quad t_s, \quad E_s(\mathbf{G}_{lm}), \tag{5.12}$$

all other quantities can be derived. Note that the quantities listed in Eq. (5.12) only occupy a negligible amount of computer memory or storage space. The most voluminous data are E_s, which take about N complex double precision data spaces for each solved unique up mode. Note that we only need to record the propagating modes, the number of which seldom exceeds five in each case. Also note that r_l and t_s occupy at most $2N$ complex data space. Therefore, the total data storage required for each incident planar wave is less than $7N$ complex data spaces. For typical $N = 120$ (see Sec. 4.2.5), the data generated for each incident planar wave are about 14KB to 27KB, [1] quite small for today's personal computers. One can easily decompose the incident beam into 100 planar wave components with different q_x; calculate and store the data for each component. Using these data, one can finally integrate to obtain the refracted beam according to Eq. (5.4 on page 93). Only a few Megabytes of data storage is required to store the information of refracted and reflected waves for 100 incident planar wave. The above procedure would be much more costly for other approaches such as layered transfer matrix methods, which require several orders of magnitude larger data storage in addition to probably prohibitive computational time.

Furthermore, the power conservation, Eq. (5.11), can be proved for an arbitrary beam profile based on a more general form of Eq. (5.10). One shall construct in the $x - y$ space a large enough contour that encloses the refraction point on the interface. The contour should cut cross the beam at a place sufficiently far from the refraction point so that all the beams separate from each other when they cross the contour. Then one can compute the following path integral along contour C

$$\int_C S_n ds = 0,$$

where S_n is the surface normal component of the Poynting vector. The integral must varnish because there is no source or absorber inside the contour. By properly flattening the contour segments that cross the beams, one can again prove the conservation equation Eq. (5.11).

---

[1] One double precision complex number occupies 16 Bytes of space, one quadruple precision number occupies 32 Bytes of space

5.4 Arbitrary surface termination

Surface termination is an interesting issue, which was briefly discussed in Ref. [17] for the surface modes with frequencies in the bandgap, and in refraction [49]. For example, for a $(h_1 h_2) = (10)$ surface of a rectangular lattice, the surface modes will be different depending on whether the surface is terminated at the center of a column(or hole), or is terminated midway between two column centers. Figure 5.2(a) and (b) illustrate two different terminations. For the refraction problem, this termination also makes a difference for the transmission and reflection amplitudes and phases. In all preceding calculations, I have assumed the surface exactly terminates at a center of a column.

For the termination illustrated in Fig. 5.2(b), if the coordinate system is established as in Fig. 5.2(d), then apparently, one can follow the procedures described above to calculate the transmission and reflection coefficients. Nothing seems special. However, for many common lattices where the inversion symmetry is present, one would prefer to place the origin at the column centers so that the Fourier transform of the dielectric function $\epsilon(\mathbf{G})$ can be represented by a real-symmetric matrix. This will significantly reduce the computational load and the complexity of the algorithm. I will not explore further in this choice of origin owing to the disadvantage presented above.

When the origin is chosen at the center a column, one may directly write down the following boundary conditions

$$\begin{aligned}
(\delta_{l,0} e^{iq_{0y} y_0} + r_l e^{iq_{ly} y_0}) &= \sum_{s \in \mathcal{M}^+} \sum_m t_s E_s(\mathbf{G}_{lm}) e^{i[k_y(s) + lB_{1y} + mB_2] y_0}, && (5.13\text{a}) \\
q_{ly}(-\delta_{l,0} e^{iq_{0y} y_0} + r_l e^{iq_{ly} y_0}) &= \sum_{s \in \mathcal{M}^+} \sum_m t_s \left[k_y(s) + lB_{1y} + mB_2\right] \\
&\qquad \times E_s(\mathbf{G}_{lm}) e^{i[k_y(s) + lB_{1y} + mB_2] y_0}. && (5.13\text{b})
\end{aligned}$$

However, this would inevitably leads to divergence in most practical cases. The di-

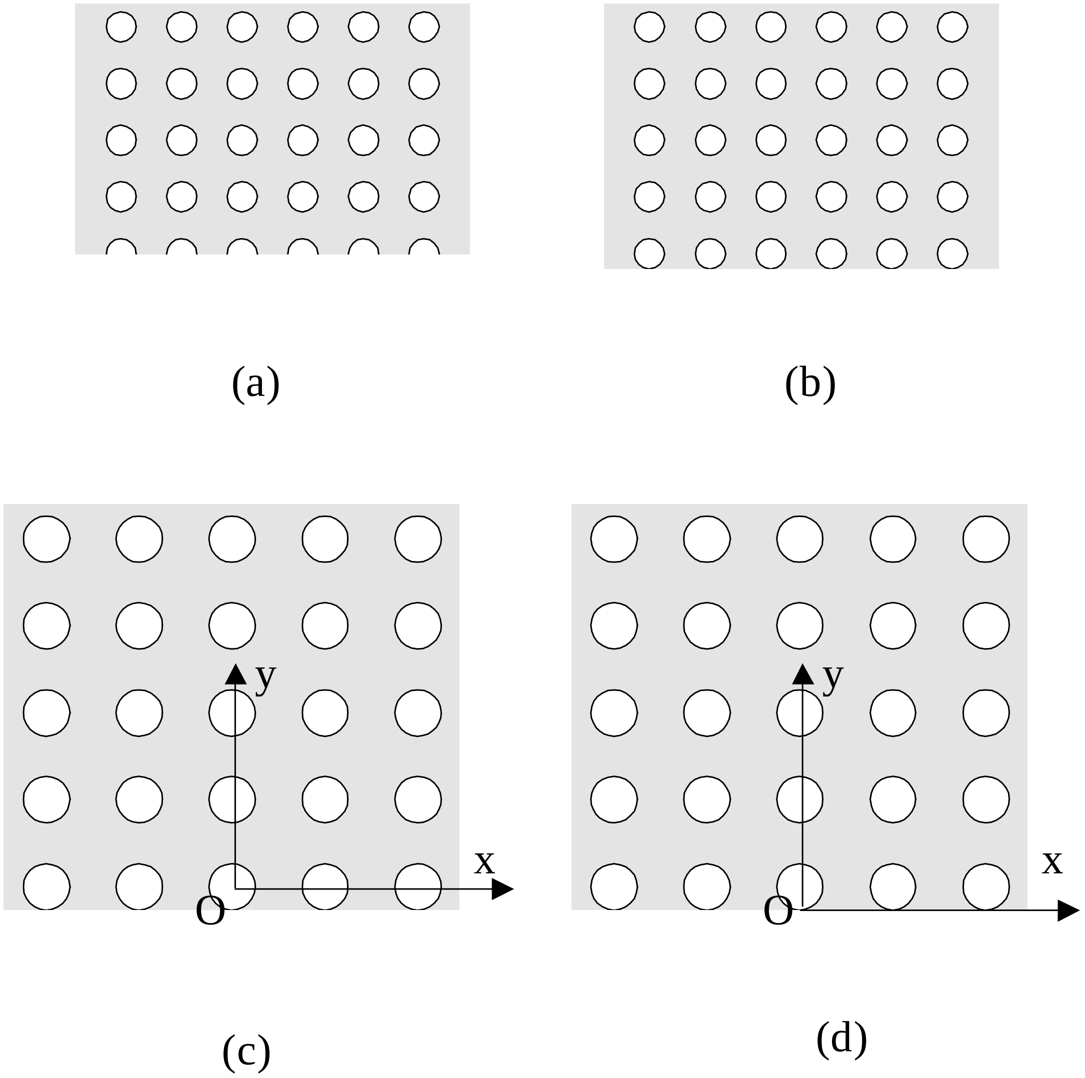

(a) (b)

(c) (d)

Figure 5.2: Surface termination and proper choice of the origin of a coordinate system (a) Crystal terminates at the column centers; (b) Crystal terminates at another position. (c) Good choice of origin; (d) A choice of origin not perferred for symmetry concerns.

vergence comes from the complex $k_y(s)$'s and q_{ly}'s. For the case shown in Fig. 5.2(c), y_0 is negative while the imaginary parts of $k_y(s)$'s are positive. Therefore, the exponential $e^{ik_y(s)y_0}$ factors on the right will be much larger than the corresponding factors for other propagating modes. [2] It can be proved that the larger the L, the larger the maximum $Imk_y(s)$. However, the amplitude, t_s, for such a complex $k_y(s)$ mode is usually extremely small so that, in principle, the contributions of the complex k_y modes to Eq. (5.13) are still much smaller than the propagating modes. Unfortunately, in numerical calculations, such an ideal case is rarely seen. The rounding errors of t_s for the complex k_y modes are magnified by exponential factor $e^{ik_y(s)y_0}$ and the errors dominate over the contribution of the propagating modes. For the case $y_0 > 0$, the exponential factors, $e^{iq_{ly}y_0}$, on the right are extremely large. These large factors amplify round-off errors in each numerical iteration, and result in divergence or produce senseless final numerical outputs. From another point of view, the above set of linear equations have a coefficient matrix whose elements differ in value by several orders of magnitudes. Such a matrix is usually ill-conditioned and an accurate solution is generally impossible.

Fortunately, the structure of that matrix is that each column of the matrix is governed by the same exponential factor. Based on this, a numerical trick is introduced to solve this problem. Define

$$\widetilde{r_l} \equiv r_l e^{iq_{ly}y_0}, \tag{5.14a}$$

$$\widetilde{t_s} \equiv t_s e^{ik_y(s)y_0}. \tag{5.14b}$$

Now the divergent exponential factors disappear from Eqs. (5.13), and the boundary conditions become

---

[2] Another way of understanding this: the complex k_y modes decay as $y \to +\infty$; therefore, they grows when $y \to -\infty$. The largest imaginary part of $k_y(s)$ is related to how many Fourier coefficients(determined by L and M) are chosen.

$$(\delta_{l,0}e^{iq_{0y}y_0} + \widetilde{r}_l) = \sum_{s\in\mathcal{M}^+}\sum_m \widetilde{t}_s E_s(\mathbf{G}_{lm})e^{i[lB_{1y}+mB_2]y_0}, \tag{5.15a}$$

$$q_{ly}(-\delta_{l,0}e^{iq_{0y}y_0} + \widetilde{r}_l) = \sum_{s\in\mathcal{M}^+}\sum_m \widetilde{t}_s\left[k_y(s) + lB_{1y} + mB_2\right]E_s e^{i[lB_{1y}+mB_2]y_0}. \tag{5.15b}$$

Of course, if one needs the original r_l and t_s, one still has to convert $\widetilde{r}_l$ and $\widetilde{t}_s$ according to Eq. (5.14). The conversion is just a simple multiplication(or division) whose round-off error is easily controllable. The prior trouble comes from the fact that when the multiplication with a large exponential is followed by a series of other additions and multiplications with unpredictable nature, the round-off error quickly grows out of control. In practice, I note that most of the quantities needed are actually directly related to $\widetilde{r}_l$ and $\widetilde{t}_s$, rather than the original r_l and t_s. The coefficients $\widetilde{r}_l$ and $\widetilde{t}_s$ are somehow related to the amplitudes on the surface(regardless the choice of origin), while r_l and t_s are somehow related to the amplitudes at the origin O. It seems that the former have more physical meaning than the latter. As expected, the refraction intensities are periodic as y_0 varies, with a periodicity of a' for a rectangular lattice.

In the foregoing discussions, I have assumed that the surface is periodic. When the surface is quasi-periodic, the same principle applies: for a lattice with inversion symmetry, always choose the origin at the inversion center, and use $\widetilde{r}_l$ and $\widetilde{t}_s$ rather than r_l and t_s.

If the origin is chosen as in Fig. 5.2(d), one may avoid the divergence trouble for a single-surface problem However, to study the slab problem (in a later section), where at least one of the surface does not pass the origin, this trick plays an essential role.

5.5 Application of the theory

5.5.1 Design of a WDM demultiplexer

Following the example in Fig. 4.7(c)-(d) on page 88, I calculate the insertion losses for a demultiplexer assuming the exiting surface has an angle of 0°, 30°, or 60° with the entering surface. Generally, I find the *total* transmission will be enhanced if the exiting surface is perpendicular to the beam in PC. The 30° case seems to be an exception because there is another exiting beam(not plotted) of comparable strength. The loss spectra in Fig. 4.7(d) suggest that for $\theta < -34^\circ$, one should use a 60° exiting surface. The corresponding demultiplexer design is sketched in Fig. 4.7(c) inset and Fig. 5.3(b). This design demonstrates lower than 3dB loss over a 25 nm wavelength span, covering >60 WDM channels if 0.4 nm resolution is possible [42]. Further optimization and other details of this device will be presented elsewhere. For a finite PC, applying the single-surface refraction method assumes the crystal is sufficiently large and the concept of beam is valid. This is practically the case in many PC devices [14, 40].

5.5.2 Transmission through a photonic crystal slab or a volume grating

In fact, this theory can be extended to treat the transmission through a thin photonic crystal slab as well without using the infinite sums in Eq. (4.1). To this end, I write down the combined boundary conditions for a slab whose front and back surfaces are located at y_0 and y_1, respectively,

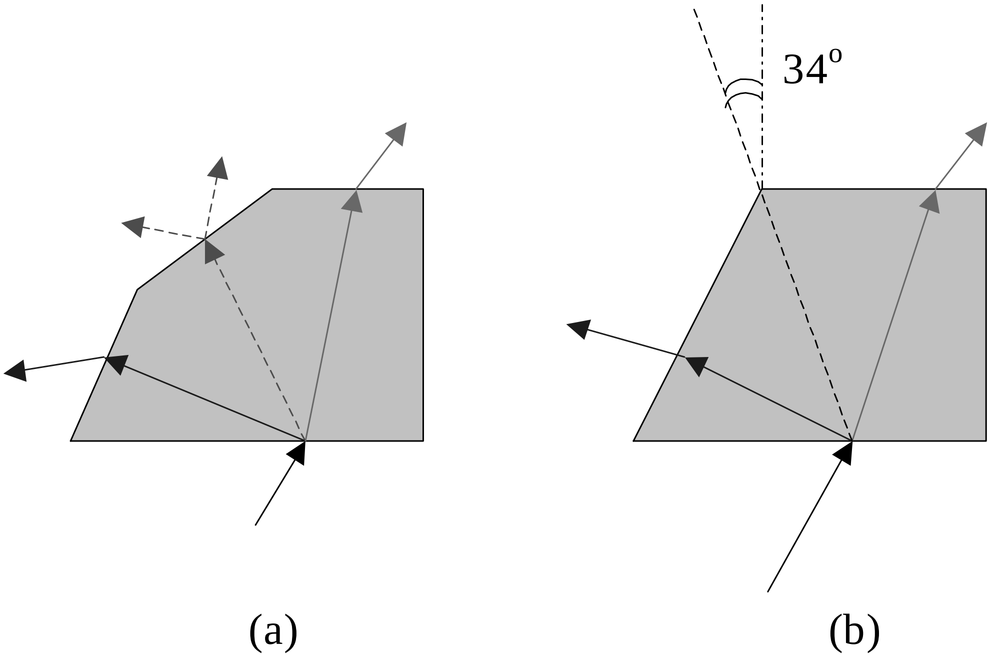

Figure 5.3: Schematics of PC based high channel-count, low-loss demultiplexers: (a)An inferior design where two beams exit PC on the 30^o surface. This increases loss by 3dB. (b) A good design, the losses of all channels are below 3dB. On a 100-GHz grid, this demultiplexer can accommodate about 32 channels.

$$(\delta_{l,0}e^{iq_{0y}y_0}+\widetilde{r}_l)=\sum_s\sum_m\widetilde{f}_sE_s(\mathbf{G}_{lm})e^{i[lB_{1y}+mB_2]y_0}, \tag{5.16a}$$

$$q_{ly}(-\delta_{l,0}e^{iq_{0y}y_0}+\widetilde{r}_l)=\sum_s\sum_m\widetilde{f}_s\left[k_y(s)+lB_{1y}+mB_2\right]E_se^{i[lB_{1y}+mB_2]y_0}, \tag{5.16b}$$

$$\widetilde{t}_l=\sum_s\sum_m\widetilde{f}_se^{ik_y(s)(y_1-y_0)}E_s(\mathbf{G}_{lm})e^{i[lB_{1y}+mB_2]y_1}, \tag{5.16c}$$

$$-q_{ly}\widetilde{t}_l=\sum_s\sum_m\widetilde{f}_se^{ik_y(s)(y_1-y_0)}\left[k_y(s)+lB_{1y}+mB_2\right] \times E_se^{i[lB_{1y}+mB_2]y_1}, \tag{5.16d}$$

The coefficients $\widetilde{r}_l$ and $\widetilde{t}_l$ are the (renormalized) reflection and transmission amplitudes, and $\widetilde{f}_s$'s are the amplitudes of the unique PC modes. Note that due to the internal reflections at the back surface, both up modes and down modes must be included in the calculation. The slab is assumed to be immersed in one medium. The equation should be slightly modified if the medium in front of the slab is different from the one in the back.

In the following, I will apply this slab formulation to calculate the diffraction by a volume grating. Actually, a 1D grating can be regarded as a photonic crystal which only has one period in the y direction. Based on this, I calculate the transmissions and reflections by a surface relief grating and compare with a classic paper [74] in Fig. 5.4. The agreement is almost perfect.

I note that the layered transfer matrix formulation, which has been one of the most popular methods for studying grating diffraction, has a much more complicated and error-prone numerical scheme compared to this theory. First, the grating (or one cell of the photonic crystal slab) must be sliced into many thin layers. Then, the grating theory calculates the transfer matrix of each layer and multiples all the transfer matrices to obtain the transfer matrices of the slab. Furthermore, to avoid some divergence issues, modified matrices, which are called scattering matrices in one approach, must be used for each thin layer. Typically, calculating such modified matrices requires matrix inversion. The matrix multiplication and inversion

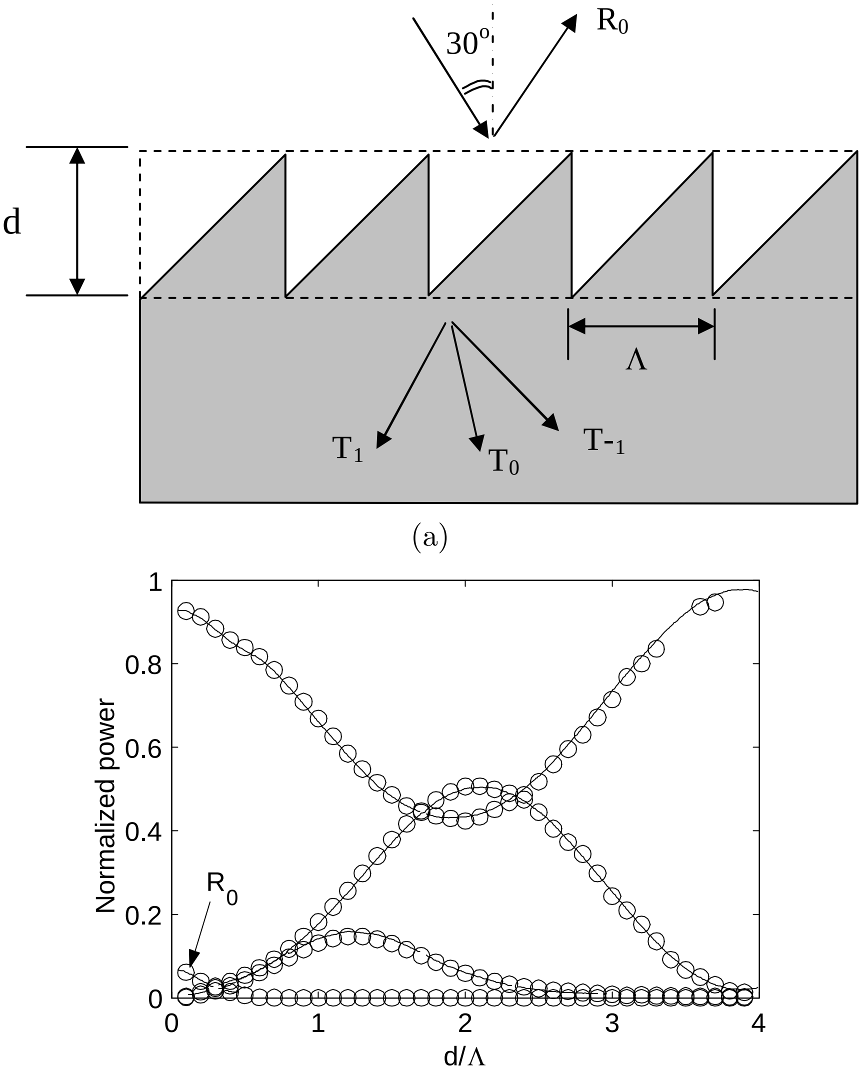

(a)

(b)

Figure 5.4: Comparision with conventional grating theory for an inverse sawtooth surface relief grating calculated by Moharam & Gaylord in Ref. [75] Fig. 8. (a) The geometry of the system. (b) Normalized powers for various transmission and reflection orders. Here R_0 indicates the zeroth order reflection, T_0, T_1, and T_{-1} denote corresponding orders of transmissions as indicated in (a). (other orders vanishes for this case), other curves are all transmission powers. The sawtooth depth is d and its period is Λ.

steps usually bring significant complexity to the numerical calculations. When a series of matrix multiplication and inversion steps are involved, the error analysis of the overall numerical scheme becomes so complex that one has to rely on empirical knowledge to estimate the error. Actually, it took over a decade for grating theoreticians to pin down the key sources of error in the transfer matrix formulation (see the introduction paragraphs of Ref. [65] and references therein).

In contrast, the theory developed here only needs to solve one eigenvalue for a single matrix, plus solving one set of linear equations. The procedure is much simpler, and the numerical error is much more controllable. There are many standard methods to rigorously estimate the error bounds of the single-matrix problems in this case.

Note that the transfer matrix formulation has been frequently used in calculating transmission through a photonic crystal slab recently. The theory presented here is certainly a better candidate for both grating and PC slab transmission calculations.

5.6 Summary and future work

A rigorous theory has been developed for light refraction by a photonic crystal with arbitrary lattice type, surface orientation and termination. The forms of incident wave addressed by this theory include planar incident waves, Gaussian beams, and arbitrary beam profiles. The theory has successfully solved the problem of partitioning forward and backward propagating modes. The periodic Brillouin zone scheme is demonstrated to be the key to understanding the refraction phenomena. Surface-orientation dependent mode degeneracy is discovered, and its relationship to quasi-periodic surfaces is unfolded. A slight change of surface orientation is predicted to split one beam into infinite number of beams in certain cases.

This theory offers a new picture of the refraction processes and opens the door to a broad range of problems that required prohibitive computation resources based on prior methods. In addition, there are numerous new theoretical problems unveiled by this theory.

First, this theory will lead to an analytic guided mode theory for photonic crystal waveguides. To the best of my knowledge, all current PC waveguide theories are imperfect in that they all use a finite spatial region (usually bounded by absorbing layers) to simulate a photonic crystal waveguides. A true analytic mode theory seeks a mode profile formula valid in the whole space. There is no need for artificial absorbing layers at the boundaries. Actually, an analytic theory for 2D photonic crystal waveguides can be readily developed by slightly modifying the slab transmission theory. Note a PC waveguides is actually a slab of uniform medium is sandwiched between two semi-infinite photonic crystal walls. In some sense it is the reverse of a PC slab, where a photonic crystal is sandwiched between two semi-infinite uniform media. The boundary conditions further differ in that the slab transmission problem is related to a matrix equation of the form

$$Ax = b,$$

while the calculations of guided modes involve

$$Ax = 0,$$

where A is a matrix whose elements depend on ω and $\mathbf{k}$, and $det(A) = 0$ gives the dispersion relation of the waveguide modes.

As discussed earlier, light coupling through an endface into a PC waveguide, which is essentially a single-surface transmission problem, can be analyzed with this refraction theory as well. In some aspect, this is a simpler problem, because usually it is assumed that both the incident angle and refraction angle are zero degree. More detailed calculations for various waveguide configurations are needed.

In addition, it would be desirable to develop a perturbation theory that shows how a slight change in surface orientation splits one beam to infinite number of beams. One can easily prove that generally, many of these split beams differ only slightly in the propagation direction, and will be difficult to separate and observe. However, if the original constant k_x line passes an angle-sensitive part on the dispersion contour, then the superprism effect will help disperse the beams and ease the observation of beam splitting. On the other hand, a perturbation theory is desired to accurately predict the intensity of each split beam as the surface orientation budges. It is anticipated that many of the split beams will be of similar strength. However, I feel that there will be much richer phenomena to explore than I can imagine here.

Furthermore, it would be of interest to study an interface between two PCs of incommensurate lattice constants, which may lead to other discoveries. This problem has similarity with the sampled gratings, which have been successfully utilized to make agile, wide tuning-range tunable lasers.

Lastly, negative refraction in photonic crystals have been subject to intensive study recently. The prospect of making superlenses with resolutions beyond the Rayleigh limit [76] has stirred significant interest in the research community. Plane-parallel photonic crystal slabs are one of the primary candidates for superlens applications [43]. The rigorous theory developed in Sec. 4.1.1 for photonic crystal slabs sheds new light on the problem. With this theory, some speculative ideas can now be evaluated on a rigorous basis. Although I will certainly study further in this area, it is also my hope that other researchers will benefit from this theory.

To conclude, I emphasize again the problems addressed in the last two chapters lie in the heart of the paradigm of solid state physics. I hope this work will stimulate further study, and possibly be extended to areas such as surface physics, X-ray and electron diffraction.

Appendix A

Experiments on Light Refraction and Propagation in Photonic Crystals

In this appendix, photonic crystals fabricated on polymer and silicon substrates will be presented and related devices will be discussed.

Polymeric materials can be coated on almost any substrate of interest, lending themselves to a broad ranges of applications. Particularly, polymeric materials have been widely used to form integrated optical waveguides for fiber-optic communications applications [78].

Polymer photonic crystals have been studied recently [79–87]. One key issue that deters the wide spread usage of polymer photonic crystals has been the low index contrast in polymer photonic crystals. The typical index contrast between polymers and air is about 1.5:1, too small to produce a full bandgap for a 2D photonic crystal. However, it was proposed that by employing high index nanoparticle additives, the polymer refractive index could increased [83].

In reality, the 2D photonic crystals are often considered in a slab geometry, which utilizes photonic bandgap to confine light in the plane of the slab, while employing large index contrast to guide in the vertical(out-of-plane) direction [88–94].

A.1 Fabrication of photonic crystal

A.1.1 Integration of photonic crystal nanostructures with conventional channel waveguides on a polymer platform

We used Hitachi OPI-N3000 series polymers in our fabrication. Typically, polymer N3205 is used for cladding and N3305 is used for core. The fabrication procedure is as follows. First a layer of N3205 is spun on a clean silicon wafer as the bottom cladding, followed by spinning the core layer N3305. Then a thin layer of aluminum(Al) is deposited on the polymer in the CHA Electron Beam Deposition Chamber. Now the photoresist AZ5209 is applied, and the waveguide pattern is transferred from a mask onto the photoresist by Karl Suss Photolithography Aligner. The mask patterns are further transferred onto the Al layer by wet etching. Then the polymer is dry-etched in the Oxford Instrument Plasmalab 80plus Reactive Ion Etching(RIE) System. The remnant Al is stripped from the top surface after RIE, and a layer of polymer is applied on the top as the top cladding. At this point, the waveguide structures are fully fabricated. Now deposit a layer of Al about 60 nm thick, and apply the e-beam resist polymethyl methacrylate (PMMA). The photonic crystal pattern is directly written on the PMMA with the Raith 50 Electron Beam Nanolithography Facility. The pattern is transferred onto the underlying Al layer by wet etching such that a regular lattice of holes appear on the Al. After removing the remnant PMMA, the wafer is sent into the RIE chamber, and we use oxygen as the etching gas. To obtain hole depth between 5 μm to 8 μm, the etching time is between 1.5 hour to 4 hours. Time may vary depending on the pressure and other parameters. The

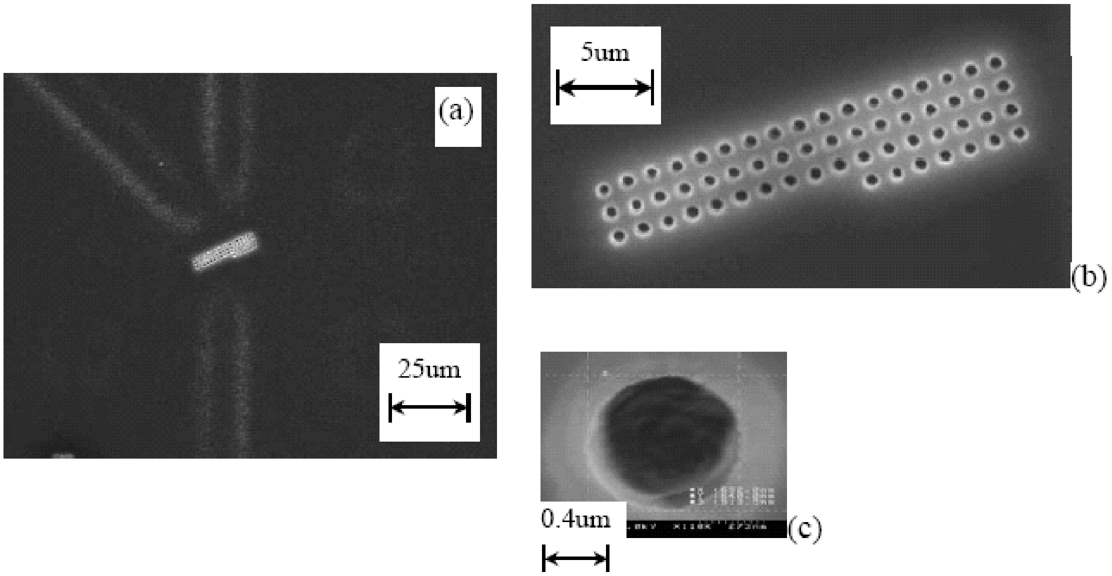

Figure A.1: SEM pictures of polymer photonic crystals

holes of photonic crystal are separated at about 1.3 μm, the hole diameters are 0.9 μm. The holes are etched through the top cladding and penetrate the core layer. By careful design and fabrication, we can create a three-dimensional three-layer polymer structure in which certain part of the top layer(top cladding) is very thin. Then when we fabricate photonic crystal, the eight micron deep holes actually penetrate to the bottom layer (bottom cladding). Thus the photonic crystal effectively covers the whole middle layer(core) where the optical functions take place. The images of the photonic crystals shown in Fig. A.1 were taken by an Hitachi S-4500 Field Emission Scanning Electron Microscope.

A.1.2 Silicon photonic crystals

In recent years, silicon photonic crystals have been extensively investigated. One of the enabling factor is the availability of relatively inexpensive silicon-on-insulator(SOI) wafers. With commercially available SOI wafers that have high quality, silicon pho-

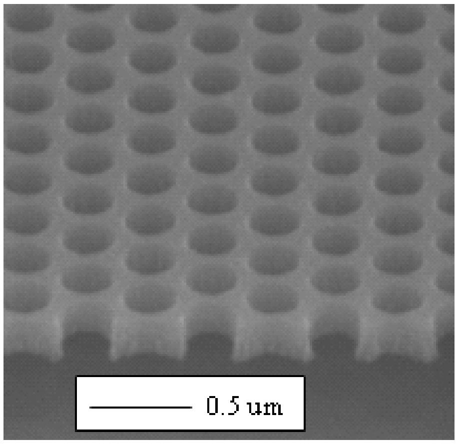

Figure A.2: SEM picture of a silicon photonic crystal that has a 2D hexagonal lattice. The lattice constant is about 340nm. And the hole diameter is about 190nm. The silicon layer is about 0.24 μm thick.

tonic crystal nano-structures, particularly silicon photonic crystal slab and silicon photonic crystal waveguides can be easily fabricated.

Silicon photonic crystal nano-structures have recently been fabricated by the colleagues in our research group. The fabrication processes start with the growth of an oxide layer on an SOI wafer, following by coating the ebeam resist. Then the resist will be patterned by electron beam nanolithography with subsequent development. The pattern will be transferred to the underlying oxide layer by reactive ion etching(RIE), and the ebeam resist will be removed. An ensuing RIE process will finally etch the photonic crystal nano-structures on the SOI layer, using the patterned oxide layer as a hard mask. The remaining oxide on the top of the silicon will be etched away in certain cases, although leaving the oxide layer would not severely affect the properties of the photonic crystal waveguides as the oxide layer is usually very thin. A SEM picture of a silicon photonic crystal is shown in Fig. A.2

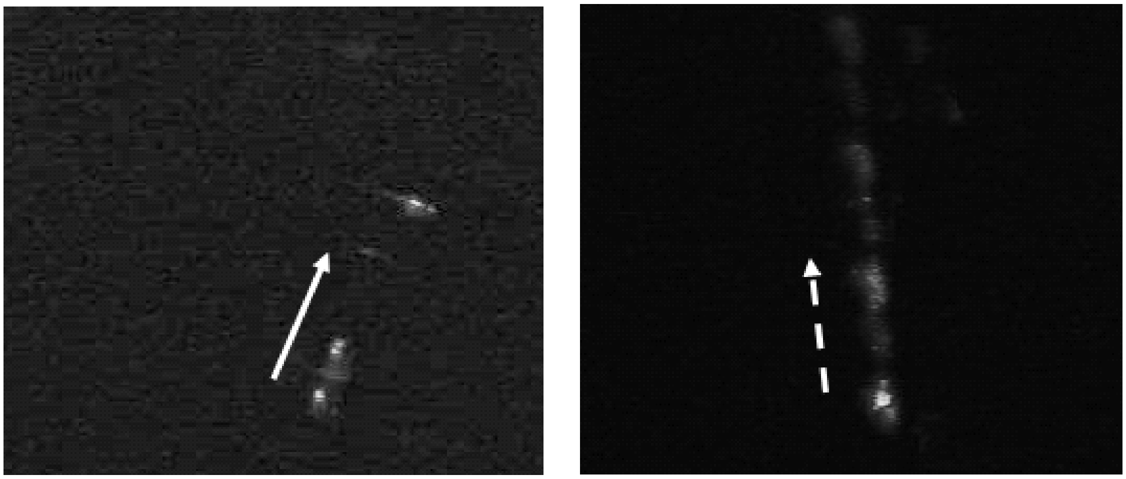

(a) (b)

Figure A.3: IR camera pictures of photonic crystal refraction

A.2 Refraction of a beam inside a photonic crystal

The silicon photonic crystal slab shown in Fig. A.2 was tested by my colleagues. Light of the TE polarization was first coupled into a silicon rib waveguide on the SOI chip. The rib wavegugide was directed to the interface of the photonic crystal slab, where the anomalous refraction took place. Two IR camera pictures are shown in Fig. A.3. The incident angle was about 34^o. And the refraction angles were about 31^o and -5^o at wavelengths 1565nm and 1541nm, respectively.

A.3 Further study

The polymer photonic crystal structures shown Fig. A.1 have been tested. However, it turned that the Hitachi polymer that we used were prone to cracking after deep holes were etched into the polymer. The cracking did not necessarily occur immediately after etching, but took place at an unpredictable time, which hindered further experiments on the devices. In the future, we plan to use other vendors' polymeric materials that are less susceptible to cracking.

Furthermore, one way to increase the refractive index contrast is to use silicon and polymer as two constitutive components of a photonic crystal [95], instead of air and polymer. The refractive index contrast between silicon and a typical polymer is in excess of 2, which is adequate to result in a full bandgap for both TE and TM polarizations for a 2D hexagonal (or triangular) lattice. It also solves the problem of the out-of-plane loss as polymer photonic crystals are prone to the loss owing to being above the lightline [17].

Further experiments need to be carried out with these new approaches to realize the demultiplexer proposed in Chapter 5.

Bibliography

[1] G. P. Agrawal, *Fiber-Optics Communications Systems*, 2nd ed. (John Wiley & Sons, New York, 1997).

[2] D. K. Mynbaev and L. L. Scheiner, *Fiber-Optic Communications Technology* (Prentice Hall, Upper Saddle River, 2001).

[3] I. Baumann, J. Seifert, W. Nowak, and M. Sauer, "Compact all-fiber add-drop-multiplexer using fiber Bragg gratings," IEEE Photonics Technology Letters, **8**, 1331 (1996).

[4] L. Dong, P. Hua, T. A. Birks, L. Reekie, and P. St. J. Russell, "Novel add/drop filters for wavelength-division-multiplexing optical fiber systems using a Bragg grating assisted mismatched coupler," IEEE Photonics Technology Letters, **8**, 1656 (1996).

[5] Xiang-Fei Chen, Chong-Cheng Fan, Y. Luo, Shi-Zhong Xie, and S. Hu, "Novel flat multichannel filter based on strongly chirped sampled fiber Bragg grating," IEEE Photonics Technology Letters, **12**, 1501 (2000).

[6] Jungho Kim and Byoungho Lee, "Bidirectional wavelength add-drop multiplexer using multiport optical circulators and fiber Bragg gratings," IEEE Photonics Technology Letters, **12**, 561 (2000).

[7] F. Bakhti, P. Sansonetti, C. Sinet, L. Gasca, L. Martineau, S. Lacroix, X. Daxhelet, and F. Gonthier, "Optical add/drop multiplexer based on UV-written Bragg grating in a fused 100% coupler," Electronics Letters , **33**, 803 (1997).

[8] Bin Liu, A. Shakouri, P. Abraham, and J. E. Bowers, "Optical add/drop multiplexers based on X-crossing vertical coupler filters," IEEE Photonics Technology Letters, **12**, 410 (2000).

[9] Wei Jiang, Y. Sun, R. T. Chen, B. Guo, J. Horwitz, and W. Morey, "Ball-lens based optical add-drop multiplexers: design and implementation," IEEE Photonics Technology Letters, **14**, 825 (2002).

[10] Wei Jiang, Y. Sun, R. T. Chen, B. Guo, J. Horwitz, and W. Morey, "Ball-lens-based optical add/drop multiplexers: designs and implementations", (Invited paper) Photonics West, San Jose, January 2002, Proc. SPIE, **4653**, 161- 171 (2002).

[11] E. Yablonovitch, Phys. Rev. Lett. **58**, 2059 (1987).

[12] S. John, Phys. Rev. Lett. **58**, 2486 (1987).

[13] S. Fan, P. R. Villeneuve, J. D. Joannopoulos, and H. A. Haus, Phys. Rev. Lett. **80**, 960 (1998).

[14] H. Kosaka, T. Kawashima, A. Tomita, N. Notomi, T. Tamamura, T. Sato, and S. Kawakami, Phys. Rev. B **58**, 10096 (1998) and references therein for related prior work.

[15] M. Notomi, K. Yamada, A. Shinya, J. Takahashi, C. Takahashi, and I. Yokohama, "Extremely Large Group-Velocity Dispersion of Line-defect Waveguides in Photonic Crystal Slabs," Physical Review Letters, **87**, 253902 (2001).

[16] T. J. Karle, Y. J. Chai, C. N. Morgan, I. H. White, T. F. Krauss, "Observation of Pulse Compression in Photonic Crystal Coupled Cavity Waveguides," J. Lightwave Technology, **22**, pp. 514 (2004).

[17] J D. Joannopoulos, R. D. Meade, and J. N. Winn, *Photonic Crystals* (Princeton University, Princeton, 1995).

[18] K. Hosomi and T. Katsuyama, "A dispersion compensator using coupled defects in photonic crystals," IEEE J. Quantum Electronics, **38**, 825 (2002).

[19] W. Jiang, and R. T. Chen, "Multi-channel optical add/drop process in symmetrical waveguide-resonator systems," Phys. Rev. Lett. **91**, 213901 (2003).

[20] T. Clark and K. Wanser, "Ball vs. gradient index lenses," Photonics Spectra, Feb. pp. 94-96, 2001.

[21] J. Ai, J. Popelek, Y. Li, and R. T. Chen, "Beam-splitting ball lens: a new integrated optical component," Opt. Lett. **24**, pp. 1478-1480, 1999.

[22] W. J. Smith, it Modern Optical Engineering, (McGraw-Hill, New York, 2000), pp. 301-366.

[23] Tohihiro Orito, private communication, 2000.

[24] E.L. O'Neill, *Introduction to Statistical Optics*, (Addison-Wesley, Reading, Massachusettes, 1963), pp. 88.

[25] H. A. Macleod, *Thin-Film Optical Filters*, 2nd ed., (McGraw-Hill, New York, 1989).

[26] K. Shiraishi, Y. Aizawa, and S. Kawakami, "Beam expanding fiber using thermal diffusion of the dopant," J. Lightwave Tech. **8**, pp. 1151-1161 (1990).

[27] A. Chutinan, M. Mochizuki, M. Imada, and S. Noda, Appl. Phys. Lett. **79**, 2690 (2001).

[28] A. Sharkawy, S. Shi, and D. W. Prather, Appl. Opt. **40**, 2247 (2001); and K. Takano and K. Nakagawa, IEICE Trans. Commun. **E84-B**, 1295 (2001).

[29] S. Fan, P. R. Villeneuve, J. D. Joannopoulos, M. J. Khan, C. Manolatou, and H. A. Haus, Phys. Rev. B **59** 15882 (1999)

[30] S. John, Phys. Today **44** (5), 32 (1991).

[31] Y. Xu, Y. Li, R. K. Lee, and A. Yariv, Phys. Rev. E **62**, 7389 (2000).

[32] W. Jiang, Master's thesis, University of Texas at Austin, 2000.

[33] C. Manolatou, S. Fan; P. R. Villeneuve, H. A. Haus, and J. D. Joannopoulos, IEEE J. Quantum Electon. **35** 1451 (1999).

[34] M. Hamermesh, *Group Theory and Its Application to Physical Problems* (Addison-Wesley, Reading, 1962).

[35] J. J. Sakurai, *Modern Quantum Mechanics* (Addison-Wesley, Redwood City, CA, 1985).

[36] S. Fan, P. R. Villeneuve, J. D. Joannopoulos, and H. A. Haus, Phys. Rev. B **64**, 245302, (2001).

[37] A. V. Oppenheim and R. W. Schafer, *Discrete-time Signal Processing*, 2nd ed., (Prentice Hall, Upper Saddle River, 1999).

[38] M. G. Daly, P. E. Jessop, and D. Yevick, J. Lightwave Technol. **14**, 1695 (1996).

[39] S. G. Johnson, C. Manolatou, S. Fan, P. R. Villeneuve, and J. D. Joannopoulos, Opt. Lett. **23**, 1855 (1998).

[40] L. Wu, M. Mazilu, T. Karle, and T. F. Krauss, J. Quant. Electron. **38**, 915 (2002).

[41] M. Notomi, Phys. Rev. B **62**, 10696 (2000).

[42] T. Baba and M. Nakamura, J. Quantum Electron. **38**, 909 (2002). T. Baba and T. Matsumoto, Appl. Phys. Lett. **81**, 2325 (2002).

[43] C. Luo, S. G. Johnson, J. D. Joannopoulos, and J. B. Pendry, Phys. Rev. B **65** 201104 (2002).

[44] K. B. Chung and S. W. Hong, Appl. Phys. Lett. **81**, 1549 (2002).

[45] J. Bravo-Abad, T. Ochiai, and J. Sanchez-Dehesa, Phys. Rev. B **67**, 115116 (2003) and references therein.

[46] The long wavelength limit is known: P. Halevi, A. A. Krokhin, and J. Arriaga, Phys. Rev. Lett. **82**, 719 (1999).

[47] P. Yeh, *Optical Waves in Layered Media* (Wiley, New York, 1988).

[48] J. B. Pendry and A. MacKinnon, Phys. Rev. Lett. **69**, 2772 (1992).

[49] T. Minami, H. Ajiki, and K. Cho, Physica E **13**, 432 (2002).

[50] Z. Li and K. Ho, Phys. Rev. B **68**, 155101 (2003).

[51] K. Ohtaka, T. Ueta, and K. Amemiya, Phys. Rev. B **57**, 2550 (1998).

[52] N. Stefanou, V. Yannopapas, and A. Modinos, Comput. Phys. Commun., **132** 189 (2000).

[53] T. Ochiai and J. Sanchez-Dehesa, Phys. Rev. B **64**, 245113 (2001).

[54] K. Sakoda, "Symmetry, degeneracy, and uncoupled modes in two-dimensional photonic lattices," Phys. Rev. **B 52**, 7982 (1995).

[55] K. Sakoda, Phys. Rev. B **52**, 8992 (1995).

[56] Wei Jiang *et al.*, "Theoretical and experimental study of photonic-crystal-based structures for optical communication applications," Photonic West, San Jose, January 2004, Proc. SPIE, **5360** pp. 190-198 (2004).

[57] Z.-Y. Li and K.-M. Ho, "Anomalous Propagation Loss in Photonic Crystal Waveguides," Phys. Rev. Lett. **92**, 063904 (2004).

[58] L. V. Azaroff *et al.* , *X-Ray Diffraction* (McGraw-Hill, New York, 1974), chapter 4.

[59] J. B. Pendry, *Low Energy Electron Diffraction* (Academic, London, 1974), for example.

[60] P. St. J. Russell, Electron. Lett. **20** 72 (1984).

[61] R. Zengerle, J. Mod. Opt. **34** 1589 (1987).

[62] C. Kittel, *Introduction to Solid State Physics*, 6th ed., (Wiley, New York, 1986).

[63] J. E. Dennis, J. F. Traub, and R. P. Weber, SIAM J. Numer. Anal. **13**, 831 (1976), and references therein.

[64] P. Lancaster, *Lambda-matrices and Vibrating Systems*, (Pergamon, Oxford, 1966).

[65] L. Li, J. Opt. Soc. Am. A **13**, 1024 (1996).

[66] L. C. Botten, N. A. Nicorovici, R. C. McPhedran, C. Martijn de Sterke, and A. A. Asatryan, Phys. Rev. E **64**, 46603 (2001).

[67] K. Sakoda, *Optical Properties of Photonic Crystals* (Springer, Berlin, 2001).

[68] P. Yeh, J. Opt. Soc. Am. **69**, 742 (1979).

[69] L. C. Kinsey, *Topology of Surfaces* (Springer-Verlag, New York, 1993).

[70] A. L. Mackay, Physica A, **114**, 609 (1982).

[71] Y. S. Chan, C. T. Chan, and Z. Y. Liu, Phys. Rev. Lett. **80**, 956 (1998) and references therein.

[72] M. Notomi, H. Suzuki, T. Tamamura, and K. Edagawa, Phys. Rev. Lett. **92**, 123906 (2004) and references therein.

[73] D. Maystre, J. Mod. Opt. **50**, 1431 (2003).

[74] See a review by T. K. Gaylord and M. G. Moharam, Proc. IEEE **73**, 894 (1985);

[75] M. G. Moharam and T. K. Gaylord, J. Opt. Soc. Amer. **72**, 1385 (1982).

[76] J. B. Pendry, Phys. Rev, Lett. **85**, 3966 (2000).

[77] Wei Jiang, C. Tian, L. Wu, Y. Chen, R. T. Chen, "Abnormal propagation and interface refraction of light in a photonic crystal and their applications," Photonic West, San Jose, January 2003, Proc. SPIE, **5000**, 251-256 (2003).

[78] R. T. Chen, "Polymer-based photonic integrated circuits," (invited paper), Optics & Laser Technology, **25**, 347 (1993).

[79] M. Meier, A. Mekis, A. Dodabalapur, A. Timko, R. E. Slusher, J. D. Joannopoulos, and O. Nalamasu, "Laser action from two-dimensional distributed feedback in photonic crystals," **74**, 7 (1999).

[80] C. Liguda, G. Böttger, A. Kuligk, R. Blum, M. Eich, H. Roth, J. Kunert, W. Morgenroth, H. Elsner, and H. G. Meyer , "Polymer photonic crystal slab waveguides," Appl. Phys. Lett. **78**, 2434 (2001).

[81] S. Inoue, K. Kajikawa, and Y. Aoyagi, "Dry-etching method for fabricating photonic-crystal waveguides in nonlinear-optical polymers," Appl. Phys. Lett., **82**, 2966 (2003).

[82] M. Deutsch, Yu. A. Vlasov, and David J. Norris, "Conjugated-polymer photonic crystals," Adv. Mater. **12**, 1176 (2000).

[83] A. C. Edrington, A. M. Urbas, P. DeRege, C. X. Chen, T. M. Swager, N. Hadjichristidis, M. Xenidou, L. J. Fetters, J. D. Joannopoulos, Y. Fink, and E. L. Thomas, "Polymer-based photonic crystals," Adv. Mater. **13**, 421 (2001).

[84] A. Yokoo, M. Notomi, M. Nakao, and T. Tamamura, and H. Masuda, "Emission from functional-polymer-injected point defects in two-dimensional photonic crystals," IEEE J. Quant. Electron. **38**, 938 (2002).

[85] M. Straub, M. Ventura, and M. Gu, "Multiple higher-order stop gaps in infrared polymer photonic crystals," Phys. Rev. Lett., **91**, 043901 (2003).

[86] M. J. Escuti and G. P. Crawford, "Holographic photonic crystals," Opt. Eng. **43**, 1973 (2004).

[87] Roberto R. Panepucci, Bryan H. Kim, Vilson R. Almeida, and Matthew D. Jones, "Slab Polymer Photonic Crystals," (invited paper) Proc. SPIE **5597**, 62, (2004).

[88] T. F. Krauss, R. M. De La Rue, S. Brand, "Two-dimensional photonic-bandgap structures operating at near-infrared wavelengths," Nature **383**, 699 (1996).

[89] S. G. Johnson, P. R. Villeneuve, S. Fan, and J. D. Joannopoulos, Phys. Rev. B **62**, 8212 (2000).

[90] A. Chutinan and S. Noda, Phys. Rev. B **62**, 4488 (2000).

[91] E. Chow, S. Y. Lin, S. G Johnson, P. R. Villeneuve, J. D. Joannopoulos, J. R. Wendt, G. A. Vawter, W. Zubrzycki, H. Hou, and A. Alleman, "Three-dimensional control of light in a two-dimensional photonic crystal slab," Nature, **407**, 983 (2000).

[92] S. Y. Lin, E. Chow, E.; S. G. Johnson, and J. D. Joannopoulos, "Demonstration of highly efficient waveguiding in a photonic crystal slab at the 1.5-mum wavelength", Opt. Lett. **25** 1297 (2000).

[93] M. Loncar, D. Nedeljkovic, T. Doll, J. Vuckovic, A. Scherer, and T. P. Pearsall, "Waveguiding in planar photonic crystals," **77**, 1937 (2000).

[94] A. Adibi, Y. Xu, R. K. Lee, A. Yariv, and A. Scherer, Phys. Rev. B **64**, 033308 (2001).

[95] M. Tokushima, H. Yamada, and Y. Arakawa, "1.5-um-wavelength light guiding in waveguides in square-lattice-of-rod photonic crystal slab," Appl. Phys. Lett. **84**, 4298 (2004).

Vita

Wei Jiang was born in Nanjing, People's Republic of China on October 4, 1974, the son of Ai Jiang and Yunxian Hua. A graduate of Nanjing No. 1 High School, he received the degree of Bachelor of Science in physics from Nanjing University in 1996. He spent two years for graduate study in physics at Naning University, then in August, 1998, he transferred to the University of Texas at Austin, where he received the degree of Master of Arts in physics in May 2000. He subsequently enrolled in an electrical and computer engineering doctoral program at the University of Texas. In 2001, he worked for Radiant Photonics in Austin, Texas. Mr. Jiang served the student body of the University of Texas and Austin Asian community in numerous roles.

Permanent Address: 158 Shanghai Road, Bldg 1, Apt. 207, Nanjing, China

This dissertation was typeset with LaTeX 2_ε[1] by the author.

---

[1] LaTeX 2_ε is an extension of LaTeX. LaTeX is a collection of macros for TeX. TeX is a trademark of the American Mathematical Society. The macros used in formatting this dissertation were written by Dinesh Das, Department of Computer Sciences, The University of Texas at Austin, and extended by Bert Kay, James A. Bednar, and Ayman El-Khashab.